Science Concept 6: The Moon is an Accessible Laboratory for Studying the Impact Process on Planetary Scales

Science Concept 6: The Moon is an accessible laboratory for studying the impact process on planetary scales

Science Goals:

a. Characterize the existence and extent of melt sheet differentiation.

b. Determine the structure of multi-ring impact basins.

c. Quantify the effects of planetary characteristics (composition, density, impact velocities) on crater formation and morphology.

d. Measure the extent of lateral and vertical mixing of local and ejecta material.

INTRODUCTION

Impact cratering is a fundamental geological process which is ubiquitous throughout the Solar System. Impacts have been linked with the formation of bodies (*e.g.* the Moon; Hartmann and Davis, 1975), terrestrial mass extinctions (*e.g.* the Cretaceous-Tertiary boundary extinction; Alvarez *et al.*, 1980), and even proposed as a transfer mechanism for life between planetary bodies (Chyba *et al.*, 1994). However, the importance of impacts and impact cratering has only been realized within the last 50 or so years.

Here we briefly introduce the topic of impact cratering. The main crater types and their features are outlined as well as their formation mechanisms. Scaling laws, which attempt to link impacts at a variety of scales, are also introduced. Finally, we note the lack of extraterrestrial crater samples and how Science Concept 6 addresses this.

Crater Types

There are three distinct crater types: simple craters, complex craters, and multi-ring basins (Fig. 6.1). The type of crater produced in an impact is dependent upon the size, density, and speed of the impactor, as well as the strength and gravitational field of the target.

Simple craters

Simple craters, as their name suggest, are the most basic, and smallest, craters. They are typified by a smooth, bowl-shaped profile, with essentially no flat floor within the crater. They have a depth-to-diameter ratio of 1:3–1:5 (Melosh, 1989; Melosh and Ivanov, 1999) with their rims slightly uplifted due to stratigraphic tilt and ejecta deposition. Within the crater resides broken and melted target rock – breccia, which has slumped off the crater walls and overlays fractured bedrock.

Complex craters

Between diameters of ~15–20 km on the Moon, simple craters begin to transition into complex craters (on Earth this transition occurs between 2–4 km [Pike, 1988]; transition diameter is inversely proportional to gravity, hence the smaller transition diameter on Earth compared to the Moon). Complex craters can be categorized into two groups: central-peak and peak-ring craters. Central-peak craters are characterized by a central dome which protrudes from the crater floor; a topographically high rim again defines the edge of the impact structure. Between the central dome and crater rim is an area of relatively flat topography produced by breccia infill which overlays molten material. Unstable material from the crater wall collapses inward as large discrete blocks forming terraces. Complex craters have a smaller depth-to-diameter ratio compared

to simple craters, a consequence of central peak and peak ring formation. Peak-ring craters are larger in diameter than central-peak craters and possess a ring of raised massifs roughly half the rim-to-rim diameter instead of a central peak. The transition between central-peak and peak-ring crater morphology begins at diameters of ~140 km on the Moon (Melosh, 1989), however the transition is gradual and ill-defined; Antoniadi Crater is 145 km in diameter and possesses both a peak ring and a central peak, while Tsiolkovsky Crater, 190 km in diameter, contains just a central peak. Above diameters of 200 km, nearly all lunar craters display remnants of a peak ring.

Multi-ring basins

Multi-ring basins are the largest type of impact structure and are characterized by the presence of at least one asymmetric, inward facing scarp ring outside the main crater rim. As with peak-ring craters, they generally possess (at least) one peak ring. Multi-ring basins begin on the Moon at diameters of ~300 km (Wilhelms, 1987). No multi-ring basin has been verified on Earth; Vredefort (~300 km diameter), Sudbury (~200 km diameter) and Chicxulub (~180 km diameter) impact structures are thought to be the best basin candidates.

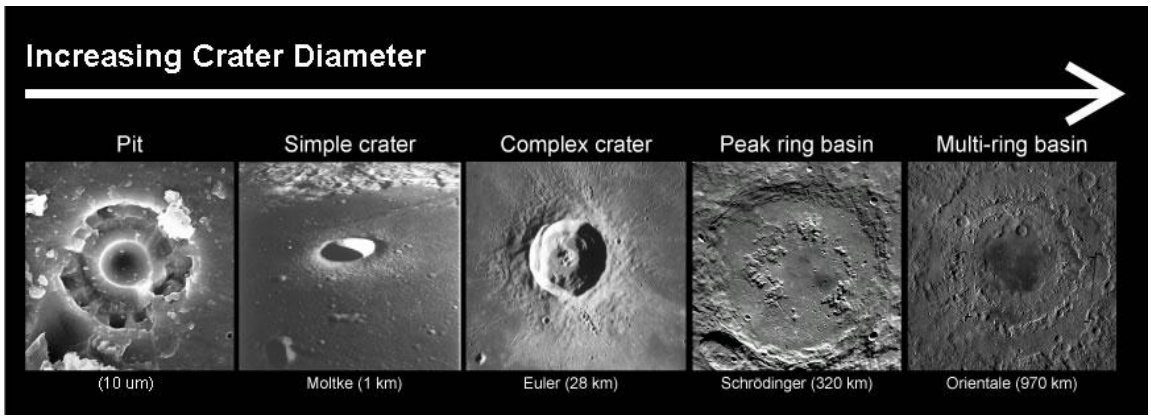

FIGURE 6.1 Impact craters on an airless body like the Moon range in size from pin-size structures to continent-size structures. This illustration shows a broad range of examples (from left to right): (a) a 10 micron-diameter crater on a glassy, ~465 micron diameter lunar spherule from the Luna 16 landing site (Hartung *et al.*, 1972); (b) a 1 kilometer diameter simple crater called Moltke; (c) a 28 kilometer diameter complex crater called Euler; (d) a 320 kilometer diameter peak-ring impact basin called Schrödinger; and (e) a 970 kilometer diameter multi-ring impact basin called Orientale. Image Credit: LPI (Priyanka Sharma).

Formation of Impact Craters

The cratering process can be divided into three distinct stages: contact/compression, excavation, and modification (Fig. 3.9). All impacts, regardless of scale, will experience these three stages during crater formation. The most common angle for impact is 45^{o} (Gilbert, 1893; Shoemaker, 1962) to the horizontal.

Contact/compression begins when the leading edge of the impactor hits the target surface. This creates two shock waves; one travels into the target, the other through the impactor. Tens of gigapascals of pressure can be created by the shock, melting and vaporizing target and impactor material; peak shock pressure is the same in both target and impactor. Evidence of these high shock pressures includes shatter cones in shocked rock and high pressure phase minerals (coesite and stishovite). The contact/compression stage is defined by the time taken for the shock to travel up through the impactor, be reflected at the impactor's rear edge, travel back through the impactor as a release wave (releasing the impactor from the high shock pressures), and reach the impactor-target interface. This time can be approximated by the time taken for the impactor to travel a distance equal to twice its diameter at its impact speed; for an impactor 1 km in diameter travelling at 20 km/s contact/compression would last ~0.1 s.

Excavation is the next stage, determining the volume of excavated material. Following shock compression and release impacted rock is accelerated and driven away from the impact point. The path of

movement of a particle is dependent on its original location within the target. Material moves along streamlines away from the impact point resulting in the formation of a bowl-shaped, transient cavity. This cavity is in effect split into two distinct regions separated by the hinge streamline (Fig. 6.2). Material found to a depth equal to approximately one third of the transient cavity's depth is driven upwards and out of the cavity; this is known as the excavation cavity (the excavation and transient cavity are equal in diameter). Below this depth, material is driven downward and outward. This flow of (particle) material is described by the Z model (Maxwell and Seifert, 1974; Maxwell, 1977), which is based on numerical simulations of high energy explosions, although Croft (1980) showed that this can be applied to the excavation of high-speed impact craters.

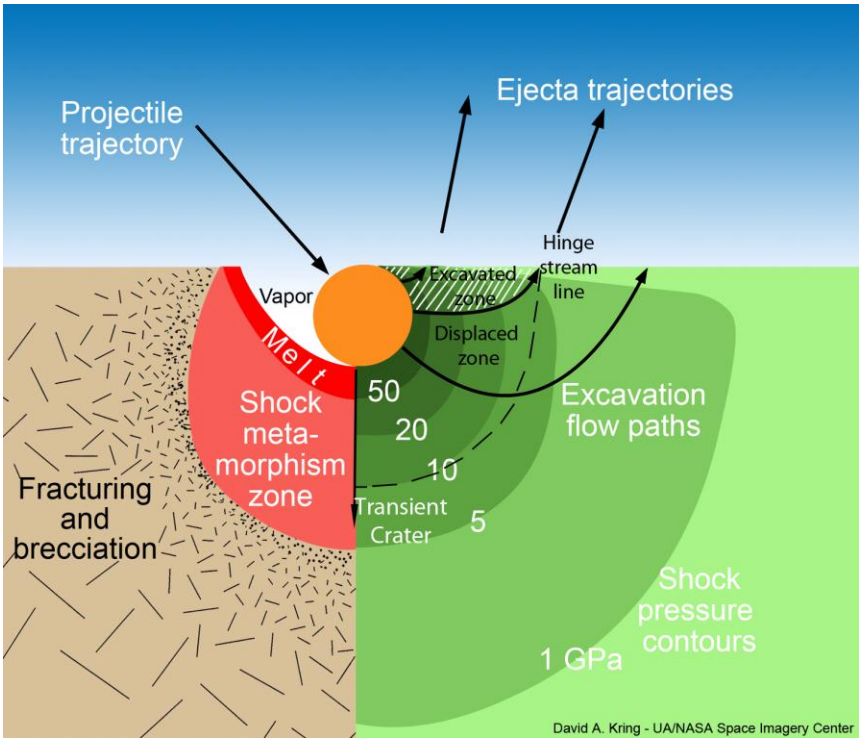

FIGURE 6.2 The impact of a projectile at 45^{o} showing the decrease in shock pressure, ejecta trajectories and excavation flow paths. (Modified after David Kring, UA/NASA Space Imagery Center).

Eventually the shock and release waves, through attenuation, lose their ability to excavate or displace target rock. At this point the cavity is at its largest size, and is referred to as the transient crater. The size of the transient crater is dependent on many factors including impactor speed, angle of impact, and impactor and target material. The transient crater is an ephemeral feature and so must be estimated from theoretical studies and geological field studies; these have suggested the maximum transient crater depth is approximately one third of its diameter (this proportion appears to remain constant for craters of widely varying sizes). This can be used to estimate the volume of the excavation cavity, as well as the impactor energy. The latter however is non-unique; energy can represent a wide variety of impact conditions. The formation of the transient crater marks the end of the excavation stage. Excavation lasts longer than contact/compression, but is still very short, geologically speaking, lasting no more than a few minutes for the very largest basin-forming impacts.

Following excavation, the final stage of crater formation, modification, begins. Here rock strength and gravity are the dominant forces resulting in the collapse of the transient crater which alters the crater morphology. In simple craters, this involves the failure of the crater walls, leading to breccia infill of the crater floor. For complex craters and multi-ring basins, modification is more complex with various theories proposed for the formation of central peaks, peak rings, and basins; see Science Goal 6b for a discussion of these. In general, the modification stage can be thought of as ending when motion ceases completely.

Scaling Laws

Statistically, only a small subset of craters has been studied on Earth. These investigations, as well as high energy explosion and nuclear tests, have been used to formulate scaling laws (*e.g.*, Croft, 1985) linking small, simple impacts to larger terrestrial and lunar impact structures, including multi-ring basins. Scaling laws have been formulated to estimate, among other things, transient crater diameter, melt volume, and depth of excavation. Currently, scaling laws represent the best estimates for predicting crater features at all scales, however their ability to accurately predict features of the largest impact structures, multi-ring basins, remains uncertain. Our understanding of cratering processes has, however, been severely impeded on Earth where other geologic processes erode impact sites. Thus, we are driven to the Moon for answers. Science Concept 6 aims to highlight lunar sites where in-situ studies can test and re-evaluate scaling laws for basin-scale impacts. The scaling laws relative to the various Science Goals of Science Concept 6 will be discussed in greater detail throughout this section.

Apollo Missions – Lunar Crater 'Ground Truth'

A few craters were visited, and sampled, during the Apollo missions (Table 6.1), though most were <2 km in diameter, limiting samples to small, simple craters or reworked debris from larger craters. Because impact cratering was so poorly understood at the time of Apollo, these few samples allowed some basic conclusions about lunar craters be made. One of these conclusions was that the vast majority of lunar craters were formed by impacts rather than volcanism (volcanism was a popular pre-Apollo hypothesis for the formation of many lunar craters; *e.g.* Fielder and Marcus, 1967); another was that craters distribute ejecta on global scales producing regolith. Science Concept 6 aims to address both fundamental and detailed issues to expand our knowledge of impact cratering through further 'ground truth' studies.

TABLE 6.1 Craters visited (with approximate diameters) during the Apollo missions (data from http://www.lpi.usra.edu/lunar/missions/apollo/).

Apollo Mission	Crater	Diameter (m)
11	Little West	183
12	Halo	7
	Sharp	13
	Block	13
	Bench	55
	Head	95
	Surveyor	150
	Middle Crescent	335
14	Flank	38
	North Triplet	105
	Cone	340
15	Spur	70
	Elbow	290
	Dune	340
	St. George	1750
16	Cinco	65
	Buster	85
	Flag/Plum	230

	Wreck	740
	N. Ray	980
17	Van Serg	96
	Shorty	105
	Lara	530
	Steno	545
	Nasen	600?
	Camelot	650

SCIENCE GOAL 6A: CHARACTERIZE THE EXISTENCE AND EXTENT OF MELT SHEET DIFFERENTIATION

Introduction

Impact cratering is one of the most influential processes that affect the evolution of the lunar surface (Ahrens and O'Keefe, 1972) and similar planetary bodies. When impacts of sufficiently high speed occur they generate pressures on the order of 40–100 GPa, far greater than the threshold of whole rock melting. In large-scale impacts, large volumes of impact melt can pool into sheets, which can be kilometers thick (Fig. 6.3). Chemical differentiation is thought to separate these large melt sheets into varying lithologies (Fig. 6.4) based on density. The notion that large impact melt sheets can differentiate carries important implications for how lunar samples and the early geologic history of the lunar highlands are interpreted (Grieve *et al.*, 1991). On Earth, examples of differentiated impact melt sheets have been found (*e.g.* Therriault *et al.*, 2002), however due to destructive terrestrial processes such as erosion and plate tectonics, examples are rare. These kind of destructive processes do not occur on the Moon, thereby making it an ideal laboratory for exploring melt sheet differentiation. The aim of Science Goal 6a is to study lunar melt sheets and characterize the existence and extent of melt sheet differentiation. This section will outline the most suitable lunar locations to achieve this goal.

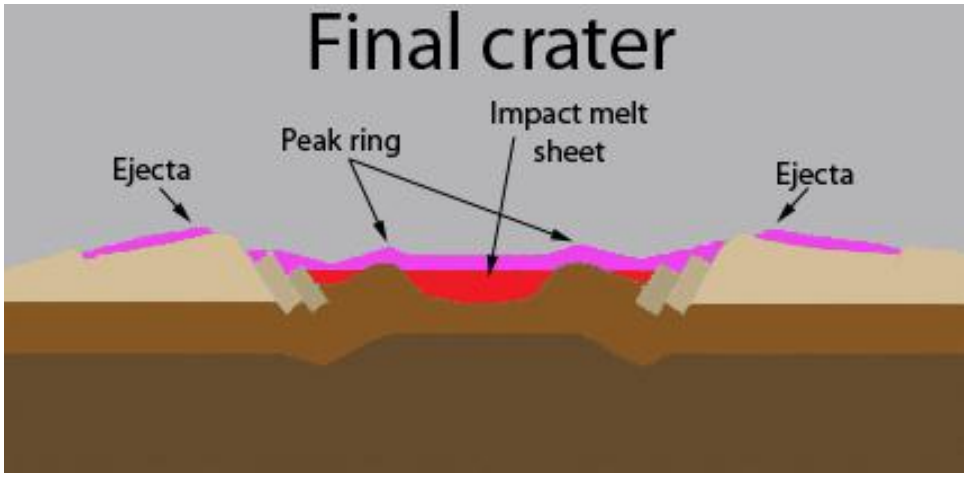

FIGURE 6.3 The structure of a multi-ring basin (modified after LPI classroom illustration).

Terrestrial Differentiated Melt Sheet Analogs

Chemical and textural characteristics of returned lunar samples interpreted as impact melts show similarities to those formed on the Earth, suggesting parameters governing melt processes are similar for both bodies (Floran *et al.*, 1978). Terrestrial analogs are an integral part in understanding processes on other planetary bodies; they promote development of models, experiments, and other methods of understanding which can be used for comparisons to non-terrestrial cases. The Sudbury and Manicouagan impact structures have been found to possess differentiated melt sheets; understanding these terrestrial structures will therefore aid understanding and exploration of melt sheet differentiation on other bodies.

Sudbury impact structure

The first impact structure recognized to possess a differentiated melt sheet was the Sudbury impact structure, Canada. The impact occurred ~1.85 Ga (Zieg and Marsh, 2005) into primarily granitic and gneissitic target rocks, with an estimated 5 km ceiling of metamorphosed sediments (Kring, 1995); the crater is 220 km in diameter (Stöffler *et al.*, 1994). The crater contains an igneous complex that includes a ~2.5 km thick differentiated melt sheet (Fig. 6.5) (Grieve *et al.*, 1991). The differentiation process, which took anywhere from days to months for complete differentiation, divided the melt into a norite (~56% SiO_2) layer overlain by granophyre (~70% SiO_2) with a thin transition zone of quartz gabbro between them (Zieg and Marsh, 2005).

	Upper unit (granophyre) 62.4%		Transition zone 5.8%		Middle unit (quartz gabbro) 4.7%		Lower unit (norite) 22.5%		Contact sublayer 4.6%		SIC average 100.00%	SIC from Collins (1934)
	23 samples	S.D.	4 samples	S.D.	5 samples	S.D.	12 samples	S.D.	2 samples	S.D.	46 samples	
SiO_2	68.71	1.29	61.52	3.67	55.25	1.38	58.82	0.62	52.33	0.25	64.57	63.14
TiO_2	0.81	0.11	1.43	0.31	1.45	0.39	0.57	0.07	0.54	0.00	0.81	0.74
Al_2O_3	12.80	0.31	13.52	0.11	14.32	0.85	16.17	0.54	15.36	0.51	13.79	14.65
Fe_2O_3	1.74	0.43	2.47	0.39	3.53	1.02	1.33	0.20	2.20	0.99	1.80	1.52
FeO	4.02	0.67	6.70	1.14	7.86	0.83	5.43	0.38	7.50	0.57	4.84	5.17
MnO	0.07	0.01	0.14	0.02	0.14	0.02	0.11	0.01	0.14	0.01	0.09	0.08
MgO	0.88	0.29	1.39	0.69	3.57	0.09	4.15	0.47	8.28	0.76	2.12	2.85
CaO	2.19	0.53	4.48	1.13	7.36	0.29	6.47	0.71	7.67	0.52	3.79	4.03
Na_2O	3.49	0.38	3.55	0.30	2.95	0.20	3.45	0.75	2.40	0.14	3.41	3.20
K_2O	3.60	0.45	2.46	0.28	1.70	0.23	1.53	0.42	1.33	0.36	2.87	2.91
P_2O_5	0.17	0.04	0.39	0.13	0.29	0.26	0.13	0.03	0.09	0.00	0.18	0.16
H_2O_{total}	1.33	0.18	1.82	0.17	1.88	0.09	1.66	0.28	2.00	0.00	1.49	1.24
$CO_{2\ total}$	0.18	0.16	0.32	0.22	0.08	0.04	0.25	0.22	0.20	0.00	0.20	0.23
S	0.04	0.03	0.05	0.05	0.10	0.03	0.05	0.03	0.20	0.10	0.05	0.08
L.O.I.	0.49	0.83	2.56		0.84	1.15	0.68	1.07	2.42		0.76	
Total	100.52		102.80		101.32		100.80		102.66		100.77	100.00

FIGURE 6.5 Chemical compositions for the units of the Sudbury Igneous Complex, as well as an overall average composition (after Therriault *et al.*, 2002).

Manicouagan impact structure

A more recently confirmed differentiated, terrestrial melt sheet is within the Manicouagan impact structure, Canada. The Manicouagan impact occurred 214±1 Ma (Hodych and Dunning, 1992), creating an impact structure ~100 km in diameter (Grieve, 1987). Target lithologies were Precambrian crystalline rocks overlain by a thin (<200 m), discontinuous layer of Middle Ordovician carbonates and shales (Spray *et al.*, 2010). The structure is unique among Earth's larger impact structures in that it is so well preserved, exposed, and has not been subjected to significant erosion or tectonic events, unlike Sudbury (Spray *et al.*, 2010). Despite its pristine state, the differentiated nature of the 55 km diameter melt sheet remained undiscovered until resource drilling commenced in the mid-1990's. Prior to this, geological field studies estimated the melt sheet to be ~230 m thick with another 50 m of material lost to erosion (O'Connell-Cooper and Spray, 2010). The drill core from the central part of the melt sheet, core MAN-0608, confirmed a clast free melt sheet with a thickness of ~1100 m (Spray *et al.*, 2010), a more modest thickness than the >2.5 km thick melt sheet of the Sudbury impact structure (Stöffler and Deutsch, 1994). Core MAN-0608, unlike the other homogeneous cores from shallower regions of the melt sheet, revealed two distinct geochemical layers with a transitional dividing zone. The top 278 m represents the upper layer which is relatively enriched in silica (60.55 wt. %) and relatively depleted in CaO and MgO with a bulk composition of quartz monzodiorite. The bottom 525 m represents the lower layer which is enriched in

CaO and MgO but relatively depleted in silica (56.64 wt. %) with a bulk composition ranging from quartz monzodiorite to monzodiorite (Fig. 6.8) (O'Connell-Cooper and Spray, 2010).

Manicouagan as an analog for the lunar highlands

The Manicouagan impact structure is an excellent analog for the Moon because the central uplift is composed of anorthositic material. Anorthosites are very common on the Moon, making up the highlands material which accounts for ~83% of the lunar surface. Manicouagan is one of only a few terrestrial impacts that contain anorthosite, the others being the Charlevoix (54 km diameter) and Mistastin (28 km diameter) impact structures, both in Canada, though these have comparatively less anorthosite than Manicouagan. The Manicouagan structure has not been reworked by constant bombardment so it provides a good comparison to pristine lunar highlands material. The largest impacts on the Moon incorporate more mafic, mantle material in their melts so Manicouagan is likely only an analog for small- to intermediate-sized events impacting the highlands.

Crater Sizes and Resulting Melt

Lunar craters range in size from micro-structures recorded in glasses to vast basins that stretch up to thousands of kilometers across the surface (Ahrens and O'Keefe, 1972). Such a wide range of sizes generates, as expected, an equally wide range of resulting melt products with the relative volume of melt produced and retained within the crater increasing as event magnitude increases (Fig. 6.9). Melt volume, V_m, is calculated using the equation

$$V_m = cD_{tc}^{\ d}, \qquad (6.1)$$

where c and d are constants (~1–2 × 10^{-4} and 3.85, respectively; see Table 2 of Cintala and Grieve, 1998) determined by fitting the curves in Fig. 6.9 and D_{tc} is the diameter of the transient crater.

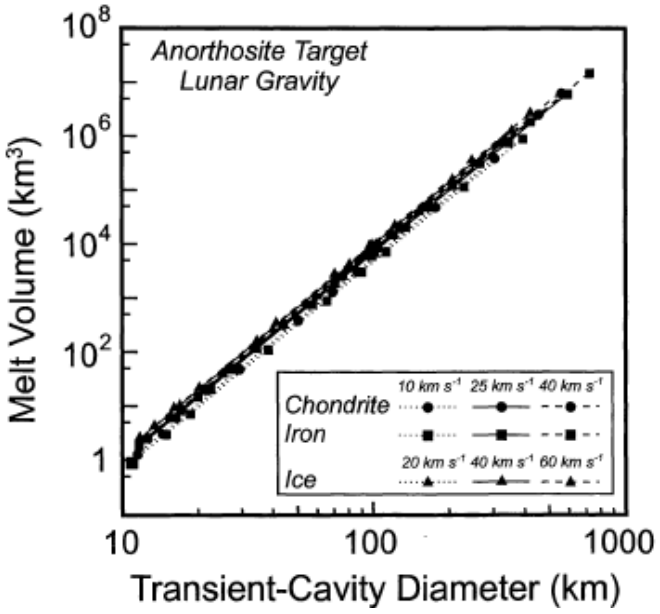

FIGURE 6.9 Calculations for melt volume as a function of transient crater diameter for varying impactor compositions and speeds (from Cintala and Grieve, 1998).

Simple craters

Melts in simple craters, like Alfraganus C (10 km diameter), occur only as thin veneers that coat the floor and, to a lesser extent, the rim (Hawke and Head, 1977) (Fig. 3.12, top panel). Models suggest the ratio of the volume of melt to the volume of the transient cavity in a crater of this size will be ~0.007 (Cintala and Grieve, 1998), equating to a melt sheet approximately 3 m in thickness. The relatively small

volumes of melt created are quickly choked with clasts, increasing the melt's viscosity and quenching it rapidly (Cintala and Grieve, 1998). Craters in this regime will not produce differentiated melt sheets.

Complex craters

Larger craters with thick melt sheets will be less susceptible to the clast choking process. Complex craters have a higher ratio of melt volume to transient crater volume compared to simple craters. Models suggest a crater the size of Tycho (102 km diameter) would have a ratio of ~0.04, producing a melt sheet ~150 m thick (Fig. 3.12, middle panel) (Cintala and Grieve, 1998). Though craters of this size have considerably more melt than simple craters they still lack the dimensions necessary to produce differentiated melt sheets.

Impact basins

Large amounts of melt are generated during basin-forming impacts and constitute an important rock type on the Moon (Spudis, 1993). The calculated melt volume to transient crater volume ratio in basins ranges from 0.1 (Schrödinger) to greater than 1 for the largest basins. Models suggest a basin the size of Schrödinger, the second smallest basin at 320 km in diameter, would produce a melt sheet approximately 1.4 km in thickness (Fig. 3.12, bottom panel) (Cintala and Grieve, 1998). The largest basin on the Moon, the South Pole-Aitken Basin (SPA), is thought to have a ~200 km thick melt sheet (Morrison, 1998).

Scaling issues for the Earth and Moon

"*Direct correlation from the Earth to the Moon regarding impact processes can lead to confusion at best and incorrect conclusions at worst*" (Cintala and Grieve, 1998). Accurate scaling is vital for determining locations to investigate possibly differentiated melt sheets. For instance, five times as much melt would be produced for a given transient crater size on Earth compared to the Moon (Cintala and Grieve, 1998). There are three variables that need to be considered when modeling impact melt generation: impact speed, target gravity, and projectile size (Cintala and Grieve, 1994). Only speed and gravity need to be considered with regards to scaling issues between the Earth and Moon because average projectile size will be comparable.

Impact speed

On Earth, impacts tend to have slightly higher speeds than those on the Moon. This speed difference is relatively small due to their proximity; it would have been even less in the past when the two bodies were closer together. In their present positions, this small speed difference can cause an almost 70% greater volume of melt on the Earth for craters of identical size (Cintala and Grieve, 1994).

Gravity

The volume of impact melt is essentially independent of gravity (O'Keefe and Ahrens, 1977) however the dimensions of impact craters are dependent primarily on target body gravity. Impact experiments conducted with varying gravity yield successively smaller crater sizes as gravity increases, assuming a constant impact energy. Models suggest lunar transient crater diameters are almost 50% larger than their terrestrial impact energy equivalents (Cintala and Grieve, 1994). This has implications for how thick the melt sheet will be based on larger surface areas of transient craters for gravities less than Earth's. Considering these variables, events of larger magnitude will be required to facilitate differentiated melt sheets for impacts on the Moon compared to the Earth.

Analysis Methods

Various depths within a melt sheet must be accessed to determine if any vertical composition heterogeneity exists. Melt sheets may be many kilometers thick and buried underneath other lithologies, therefore testing the nature of internal differentiation within them could be problematic. Methods for testing the existence and extent of their differentiation must therefore try to circumvent this problem.

Geophysical analysis

Seismic detection of subsurface features is an analysis method used widely by geologists to detect structural features and, to a lesser extent, lithological variation. Seismic surveys could be used to infer density and structural changes beneath the surface and therefore investigate the nature of melt sheets and whether or not they are differentiated.

Stratigraphic analysis

Currently the most robust method for testing melt differentiation on the Moon is through stratigraphic interpretation of uplifted central structures. When an impact occurs, material from beneath the zone of melting is uplifted above the crater floor (Fig. 6.11). Investigation of this material, for example in central peaks, can help determine the composition of originally deeper lithologies beneath the lunar surface. Some of this deep, excavated and uplifted material may represent melt sheet material from older, larger impacts that the smaller crater impacted into; testing of the vertical heterogeneity of the uplifted melt could take place. Figure 6.12 (Cintala and Grieve, 1998) shows the minimum depth of origin for central peaks with respect to final crater diameter. These estimates are developed from the notion that the central peak must come from a depth below the zone of melting of the cratering event. Any material above this depth would have been incorporated into the melt. The subsequent craters used for differentiation analyses must lie within the limit of the transient crater because the melt sheet is proposed to be confined within this area (Kring, 2005).

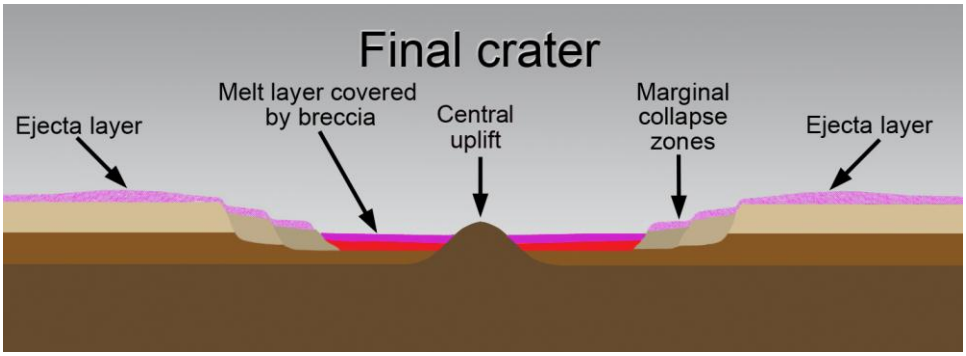

FIGURE 6.11 The structure of a central-peak complex crater. The central uplift is shown to contain originally deeper lithologies (after LPI classroom illustrations).

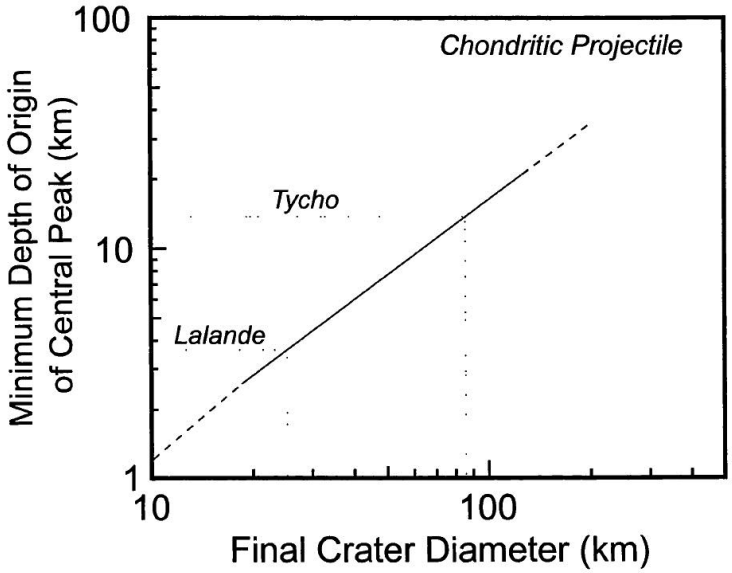

FIGURE 6.12 Minimum depth of origin for lunar central peak material as a function of final crater diameter for an impact velocity of 16.1 km/s (after Cintala and Grieve, 1998).

Ejecta analysis

Another way of using subsequent craters to access the underlying melt sheet is to examine their ejecta. Distal ejecta material would have originated from shallower depths, while material proximal to the crater is

thought to have originated from deeper in the crust (Fig. 6.13). Croft (1985) found that the depth of excavation is ~1/10 of the transient crater diameter. With a reasonable estimate of the transient crater diameter, calculations could be made to ensure that the impact melt of interest was ejected. This same technique was used for site selection on the Apollo 14 mission, the goal of which was to sample the ejecta of the 340 m diameter Cone Crater which was suspected to have excavated material from the Fra Mauro Formation (Imbrium Basin ejecta). The astronauts obtained samples along a traverse towards and away from the crater, acquiring material from varying excavated depths (Kiefer, personal communication). This method, on a larger scale, may prove useful for testing impact melt sheet differentiation. As with the previous method, subsequent excavating craters must lie within the limits of the transient crater to access the melt sheet.

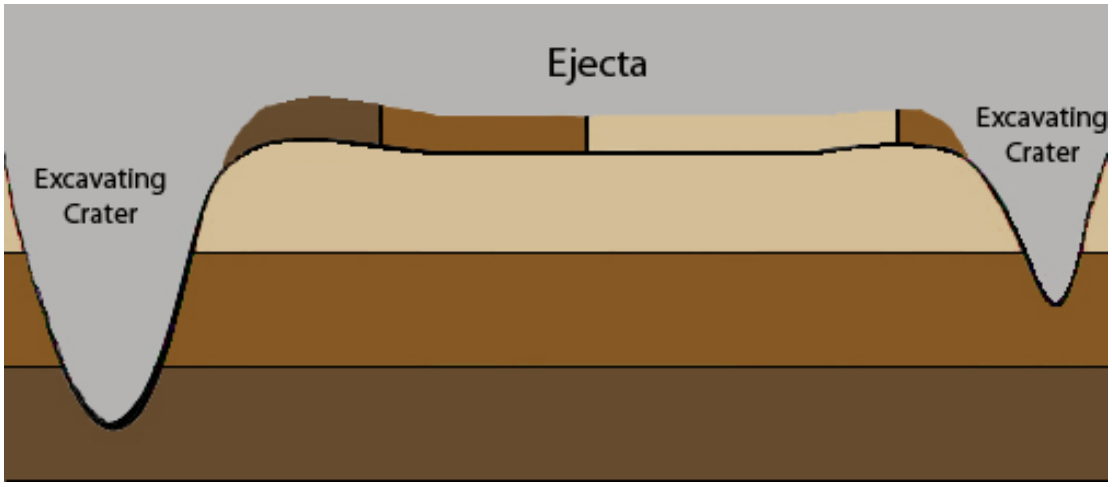

FIGURE 6.13 A schematic representation of the various depths of origin for crater ejecta on the surface. In reality, ejecta will not be separated into such distinct layers as shown.

Drill core analysis

As shown in the discussion of the Manicouagan impact melt sheet, surficial geologic interpretation may not be sufficient to detect differentiation. One way to precisely determine this phenomenon is by drilling into a melt sheet to collect rock core samples. As stated earlier, the differentiated nature of the Manicouagan melt sheet was not discovered until it was drilled. Although this may be out of scope for immediate lunar missions, drilling would be a definitive way to investigate lunar melt sheet differentiation.

Previous Work on Lunar Differentiation

Given the extent of terrestrial erosion and the dynamic nature of Earth's geologic processes, information on melt sheet differentiation is sparse; use of terrestrial melt sheet data to explain the composition and nature of lunar melt sheets, while useful, may not yield correct interpretations.

Spectral analysis of Orientale Basin

Budney *et al.* (1996) studied the melt sheet of the 930 km diameter Orientale Basin for signs of differentiation. Using spectral data from the Clementine UVVIS instrument they mapped radial FeO variations of ejecta from craters excavating Orientale basin floor material to determine if vertical differentiation of Orientale melt took place. Initial results from their study suggested that the Orientale melt sheet is both laterally and vertically homogeneous. This would mean only basins larger than Orientale could potentially contain differentiated melt sheets, dramatically reducing the number of candidate basins (Fig. 6.14). However, the craters excavating basin floor material that were analyzed were located near the margin of the proposed Orientale transient crater. Here the melt sheet is likely to be thinner than at the center of Orientale and heterogeneity may not be as apparent. This study also suggested that a melt thickness of 1 km would be sufficient to see variations in FeO using the MAGFOX program for modeling fractional crystallization.

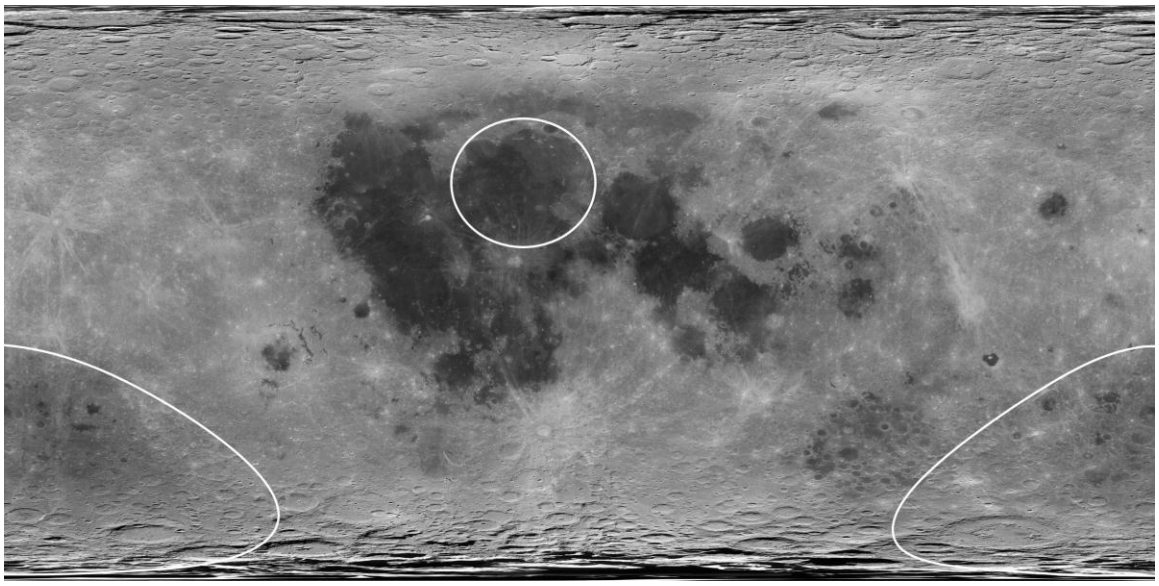

FIGURE 6.14 Imbrium Basin (center) and South Pole-Aitken Basin (lower periphery); the only two basins that may have differentiated melt sheets based on the spectral analysis of Orientale by Budney *et al.* (1996).

Rayleigh calculation for convection

Morrison (1998) proposed that the South Pole-Aitken Basin melt sheet could have been as thick as 226 km, producing a differentiated melt sheet consisting of anorthosites, norites, and possibly ultramafics. The differentiated nature of the SPA melt sheet was prompted by Clementine spectral data of FeO concentrations in the outer ring of Apollo Basin; Apollo is thought to have excavated 28 km into the heterogeneous SPA melt sheet yielding variations of FeO from 10-12%, while the Apollo melt sheet yields FeO concentrations from 6-8%. Morrison (1998) also used the Rayleigh equation to determine if convection and therefore differentiation occurs in an impact melt sheet

$$R = gaBd^4/(hv)\ , \qquad (6.2)$$

where g is the acceleration due to gravity, a is the coefficient of thermal expansion, B is the temperature gradient in excess of the adiabat, d is the thickness of the melt, h is the thermal diffusivity, and v the kinematic viscosity. Using the Rayleigh number, R, approximated from Manicouagan, lunar gravity and viscosities of impact melt estimated from lunar meteorites, an approximate minimum thickness for differentiating melt sheets on the Moon is 1.1 km. If the Rayleigh number is the determining factor, melt sheets in excess of this thickness have the physical dimensions to convect as vigorously as Manicouagan and therefore differentiate. Based on estimates for lunar melt thickness from Cintala and Grieve (1998) (Fig. 6.15), all lunar basins will have a melt thickness >1.1 km and, therefore, based on the Rayleigh criteria, will be thick enough to differentiate (Fig. 6.16).

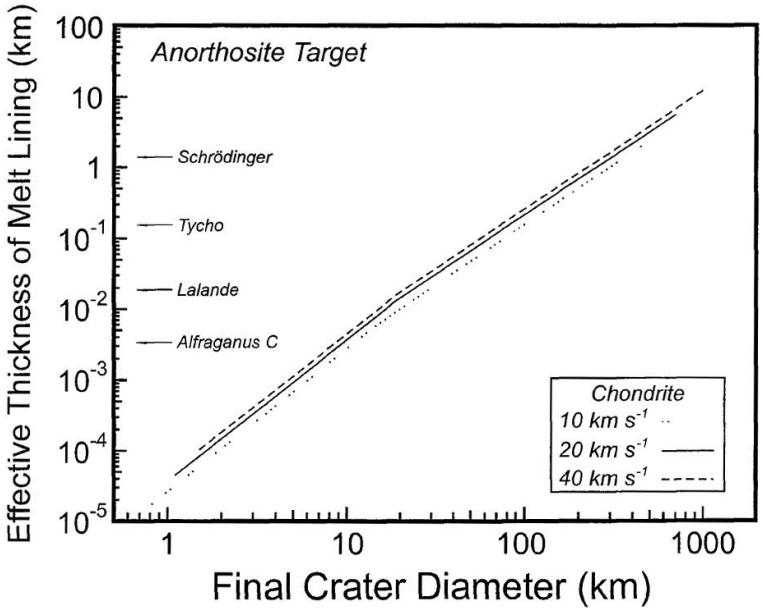

FIGURE 6.15 Effective thickness of the melt lining as a function of final crater diameter (after Cintala and Grieve, 1998).

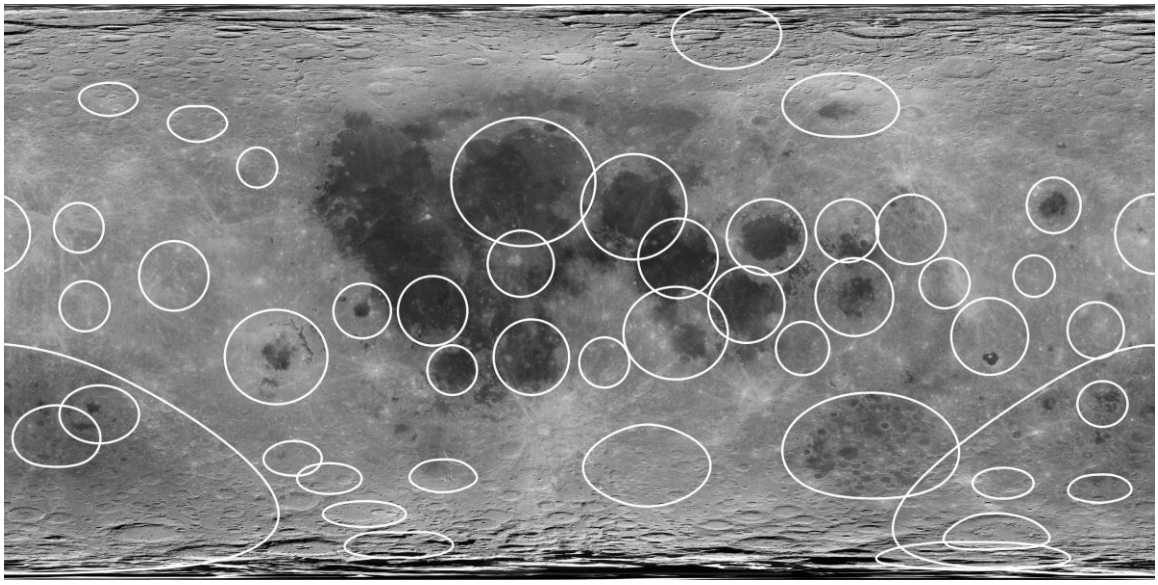

FIGURE 6.16 Basins with melt sheets thick enough to differentiate based on the Rayleigh number criteria.

Spectral analysis of the South Pole-Aitken Basin

Using the Spectral Profiler aboard the Kaguya spacecraft, a study by Yamamoto *et al.* (2010) suggested the SPA Basin has a highly differentiated impact melt sheet consisting of an orthopyroxene layer that overlies an olivine-rich layer. However, a study by Nakamura *et al.* (2009) suggested SPA's melt sheet is largely homogeneous given the spectral similarities of the central peaks in Finsen, Antoniadi, Bhabha and Lyman craters within SPA, despite their different estimated excavation depths.

Requirements

Three requirements are used to select impact sites at which to investigate lunar melt sheet differentiation: certainty of basin existence, the extent of post-basin cratering, and whether those post-basin craters excavated the basin's melt sheet.

Basin certainty

Figure 6.17 shows the location of all named basins on the Moon and classifies them by certainty (after Wood, 2004). Based on this classification, uncertain and possible basins are determined to be unsuitable candidates for testing lunar impact melt sheet differentiation.

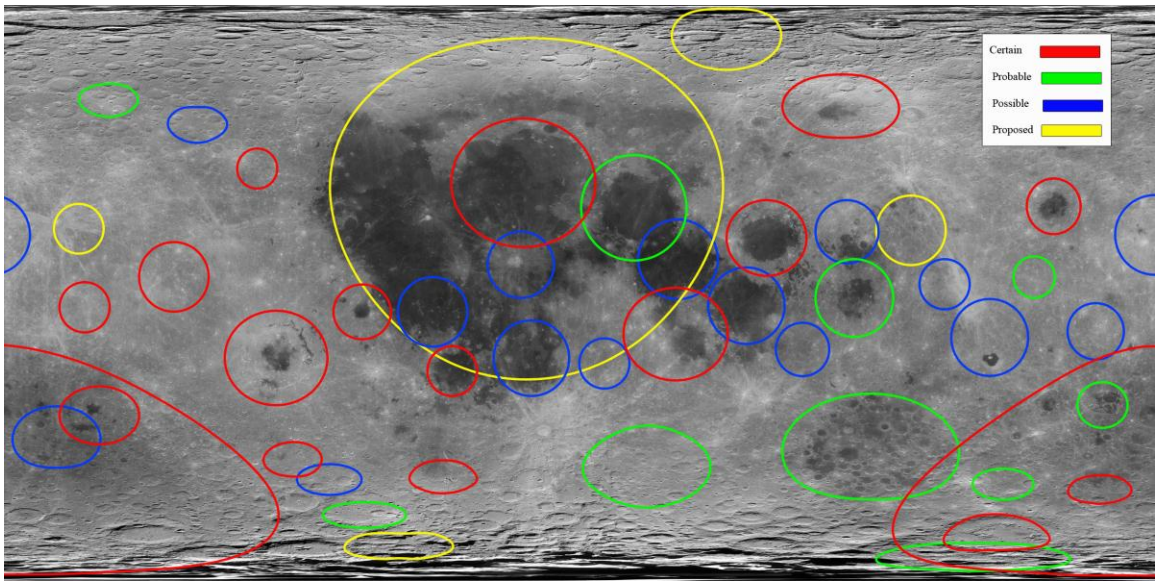

FIGURE 6.17 The spatial extent of lunar basins. Basins are classified by certainty (after Wood, 2004): red, certain; green, probable; blue, possible; yellow, proposed (uncertain).

Post-basin cratering

Post-basin impacts can act as probes into the underlying basin material, such as the melt sheet. Areas with a large number of craters are deemed older than an area with fewer craters; an older surface may offer a greater number of potential probes into the subsurface. Therefore, though some younger and smaller basins like Schrödinger (320 km diameter) are ideal for studying many cratering processes, their younger age means they may not have sufficient post-basin impacts (of a certain size) to test impact melt sheet differentiation. However, the youngest basin, Orientale, may provide access to its melt sheet through post basin-forming cratering simply because of its large size (930 km diameter); a melt sheet with a larger surface area has a greater chance of being subsequently impacted on.

Melt sheet excavation

Not all post basin-forming craters are suitable for testing basin melt sheet differentiation. If a crater is too large it will have a depth of melting which exceeds the underlying basin melt sheet, in which case uplifted central peak material will not contain the basin melt sheet of interest. For instance, models suggest Orientale has a maximum melt sheet thickness of ~10.5 km (Cintala and Grieve, 1998). Assuming only a small amount of regolith has accumulated above the melt sheet since formation, an impact onto Orientale's basin floor forming a crater > 69 km will melt material to a depth greater than that of Orientale's melt sheet. Therefore at Orientale, craters ≤69 km in diameter will be targeted, as these craters will not, in theory, melt material to be a depth greater than Orientale's melt sheet and so can investigate differentiation of the Orientale melt sheet.

Complications

Post-impact regolith accumulations

Models have been produced to determine the amount of regolith accumulated on the lunar surface since the start of the basin forming era. Housen *et al.* (1983) suggest a minimum of ~100 m to a maximum of ~1000 m of material has accumulated, while Pike's (1974) model instead suggests a minimum of ~200 m to a maximum of ~3000 m of material may be blanketing the pre-basin surface (Fig. 6.18) (Petro and Pieters 2008). This will be important when using the method of examining melt sheet material excavated from a post-basin crater. If the basin is old (for example, Nectarian in age) and the crater excavating the basin material is young (Copernican in age), there would likely be a substantial amount of ejecta and regolith that must be penetrated. If the crater is too small it will only excavate regolith material and not the underlying basin melt sheet. Conversely if the basin of interest is relatively young (Imbrian in age) there will be little material between the surface and the melt sheet. Assuming a constant post-basin regolith accumulation rate of 1 mm/yr, the youngest basin (Orientale) would have ~38 m of regolith blanketing its surface.

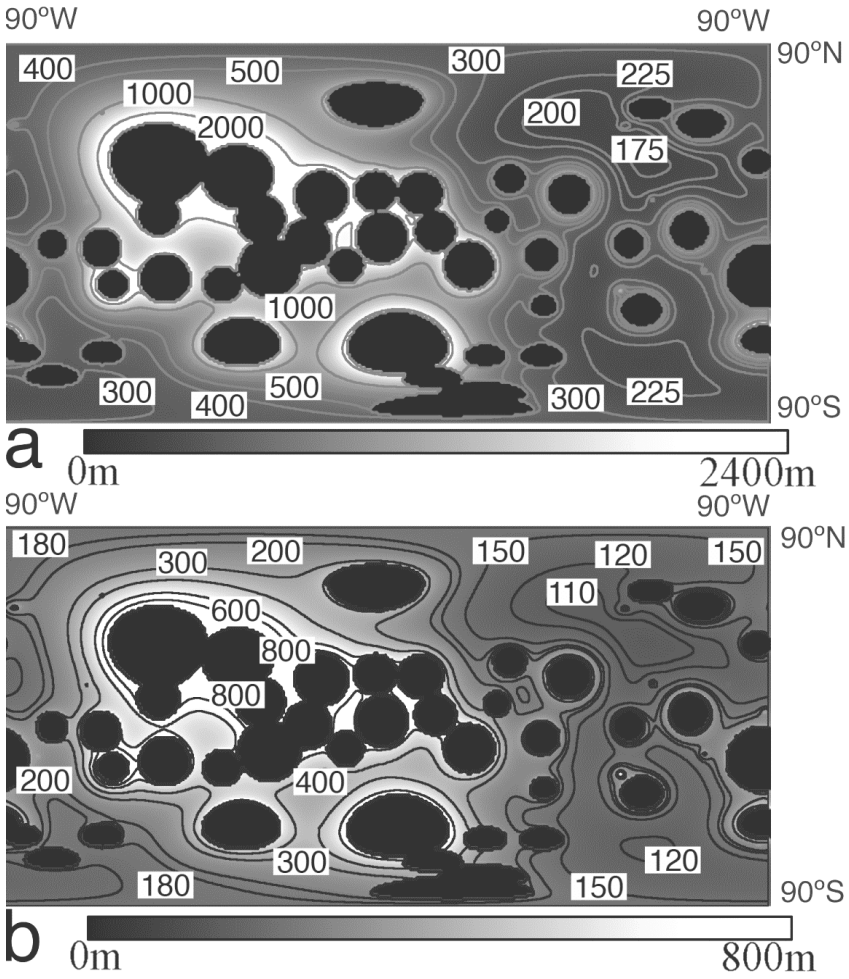

FIGURE 6.18 Cumulative ejecta thickness from 42 impact basins estimated from the calculations of (a) Pike (1974) and (b) Housen *et al.* (1983) (after Petro and Pieters, 2008).

Fallback breccia accumulations

During an impact, material is ejected from the crater, some of which falls directly back into the crater and accumulates atop the melt sheet (Figs. 6.3 and 6.11). This fallback breccia must be considered when calculating the size of crater that is required to excavate the melt sheet. The Sudbury impact melt, for

instance, is covered by a thick (~1.5 km) layer of breccia. If the crater is not of sufficient size it will only excavate breccia and not the melt sheet of interest.

Density relationships

A study by Warren (1993) suggested the density of lunar impact melt relative to the density of the crystals precipitating from the melt could prevent differentiation in all except the largest basins; Warren (1993) implies that buoyant floatation of feldspar crystals would mostly prevent effective differentiation. The average density of lunar impact melt compositions is 2.76 g/cm^3, which is 0.05 g/cm^3 greater than the density of the major liquidus phase, feldspar. The density of the aggregate liquidus phase, feldspar + pyroxene, would be 0.20 g/cm^3 greater than the density of the melt (2.76 g/cm^3). This difference in densities could interfere with convection and therefore differentiation.

SPA Case Study

The highest priority for investigating melt sheet differentiation on the Moon is the South Pole-Aitken (SPA) Basin. SPA is the largest confirmed lunar basin and has been sufficiently excavated by subsequent impacts to allow investigation of the initially deeper lithologies (including basin melt sheet) at or close to the lunar surface. The SPA impact is thought to have sampled material from deep within the Moon making a geochemically complex melt of anorthosites, norites, and perhaps ultramafics (Morrison, 1998), which likely differentiated into layers of varying mineralogy and chemistry. On the other hand, smaller lunar impact events may only have sampled (and melted) upper crustal material and may therefore not have differentiated due to their relative geochemical homogeneity.

Subsequent cratering

SPA contains approximately 45 complex craters (Fig. 6.19) that have well-defined central peaks in high-resolution Clementine data. Fourteen of these are within the 1260 km transient crater diameter estimate (centered at –56°, 170°E) of Petro and Pieters (2002). Using a proportional growth model Spudis (1993) estimated a SPA transient crater diameter of 1160-1470 km. When centered at –56°, 180° (Wilhelms *et al.*, 1979), the lower estimate of Spudis (1993) contains 16 complex craters, while the upper estimate contains 21 with an additional two complex craters straddling its limit (Table 6.2). There are also several large basins within SPA that excavate deep into the proposed ~200 km melt sheet. These large basins would serve to test the nature of SPA's melt sheet and also to constrain the extent of melt sheet differentiation as their own melt sheets could be tested during the process (see chapter on SPA).

Antoniadi crater

There are 11 complex craters with well-defined central peaks that lie completely within all three transient crater estimates for SPA mentioned above. One is of particular interest to several goals in Science Concept 6: Antoniadi Crater. Antoniadi possesses a peak-ring and a well preserved central peak (Fig. 6.39). Its 143 km diameter suggests the central peak came from a depth of ~22.8 km (calculated from Cintala and Grieve, 1998), which provides a glimpse into the mid-upper ranges of SPA's melt sheet.

Melt sheet differentiation at SPA, if proven, would confirm the differentiation of impact-induced melt sheets for the very largest impact events. However, it would also be important to constrain a lower bound on the size of basin that would produce a differentiated melt sheet. Therefore, if SPA, ~2500 km diameter, is confirmed to possess a differentiated melt sheet, basins of gradually smaller sizes should be evaluated.

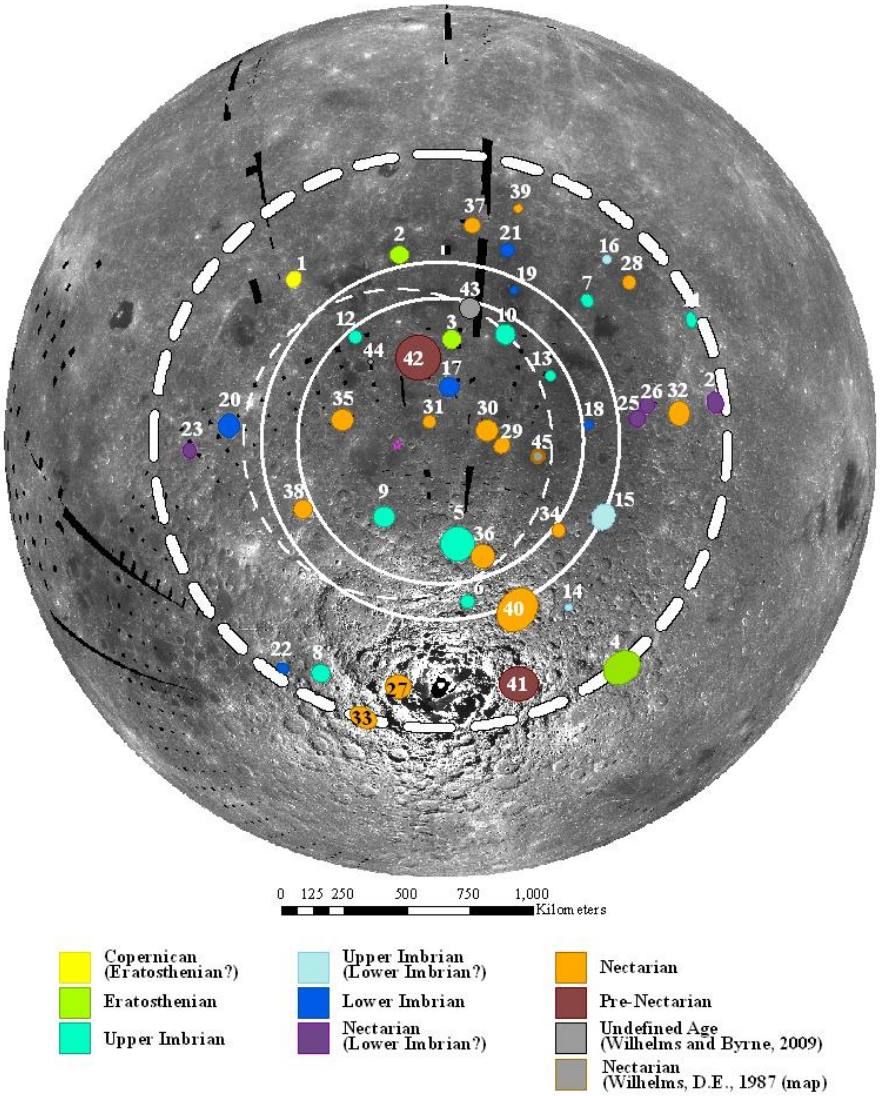

FIGURE 6.19 Locations and approximate sizes of complex craters with discernable central peaks within SPA (large, dashed white circle) (see chapter on SPA). The solid white rings represent the minimum (1160 km) and maximum (1470 km) estimates of transient crater diameter calculated from Spudis (1993) and the smaller dashed white ring represents the size and location of the transient crater as estimated by Petro and Pieters (2002). See Table 6.2 for crater identification information.

TABLE 6.2. Complex craters within SPA that fall within various estimates for the transient crater (TC) diameter, whose central peaks may be used to determine if the SPA melt sheet differentiated. Asterisks indicate craters whose central peaks are barely visible in high-resolution (~100 m/pixel) Clementine data (see chapter on SPA).

ID #	Name	Lower TC estimate calculated from Spudis, 1993 (1160 km)	Upper TC estimate calculated from Spudis, 1993 (1470 km)	Petro and Pieters (2002) TC estimate
1	O'Day			
2	Birkeland			

3	Finsen	X	X	X
4	Hausen			
5	Antoniadi	X	X	X
6	De Forest		X	
7	Dryden			
8	Hale			
9	Lyman	X	X	X
10	Maksutov*	X	X	(partial)
11	Mariotte			
12	Oresme V	X	X	X
13	White	X	X	
14	Doerfel S			
15	Fizeau		(partial)	
16	Plummer M*			
17	Alder	X	X	X
18	Grissom M		X	
19	Oppenheimer U		X	
20	Pauli			
21	Rumford			
22	Wexler			
23	Carver			
24	Langmuir			
25	Leavitt			
26	Leavitt Z			
27	Amundsen			
28	Barringer			
29	Bhabha	X	X	X
30	Bose	X	X	X
31	Boyle	X	X	X
32	Buffon			
33	Demonax			
34	Eijkman		X	
35	Hopmann*	X	X	X
36	Numerov	X	X	X
37	Orlov			
38	Prandtl*		X	X
39	Sniadecki			
40	Zeeman		(partial)	
41	Drygalski			
42	Von Karman*	X	X	X
43	Davisson	X	X	(partial)
44	Oresme Q	X	X	X
45	Stoney	X	X	X

Orientale Case Study

As mentioned earlier, spectral evidence suggests Orientale's melt sheet is not differentiated (Budney *et al.,* 1996). However, the proposed melt sheet thickness (~10.5 km) is far greater than the estimated thickness for differentiation (1.1 km) using the Rayleigh criteria. At 930 km in diameter, Orientale would be a reasonable choice for investigation when down-sizing from SPA.

Subsequent cratering

One problem for testing Orientale is its relatively young age. Being the youngest basin, it has had less time to accumulate post basin-forming craters (which could potentially excavate its melt sheet) compared

to older basins. There are eight craters >5 km diameter within the maximum Orientale transient crater estimate of Melosh (1989) (Fig. 6.20), only two of which are complex and only one, Maunder, contains a central peak.

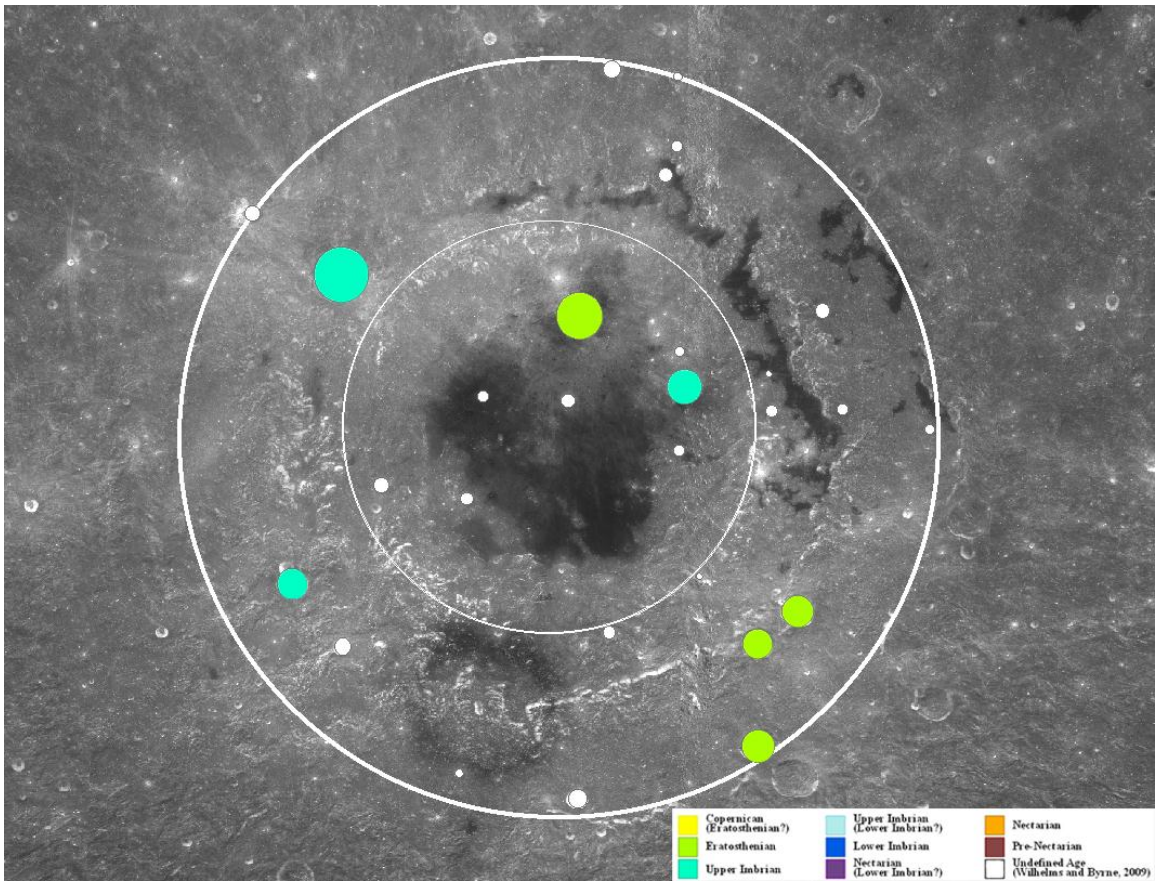

FIGURE 6.20 Location, age, and size of craters within Orientale Basin. The inner white circle represents the transient crater from Melosh (1989); the outer white circle represents the basin rim (930 km diameter). The ages of craters shown by closed white circles are undetermined.

Maunder crater

The largest crater inside the estimated transient diameter of Orientale basin is Maunder. It is a complex crater with a diameter of 55 km suggesting that its central peak originated from a depth of ~7.3 km, therefore within the melt sheet of Orientale. The ejecta blanket of Maunder shows considerable variability compared to that of the surrounding areas and may be estimated for variations in compositions with distance.

If Orientale proves to be differentiated, smaller basins must be tested. Conversely if it does not show differentiation, basins of larger size must be tested to constrain a lower/upper bound on melt sheet differentiation.

Mutus-Vlacq Case Study

The 700 km diameter Mutus-Vlacq Basin would be appropriate for investigation after Orientale. Its diameter suggests a melt sheet thicker than the minimum estimate for differentiation from the Rayleigh criteria. Classified in age group 3 of the pre-Nectarian basins (Wilhelms, 1987) and therefore one of the oldest lunar basins, its formation could have been at a time when the Moon possessed a different (hotter) thermal gradient relative to the younger basins (such as Orientale). It is possible that hotter thermal conditions could have influenced the differentiation of impact-induced melt sheets (initially warmer

conditions would result in a larger impact-induced melt volume for a given impact energy). For example, Mutus-Vlacq, though smaller than Orientale, could possess a differentiated melt sheet on account of the warmer conditions during its formation compared to the cooler conditions during Orientale's formation. This suggests a range of basins with different ages should be studied to infer if possible warmer thermal conditions during the Lunar Cataclysm could have affected the process of melt sheet differentiation.

Subsequent cratering

As a pre-Nectarian basin, Mutus-Vlacq has been subjected to significant cratering over time, increasing the likelihood of post basin-forming impact craters excavating the Mutus-Vlacq melt sheet. In order to guarantee uplift of the melt sheet, post-basin craters ≤55 km in diameter will be considered as possible Mutus-Vlacq melt sheet samplers. Craters larger than this would have a zone of melting that extends deeper than the Mutus-Vlacq melt sheet.

Analysis of an intermediate-sized basin, such as Mutus-Vlacq, would help place a constraint on basin melt sheet differentiation. If the Mutus-Vlacq melt sheet is shown to be differentiated, basins of smaller size will need to be considered. Conversely if it does not show signs of differentiation, basins of larger size should be tested to constrain limits of impact melt differentiation.

Implementation

There are three methods that should be considered as immediate means for testing impact melt sheet differentiation via post basin-forming cratering. The first and most direct method is to traverse a crater central peak, which is estimated to have uplifted the underlying basin melt sheet, taking samples at various locations. The second method is to sample boulders that have fallen down a central peak and lay at its base; Apollo 17 used this method to sample massif material. Boulder tracks can trace the path to locate the original position of the boulder. With a sufficient sample size of boulders, one could potentially examine multiple elevations along the central peak and determine the presence, composition and extent of the melt sheet, and whether it is differentiated. A third, less direct way to test for differentiation is to traverse away from or towards a crater that possibly excavated melt sheet material to test for varying elemental abundances in it's ejecta as a function of crater distance. Deeper lithologies will be concentrated at locations proximal to the crater; shallower lithologies will be concentrated at distal locations (Fig. 6.13).

Conclusion

Lunar impact melt sheet differentiation will be an issue of contention until it is directly assessed with geologic sampling. With the recommendations for site selection and implementation methods discussed here, the question of whether basin melt sheet differentiation takes place, and if so, to what extent, can be definitively resolved.

SCIENCE GOAL 6B: DETERMINE THE STRUCTURE OF MULTI-RING IMPACT BASINS

Introduction

Multi-ring basins are the largest form of impact structure. Evidence of these structures on Earth is contentious, however they have been found and confirmed on many other Solar System bodies including the Moon (Wilhelms, 1987), Mercury and Mars (Pike and Spudis, 1987), and Ganymede and Callisto (Melosh, 1989).

Multi-ring basins were first discovered on the Moon by Hartmann and Kuiper (1962)[1] and defined as "large circular structures with not just one rim but an additional raised ring or rings and a system of radial furrows". Later, Wilhelms (1987) used a size parameter to define lunar multi-ring basins as any impact structure larger than 300 km in diameter. Problems arising from these definitions include potentially classifying peak-ring craters as multi-ring basins from the former, and placing an arbitrary limit on the size of multi-ring basins from the latter. A more concise definition is offered by Melosh (1989) who states, "multi-ring basins possess at least two asymmetric scarped rings one of which may be the original crater

[1] The original paper by Hartmann and Kuiper (1962) is hard to obtain, therefore the reader is directed to Hartmann (1981).

rim". This definition therefore differentiates multi-ring basins (at least two asymmetric scarped rings) from peak-ring craters (only one asymmetric escarpment), and does not place an arbitrary size constraint on basins. Added to this definition is the caveat that at least one of the rings must form outside of the final crater. These outer rings generally resemble scarps, are asymmetric in shape, and locally disrupt material. It has been observed that adjacent basin rings appear to be spaced at a ratio of $\sqrt{2}$ (Baldwin, 1963; Hartmann and Wood, 1971); the validity of this geometric spacing remains unclear. Lunar multi-ring basins are thought to have formed early on in the Solar System's history, many within a period of a few hundred million years approximately 4 Ga. This period is known as the Lunar Cataclysm (Tera *et al.*, 1974).

These 'lunar' multi-ring basins are not the only multi-ring basin type; another is the Valhalla-type basin named after the Valhalla multi-ring basin on Callisto. These basins contain tens to hundreds of closely spaced outward facing scarps. These basins are not discussed further here; for more information see Melosh (1989).

Spudis (1993) outlines five criteria for recognizing lunar basins: 1) presence of strongly expressed concentric scarps, 2) arcuate chains of massif (isolated or associated with textural ejecta deposits), 3) arcuate chains of massifs in association with wrinkle ridges within maria, 4) circular arrangements of complex, wrinkle-ridge systems, and 5) isolated massif scarps/ridges that collectively occur more or less at a constant radial distance from a central point.

A Lunar Multi-Ring Basin – Orientale

The first multi-ring basins were discovered on the Moon (Hartmann and Kuiper, 1962). Twenty five years later, Wilhelms (1987) had identified 45 lunar impact structures as definite, probable or possible multi-ring basins. The most prominent and best preserved of these basins is Orientale. Located on the western limb of the nearside, Orientale contains at least four ring structures encompassing a diameter of 930 km making it one of the largest lunar impact structures. Relative ageing suggests Orientale is the youngest multi-ring basin with an estimated age of 3.82 Ga (Wilhelms, 1987). Being the youngest basin, it is well preserved compared to other, older basins.

Orientale's ring structures are clearly visible at radial distances of 465 km (Montes Cordillera), 310 km (Outer Rook Mountains) and 240 km (Inner Rook Mountains) from its basin center, with another less prominent ring, here referred to as the Inner Shelf Ring, at a radial distance of 160 km. Outside of the Montes Cordillera lays the Hevelius Formation; between the Rook Mountains is the Montes Rook Formation and within the Inner Rook Mountains lays the Maunder Formation (Fig. 6.21). Gravity modeling suggests the center of the basin sits ~3 km below the lunar geoid, with the basin possessing a vertical height range of 5–6 km (Mohit and Phillips, 2006).

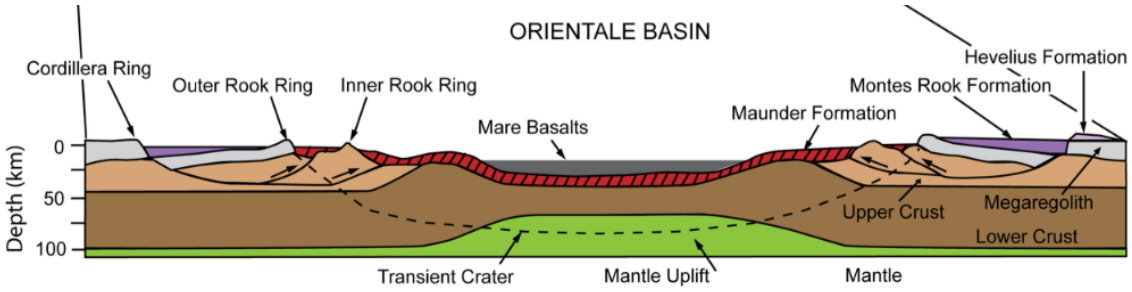

FIGURE 6.21 A cross-section through the Orientale Basin. The Inner and Outer Rook rings, as well as the Cordillera Ring are clearly visible. The crust has been thinned under the basin center resulting in uplift of the Moho (the crust/mantle boundary). In this model the rings are composed of either megaregolith or upper crustal material. The upper crust has been completely removed around the basin center *(*after Head *et al.* 1993; modified from LPI classroom illustrations).

Orientale's inner most zone, the Maunder Formation, is interpreted as Orientale's impact melt sheet (Bussey and Spudis, 2000) while the compositionally similar outermost zone, the Hevelius formation, is interpreted as impact ejecta which is thought to be highly feldspathic in composition (Spudis *et al.*, 1984).

Between these two, the Montes Rook Formation has a weak mafic signature (Head *et al.*, 1993), suggesting a deeper crustal composition. The most topographically prominent ring is the Montes Cordillera, which would suggest this represents the final crater rim. However, pre-impact structures have been recognized relatively intact between the Cordillera and Outer Rook (Spudis, 1993) implying the Cordillera Mountains are placed outside of the crater rim and are therefore an outer ring structure. The crust beneath the center of Orientale appears to be thinned relative to the crust outside of the basin. Gravity estimates suggest a crustal thickness between ~0 km (Hikida and Wieczorek, 2007) and 15 km (Wieczorek and Phillips, 1999) at the basin center; Wieczorek *et al.* (2006) suggest the entire upper crust is absent below the basin center.

A (Possible) Terrestrial Multi-Ring Basin – Chicxulub

On Earth, three impact structures are considered possible multi-ring basins: Vredefort, Sudbury, and Chicxulub. Of these three, Vredefort and Sudbury formed ~2 Ga and are therefore severely degraded preventing extensive analysis of their structure. Chicxulub on the other hand is a relatively young, 65 Ma, impact structure and its links to the Cretaceous-Tertiary mass extinction (Alvarez *et al.*, 1980; Hildebrand *et al.*, 1991) means it has been studied intensely.

The Chicxulub impact crater is located on the Yucatán Peninsula, Mexico and is ~150-200 km in diameter (Morgan and Warner, 1999) (Fig. 6.22). The crater is buried under a kilometer of Tertiary sediments (Morgan *et al.*, 1997) therefore its structure has been inferred from seismic, gravity and magnetic surveying. This surveying suggests Chicxulub contains a peak ring, a main rim, and an outer ring; a second exterior ring with a diameter of ~250 km has also been proposed (Fig. 6.22). Based on these observations, Chicxulub may well represent a terrestrial equivalent to the Orientale Basin, and other multi-ring basins found in the Solar System.

Morgan *et al.* (2000), from their analysis of gravity and seismic data, suggested the Chicxulub peak ring contains highly brecciated and altered central peak material or allogenic impact breccias. The seismic data also suggests the peak ring is underlain by slump blocks and bounds the lateral extent of the central melt sheet.

The main topographic rim of Chicxulub has a diameter of ~150 km. The rim itself is asymmetric with a steep inward facing slope and a gentle back slope, in contrast to the peak ring. The main rim is also a head scarp within which are a number of terraces which have slumped inwards along normal faults; occasional up-thrust slumps are also present (Gulick *et al.*, 2008). The slumps are covered by a thin veneer of impact melt and ejecta material.

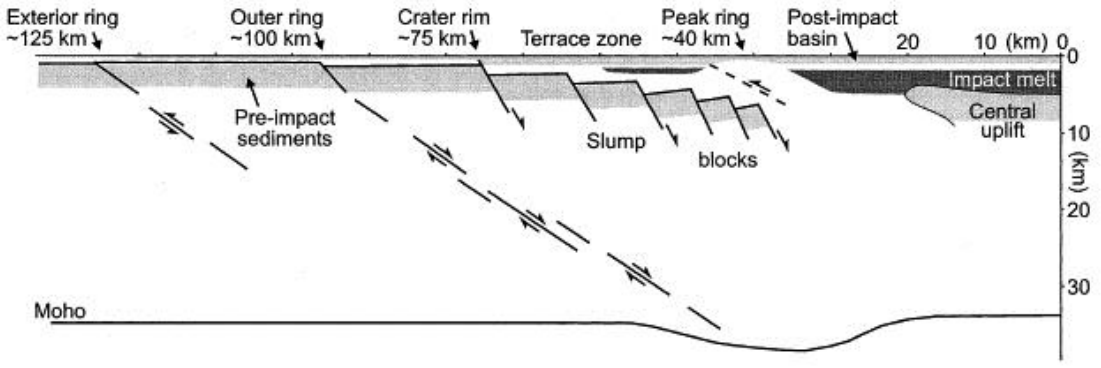

FIGURE 6.22 A cross-section through the Chicxulub impact structure (after Morgan *et al.* 2000). The peak ring is found ~40 km from the basin center and contains a thrust feature with originally deep-seated crustal material overlaying normally faulted slump blocks which collapsed off the crater wall. The crater rim occurs at ~75 km and the outer ring at ~100 km. The outer ring is the surface structure of a deep-seated normal fault. A second outer ring is thought to be ~125 km from the basin center. The Moho (crust/mantle boundary) appears to be thickened beneath the peak ring and thinned below the basin center.

Outside of the main crater rim, another ring structure is found at a diameter of ~200 km. As with the crater rim this ring is faulted normally and possesses an asymmetric profile with a gently sloping backslope. However, unlike the crater rim, there are no terrace slump structures associated with this outer ring. Beneath the impact structure the Moho appears to be uplifted by a distance of 1 km at the basin center, and thickened adjacently by a value of ~1.25–1.5 km (Christeson *et al.*, 2001).

Formation of Multi-Ring Basins

As noted above, the mechanism responsible for the modification of complex craters and multi-ring basins, and their resulting ring structures, is unclear. Based on photogeology, spectroscopic data, and gravity data from lunar multi-ring basins, various theories have been proposed to explain multi-ring basin formation; these are outlined below.

Megaterrace hypothesis

The megaterrace hypothesis (Head, 1977; Fig. 6.23, left) suggests ring structures in multi-ring basins are the result of transient crater collapse. The formation of the transient crater weakens target material resulting in the inward collapse of material creating a 'mega' terrace. The edges of these terraces form the basin ring structures.

Nested melt cavity hypothesis

The nested melt cavity hypothesis (Head, 2010; Fig. 6.23, right) in some ways builds upon the earlier megaterrace hypothesis and work by Cintala and Grieve (1998). Here, inwards movement of target material along the edge of the displaced zone (the zone of material affected by the impact) results in the uplift of the transient crater floor. Collapse at the edge of the displaced zone forms the outer ring; inward and upward movement forms the peak rings, which are composed of highly shocked, partially molten, shallow crustal material.

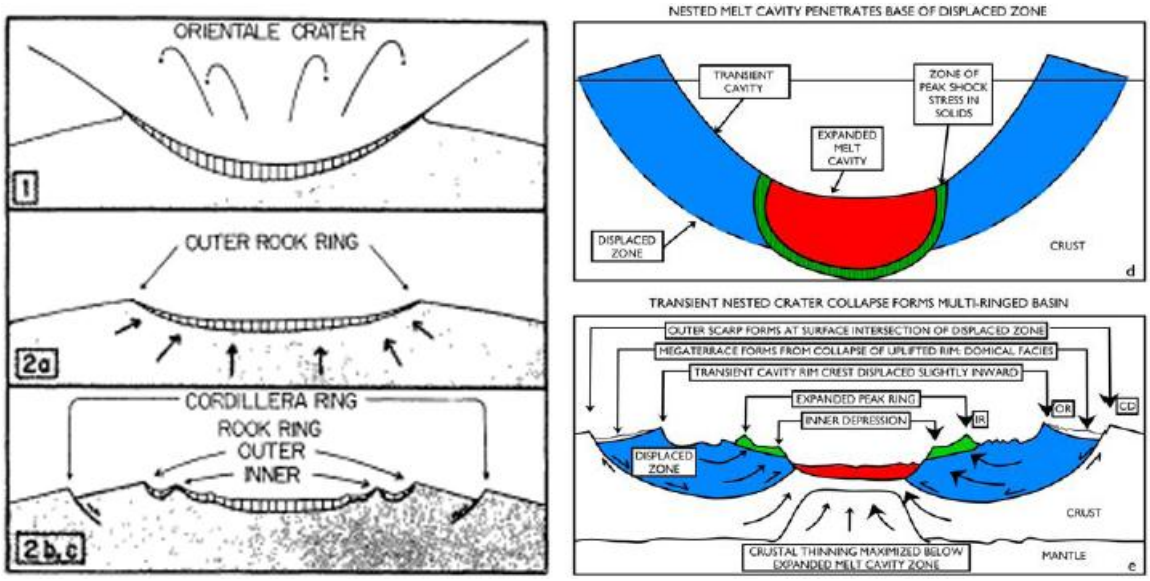

FIGURE 6.23 Left: The Megaterrace hypothesis for basin formation (after Head, 1977). The Outer Rook Ring marks the final crater rim. This forms in a zone of weakness and results in normal faulting which forms the Cordillera Ring outside and the Inner Rook Ring within. Right: The nested melt cavity hypothesis (after Head, 2010) based Orientale. On formation of the transient crater (top image), collapse occurs at the edge of the displaced zone (bottom image) forming a megaterrace resulting in the formation of ring structures. Inner ring structures form from the uplift of shallow crustal material from the edges of the melt zone. (IR: Inner Ring, OR: Outer Ring, CD: Cordillera).

Nested crater hypothesis

The nested crater hypothesis (Hodges and Wilhelms, 1978; Fig. 6.24) suggests rings are formed at strength boundaries within the crust. The transient cavity penetrates layers of varying strength creating bench structures. The crater subsequently undergoes isostatic re-adjustment following its formation, rising up and creating prominent topographic features from the strength boundaries – the ring structures. The innermost ring represents the deepest strength boundary layer; the outermost rings represent the shallower strength boundaries. Slumping may occur at the rims of the 'nested' craters forming additional ring-like structures.

Volcanic modification

Volcanic modification (Hartmann and Yale, 1968) (Fig. 6.25) suggests subsidence in ring faults around the basin, induced by later subsurface melting or intrusions below the crater result in the formation of ring structures both inside and outside of the original crater. However, geological evidence suggests ring formation occurs almost instantaneously in the impact process. At Orientale for example, evidence suggests that suevite, a form of impact breccia, laps up against the Rook Mountains implying the rings formed prior to the suevite hardening. Volcanic modification assumes some kind of volcanic activity within the crater, however many large farside basins lack volcanic mare deposits, in contradiction to this theory.

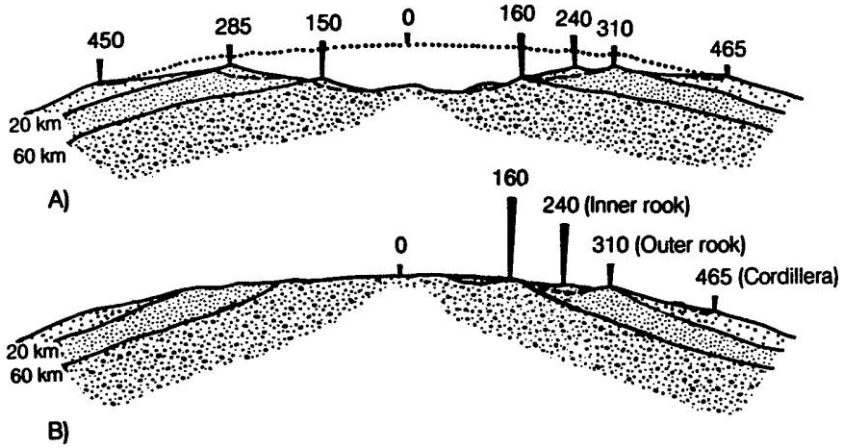

FIGURE 6.24 The nested crater hypothesis modeled on Orientale Basin (after Hodges and Wilhelms, 1978). Strength boundaries within the crust are exposed during impact forming benches (A). These are pushed upwards and outwards through isostatic re-adjustment, forming the various ring structures (B). The outermost ring represents the extent of the transient crater.

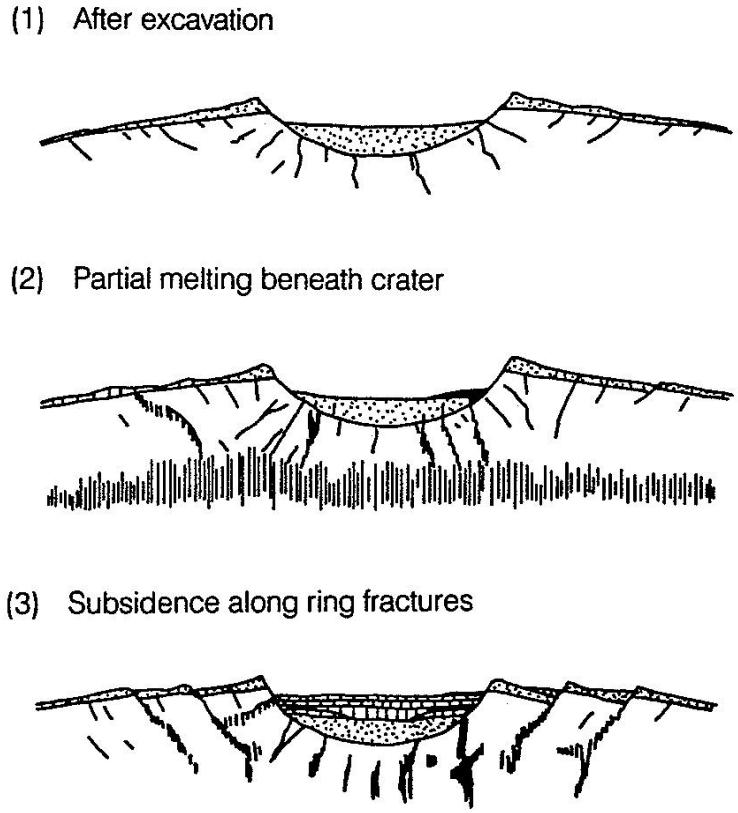

FIGURE 6.25 The volcanic modification hypothesis (after Hartmann and Yale, 1968). Following crater excavation, partial melting occurs beneath the crater (2), which results in subsidence along ring faults (3) creating the ring structures.

Tsunami wave motion

The formation of rings by tsunami-like motions (Baldwin, 1972; Murray, 1980) has also been suggested. Wave oscillations from the initial impact move through the transient crater or alternatively target material becomes fluidized. Eventually the sloshing material 'freezes' into place producing rings. However, the concept of fluid material suddenly 'freezing' in place was not well received. A more physical explanation was proposed by Melosh (1979): acoustic fluidization. In the acoustic fluidization theory, the target material behaves as a Bingham fluid (Bingham, 1916); it deforms either as a plastic or viscous material depending on the applied shear stress. If the shear stress exceeds the material's cohesive strength then the material will flow with a viscosity in a fluid-like manner, allowing the creation of central peaks and peak rings. Once the shear stress drops below the cohesive strength the material once again deforms plastically, its motion ceases and the material becomes 'frozen' into place.

Interaction/collision

The theory that peak-rings contain originally deep-seated material has mainly arisen from studies at Chicxulub. Brittan *et al.* (1999) suggests the peak ring is formed from the collision/interaction of upward/outward collapsing central peak material and inward/downward collapsing material from the crater wall. This results in the peak ring containing deep-seated (lower) crustal material (which had been brought up in the impact by the central uplift) overlying shallow (upper) crustal material which had simply slumped off the crater wall (Fig. 6.26). Seismic studies at Chicxulub showed the peak-ring contained highly brecciated and altered central peak material underlain by slump blocks (Morgan *et al.*, 2000), which agrees with this interaction/collision hypothesis. Spectroscopic analysis of the rings at Orientale also suggests peak-rings are composed of originally deep-seated material (Bussey and Spudis, 1997).

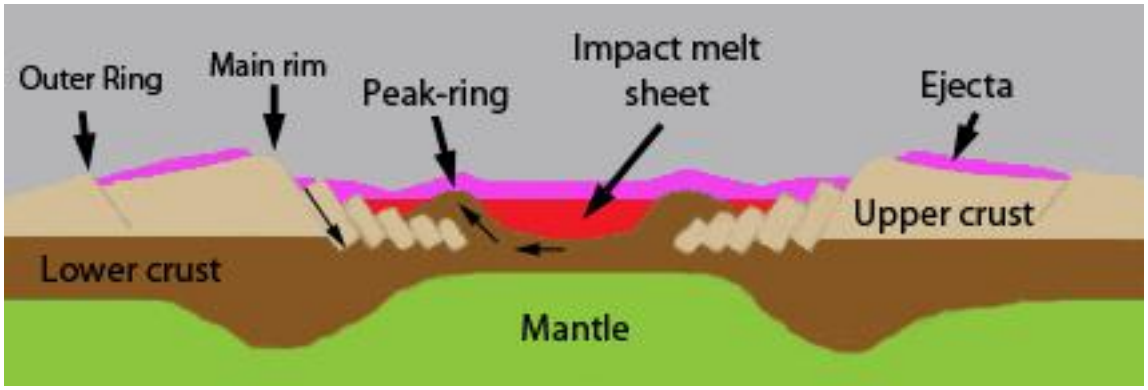

FIGURE 6.26 Peak ring formation through collision/interaction (modified from LPI classroom illustrations). The peak-ring is formed through the outwards motion of the collapsed central peak and the inwards collapse of the crater rim. This forms a type of thrust feature with lower crustal material overlying upper crustal material.

Ring tectonics

Ring tectonics (Melosh and McKinnon, 1978; Melosh, 1989) deals specifically with the formation of outer rings. In this hypothesis the thickness and strength of the lithosphere as well as the viscosity of the asthenosphere and the depth of the transient crater are the factors controlling outer ring formation. Penetration through the lithosphere into the underlying (more fluid) asthenosphere by the transient crater will result in the flow of asthenospheric material towards the basin center. The inward flow of the asthenosphere exerts a drag on the lithosphere; a weak enough lithosphere may fracture under this force forming ring faults, the surface traces of which are the outer rings (Fig. 6.27). The apparent $\sqrt{2}$ ring spacing of multi-ring basin rings can also be explained by this mechanism. The faults will form to relieve stress, but will only form at an appropriate distance from the rim diameter. Shear stresses at the base of the lithosphere will prevent the rings forming too close to the crater rim as they need to act over a broad area to build up large extensional stress. At great distances the inward directed forces which would cause the scarps can be resisted. Therefore, the rings form at an appropriate distance from the crater rim, which is normally 1.3–1.6, crater radii away, approximately $\sqrt{2}$. This differs from the megaterrace hypothesis as it requires penetration into the asthenosphere and allows for the formation of more than one ring outside of the crater rim.

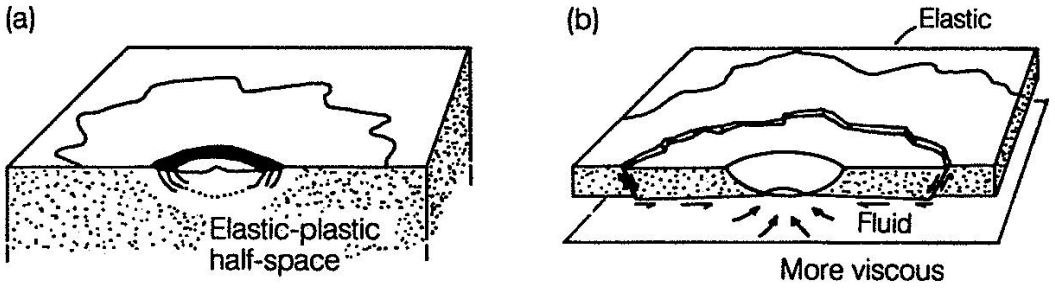

FIGURE 6.27 The ring tectonic theory (after Melosh and McKinnon, 1978). In a thick lithospheric target, ring structures will not form outside of the crater rim (a). In a thinner lithospheric target, penetration into the asthenosphere below results in fluid inflow and the formation of rings outside of the crater rim (b).

All of the theories attempting to explain multi-ring basin formation outlined above have their weaknesses. For example, the megaterrace hypothesis cannot account for more than one ring forming outside of the basin. The nested crater hypothesis is reliant on the strength of the target, not the crater size, and implies that if layers are at a constant depth within the Moon then all basins would have rings at the same radial distances; photogeology implies this is not the case. This model also assumes the topographic basin rim represents the original crater rim, which does not seem to be the case for Orientale (*e.g.* Head *et al.,* 1993). Contradictions also occur between models. For example the interaction/collision model suggests the formation of the peak-ring through the interaction of the collapsing central peak and slump structures. Contrasting this, the nested melt cavity hypothesis suggests that the peak-ring is formed solely by vertical motion, and that no central peak forms in basin-sized impacts.

Scaling Laws and the Transient Crater

As previously mentioned, scaling laws have been developed to link impact structures at all scales on any target body. However, the accuracy of scaling laws for predicting features of the very largest impact structures, multi-ring basins, is uncertain. One notable scaling law, based on data from complex terrestrial and lunar craters, relates the final crater diameter D, to the transient crater diameter D_{tc} (Croft, 1985):

$$D_{tc} = D_q^{\,0.15\pm0.04}\, D^{\,0.85\pm0.04}, \qquad (6.3)$$

where D_q is the transition diameter between simple and complex craters, all values are in kilometers. The importance of the transient crater lies in the ability to estimate depth and volume of excavated material as well as the impact energy from it. If one knows the final crater diameter, the transient crater diameter can be calculated from Equation 6.3, which can then be used to calculate melt volume and depth as well as excavation depth. The ratio of excavation depth to transient crater diameter, based on Z-model results and somewhat limited field data, is approximated to be 0.1. This is believed to be valid for both simple and complex craters. The use of this law to estimate transient crater diameters for multi-ring basins is problematic as it assumes craters at all scales obey the same relationship. Croft (1985) notes, however, that the collapse environment producing rims is apparently the same in both complex and multi-ring structures, suggesting that complex crater scaling can be applied to the larger multi-ring basins.

Assuming the 0.1 depth/diameter ratio is valid for multi-ring basin scale impacts, then the larger the basin, the greater the depth of excavation. It is therefore possible that multi-ring basins may have excavated mantle material, which numerical models suggest is the case for the largest multi-ring basin, South Pole-Aitken (SPA) (Hammond *et al.,* 2009; Potter *et al.,* 2010). If true, sampling of mantle material on the lunar surface would dramatically aid understanding of the Moon's interior as well as planetary differentiation. However, there is no confirmed geological evidence of any lunar basin penetrating into or excavating mantle material (*e.g.* Wieczorek and Philips, 1999; Hikida and Wieczorek, 2007)

Wieczorek and Phillips (1999) suggested that basins up to 500 km in diameter follow proportional scaling laws, but that the largest basins do not. For example, using Equation 6.3 assuming a simple-to-complex transition diameter of 18 km and final crater diameter of 2500 km, the transient crater for SPA is estimated to be 1190 km. However Petro and Pieters (2002), using orbital spectroscopic data, estimated the transient crater of SPA to be 1260 km based on the innermost occurrence of upper crustal anorthosite

crustal material which they believe bounds the edge of the transient crater (the transient crater removed all upper crustal material within its limits). For Orientale, Equation 6.3, assuming an 18 km simple-to-complex transition and a 930 km final crater diameter, predicts a transient crater 515 km in diameter. Alternative techniques using excavation (transient) cavity reconstruction based on gravity-derived crustal profiles estimated transient cavities with diameters of 383 km (Hikida and Wieczorek, 2007) and 397 km (Wieczorek and Phillips, 1999). This suggests scaling laws may be a useful first estimate for transient crater sizes (and other basin features) however *in situ* studies would be required to test estimates of the various methods.

Data collection: Testing the Hypotheses

Two primary data collection methods can be employed to test and investigate multi-ring basin structure: geological sampling and geophysical surveying. Geological sampling can be used to infer the near-surface compositions of structures, contact boundaries at outcrops and fault features, whereas geophysical surveying can probe the subsurface and infer features at greater depth, possibly the crust/mantle boundary (the Moho).

Peak ring structure and formation

According to the theories outlined above, peak rings may either be composed of shallow crustal material or deep crustal material. Geological sampling of ring material will be able to infer a depth of origin and therefore test these models. Sampling can be undertaken on the slopes of peak rings or from boulders at the base of the peaks, if slopes are too steep for lunar rovers or crew to traverse. Samples should be taken on either side of the peak ring for comparison. The peak ring may well be discontinuous and contain (smaller) isolated massif structures; these massifs may be more accessible for traversing and sampling. Seismic surveys can also be used to infer the subsurface structure including contact boundaries, fault and slump structures, and the location of the Moho. Jointly, the geological and geophysical data can be used compile evidence for or against the proposed formation mechanisms for peak rings.

Outer ring structure and formation

At outer rings, geological surveying could locate fault structures, identify compositional features as well as note the amount of fault movement and fault type. Seismic surveying could infer subsurface structures.

Transient crater estimations

The transient crater is an ephemeral feature and so cannot be directly sampled. However features can be used to infer upper and lower limits for the transient crater diameter. Scaling laws can be used to initially estimate the transient crater diameter. Field studies around this estimated diameter could then be undertaken to locate any pre-impact structures. The presence of pre-impact structures would place an upper bound on the transient crater diameter, as all pre-impact surface features within the transient crater would be destroyed during impact. If particular upper crustal lithologies were missing from the basin center, the first occurrence of these could also help place a boundary on the transient crater (the first occurrence would mark the edge of the transient crater).

Quantitative data to collect

Scaling laws have been used to estimate multi-ring basin features, however their validity at multi-ring basin scale is questionable. Therefore, it is important to try to quantitatively assess a basin's features and in turn the accuracy of the scaling laws. Features which can possibly be quantified are the extent and thickness of a melt sheet and, possibly, whether it has differentiated. This could be sampled through excavated or uplifted material from smaller, younger impacts. Ring dimensions as well as fault zone widths could also be collected to help determine basin structure.

Basin ages are not well constrained, and most are dated relative to one another. It would therefore be important to sample basins to produce definitive ages; this would help constrain timing of the proposed Lunar Cataclysm. A geological anchor on the Cataclysm would be provided by dating the youngest basin, Orientale, and the oldest basin, SPA, and a basin of intermediate age, such as Nectaris.

Table 6.3 outlines the sample locations at which various multi-ring basin formation hypotheses can be tested; Table 6.4 list various tests which can be carried out at these locations to gain evidence either for or against the hypothesis. Some hypotheses will be easier to test than others. For example, testing the ring

tectonics theory will be extremely difficult. The best way to test this is through numerical modeling of impacts investigating how the thickness of the lithosphere affects the formation of outer-ring structures. The method of acoustic fluidization (Melosh, 1983) to produce peak rings also cannot be tested at ground level, and will also require numerical modeling to investigate whether this process can be used to accurately re-create well studied terrestrial and lunar impact structures.

TABLE 6.3. Summary of sample locations and the hypotheses which can be tested their (marked by a ✓).

Hypothesis → **Sample location ↓**	*Interaction/ collision*	*Megaterrace*	*Nested Crater*	*Nested Melt Cavity*	*Ring Tectonics*	*Volcanic Modification*
Peak-ring	✓	✓	✓	✓		✓
Main Rim	✓	✓	✓	✓		✓
Outer Ring		✓	✓	✓		✓

TABLE 6.4. Summary of testable questions and whether these will provide evidence for or against the various formation hypotheses. Boxes left blank indicate the test will not provide any useful feedback on the hypothesis.

Hypothesis → **Test ↓**	*Interaction / collision*	*Megaterrace*	*Nested Crater*	*Nested Melt Cavity*	*Ring Tectonics*	*Volcanic Modification*
Peak-ring material derived from shallow depths	against	for	for	for		for
Peak-ring material derived from great depths	for	against	against	against		against
Deep material overlays shallow material in peak rings	for	against	against	against		
Slumps blocks are evident under peak ring	for					
Evidence of listric faulting in ring structures	against	for		for		
Pre-impact features are persevered within the outermost ring			against			
>1 ring outside of original crater rim		against	against	against		

Recommendation Criteria and Results

Based on the multi-ring basin studies of Wilhelms (1987), Pike and Spudis (1987) and Spudis (1993), with additions from Cook *et al.* (2000, 2002), a total of 53 lunar multi-ring basins were identified for consideration in this study (Fig. 6.28) (see Appendix A for additional basin data). In order to identify the basins most suitable to determine the structure of multi-ring basins, a systemic analysis was undertaken, taking into account basin age, location, size, individual attributes (presence of a peak-ring, outer-ring etc.) and certainty.

Temporal distribution and basin modification

Lunar multi-ring basins are either pre-Nectarian (~4.5–3.92 Ga), Nectarian (~3.92–3.85 Ga) or Imbrian (~3.85–3.2 Ga) in age. Orientale, an Imbrian basin, is the youngest basin with an estimated age of 3.82 Ga. SPA, a pre-Nectarian basin, is the oldest; but does not have a definitive age (age estimates vary between 4.4–3.9 Ga; Ryder *et al.*, 2000). Due to the Moon's thermal evolution basins forming in different geological time periods may have impacted into different thermal regimes thus affecting their structure and subsequent evolution. Over time, basins lose their characteristic topographic and crustal profiles through a process known as viscous relaxation. Older basins are therefore more likely to have lost their features through viscous relaxation compared to the younger basins. Evidence of this viscous relaxation can be seen in the gravity-derived basin profiles from Hikida and Wieczorek (2007) (Fig. 6.29); young basins appear to have maintained their crustal and topographic profiles over time, while the older basins lack the characteristic crustal thinning.

The relaxed and degraded state of the (early) pre-Nectarian basins studied by Hikida and Wieczorek (2007) suggests that pre-Nectarian basins are not viable basins to investigate the structure of multi-ring basins. Compounding this, many of these basins possess only one or two ring structures (a probable consequence of their relaxation and degradation). In contrast the younger Nectarian and Imbrian basins (as well as late pre-Nectarian basins) appear to have retained their structure and ring features, making them the best candidates to sample to determine the structure of multi-ring basins.

In terms of basin evolution, analysis of the current rheological and mechanical structure of basins can be used to infer the thermal regime at the time of formation (Mohit and Philips, 2006). The early pre-Nectarian basins would therefore be useful for investigation in terms of basin evolution due to their relaxed state. Similarly the younger basins could also be analyzed to infer the thermal state of the Moon within younger periods. Science Concept 6 does not deal with the evolution of multi-ring basins, however this issue should be considered for future investigations.

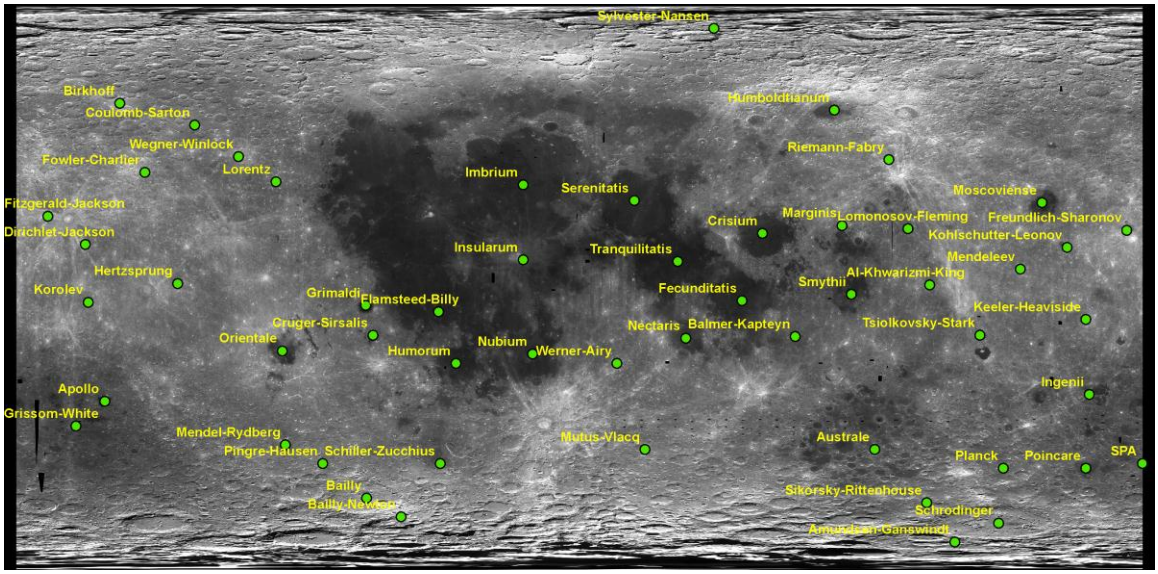

FIGURE 6.28 A global Mercator projection showing the spatial extent of the 53 lunar multi-ring basins (Wilhelms 1987; Pike and Spudis 1987; Spudis 1993; Cook *et al.* (2000, 2002). The green points represent the basin centers. Basemap is a UVVIS Clementine image.

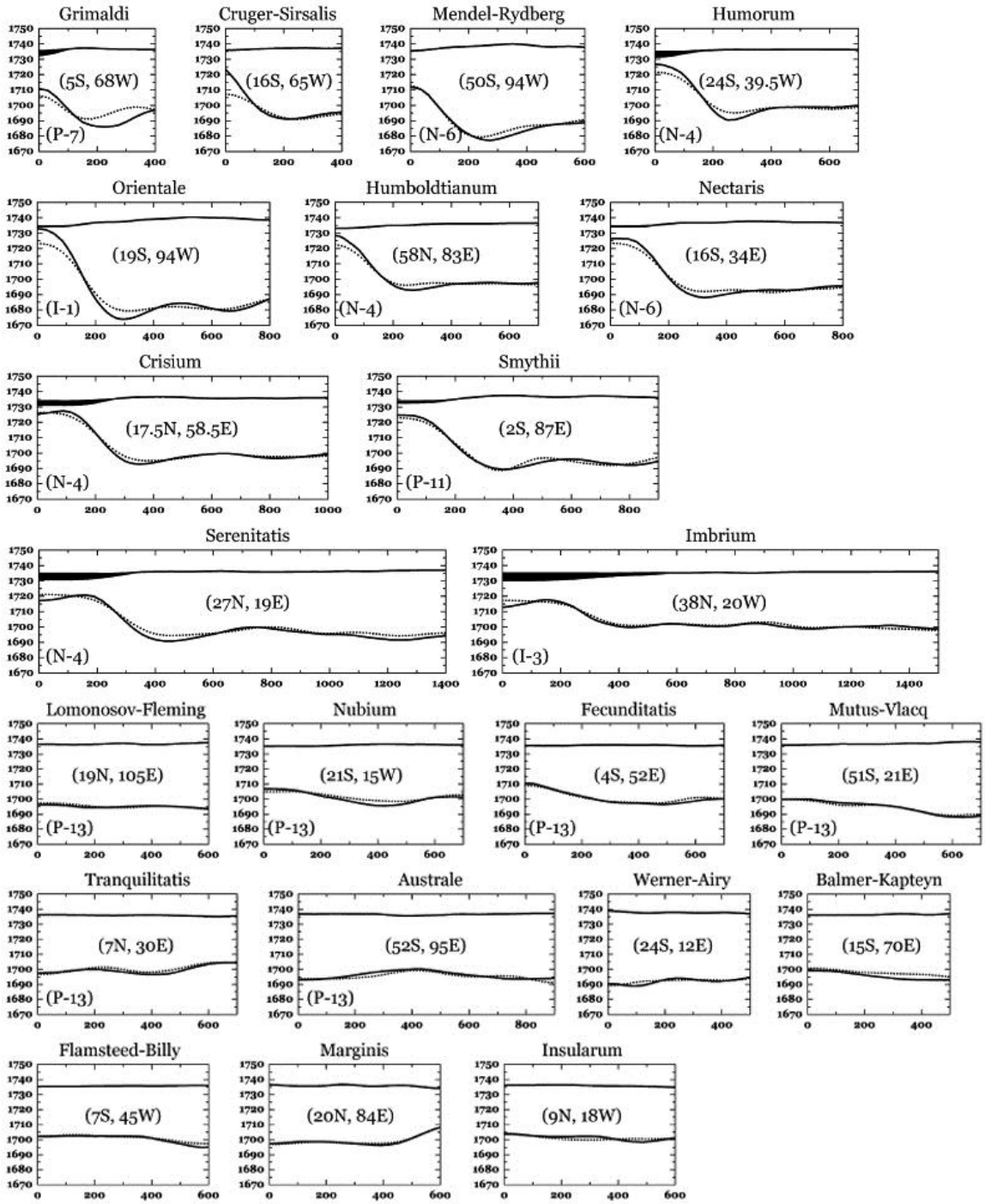

FIGURE 6.29. Crustal profiles for 11 pre-Nectarian, Nectarian, and Imbrian basins (top four rows) and 11 pre-Nectarian basins (bottom three rows) (after Hikida and Wieczorek, 2007). Distance from the Moon's center (y-axis) is plotted against radial distance from the basin center (x-axis). Both axes are in kilometers. Basin center coordinates given in the middle of each image; the letter-number combination in the lower left is basin age from the classification of Wilhelms (1984). In contrast to the older pre-Nectarian basins, the younger basins in the top four rows clearly show topographic variations as well as a thinned crust beneath the basin center, and a thickened crust towards its edge. The older basins in the bottom three rows show generally flat topography and Moho structure and no clear crustal thinning below the basin center or crustal thickening at the basin edges.

Spatial distribution

Jolliff *et al.* (2000) divided the Moon into three separate terranes: the South Pole-Aitken Terrane (SPAT), the Feldspathic Highlands Terrane (FHT) and the Procellarum KREEP Terrane (PKT) (Fig. 6.30). Differences in composition between these terranes could have affected the cratering forming process. To see if terrane composition did affect basin formation (for example, it has been hypothesized that the PKT never possessed an anorthositic crust; Jolliff *et al.*, 2000) it would be advantageous to sample basins of similar age and/or size which impacted into different terranes.

Size distribution and number of rings

Not all of the impact structures classified as basins by Wilhelms (1987) possess three ring structures and are not, therefore, by the definition of Melosh (1989), true multi-ring basins (Fig. 6.31). It is possible those basins ~300 km in diameter with only two discernible rings are multi-ring basins, but due to impact over-printing and degradation, they no longer possess any outer ring features. However, this seems unlikely for the young Imbrian basin Schrödinger, which appears to be a peak-ring crater and not a multi-ring basin. Nevertheless, it is possible that the mechanism responsible for peak ring formation in peak-ring craters is the same for multi-ring basins. By sampling these more accessible (in terms of their size) basins, it would be possible to determine the structure and formation of peak rings. It would therefore be important to visit at least two basins, one smaller, more accessible basin 300 km in diameter and one basin with at least three clearly defined rings of similar ages.

Basin certainty

Added to these three criteria is basin certainty. Wilhelms (1987) classified basins as definite, probable or possible, depending on their features. In terms of determining multi-ring basin structure, basins defined as definite are here given sampling priority over the probable or possible basins. However, it would also be advantageous to visit other basins or study them in greater detail (*i.e.*, remotely) to aid clarification of basin structures.

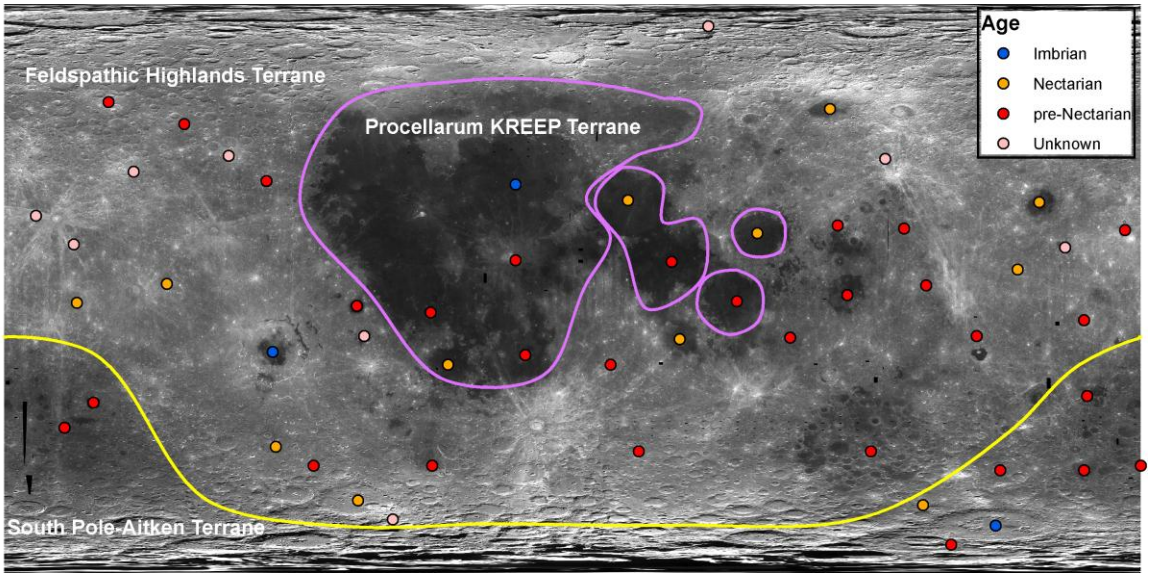

FIGURE 6.30 A global Mercator projection of the Moon showing lunar multi-ring basins classified by age (Wilhelms 1984) (see legend) and terrane. The purple boundary represents the extent of the Procellarum KREEP Terrane, the yellow boundary represents the extent of the South Pole-Aitken Terrane. The rest of the surface area is represented by the Feldspathic Highlands Terrane (terranes from Jolliff *et al.* 2000). Of the 53 basins, 29 are pre-Nectarian (red), 12 are Nectarian 9 (orange), 3 are Imbrian (blue) and 9 are unknown (pink) in age.

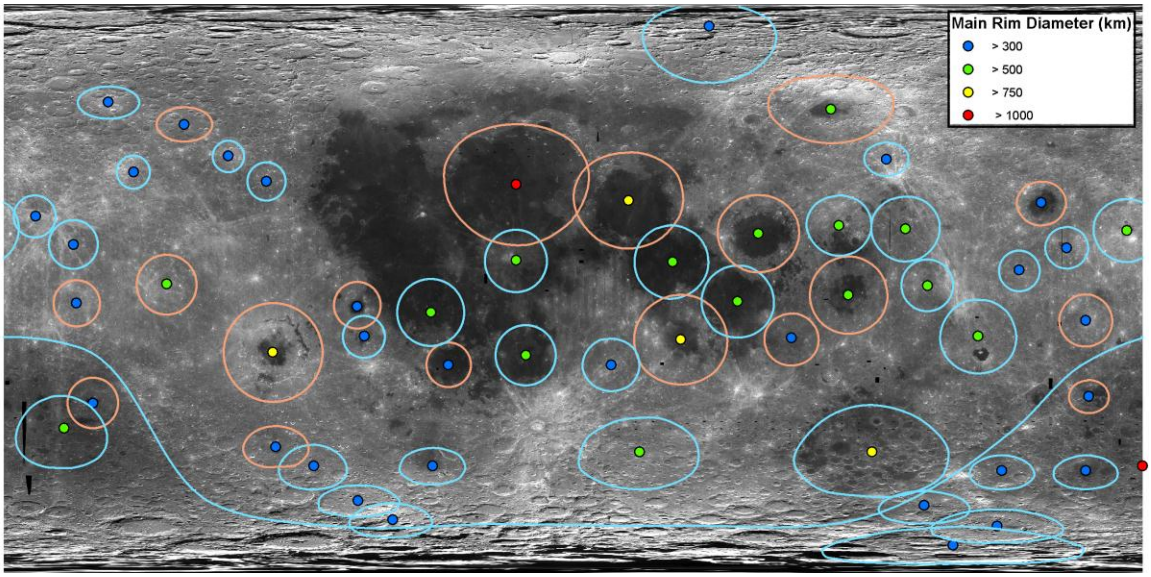

FIGURE 6.31 A global Mercator projection of the Moon showing lunar multi-ring basins classified by main topographic rim diameter (Wilhelms 1987; Pike and Spudis 1987; Spudis 1993; Cook et al (2000, 2002) (see legend). The larger circles represent the extent of each individual basin's topographic rim. Basins containing < 3 identified ring structures have a blue circle (35 basins); basins with ≥ 3 rings have a beige circle (18 basins). 31 basins are >300 km in diameter, 15 >500 km, four >750 km and two >1000 km. Note that away from the equator, basins appear to increase in size and ellipticity. This is an artifact of the projection, and does not represent true basin size relative to one another.

Summary of Site Recommendations

Based on the analysis outlined above, a total of 11 basins have been selected as suitable for determining the structure of multi-ring basins (Table 6.5, Fig. 6.32). Of these basins, Orientale should be given the highest priority for sampling because it is the youngest impact basin, has undergone the least degradation, and possesses three clearly defined ring structures. At Orientale it would be possible, in theory, to sample a peak ring, a main rim, and an outer ring. Smaller, younger impacts in the center of the basin could be used to infer the composition and depth of a (possibly differentiated) melt sheet. Rock sampling would also allow a definitive age of the basin to be calculated, which would help constrain an end date for the Lunar Cataclysm. Many other basins can be investigated to determine how multi-ring basin structure differs within different lunar terranes and with age. However their lack of attributes means a limited number of features can be sampled.

TABLE 6.5. Criteria indentifying the best basins to determine multi-ring basin structure. Certainty: Basins classified by Wilhelms (1987) as certain are checked. Well preserved: Basins of Nectarian or Imbrian age, based on Wilhelms (1984) are checked. Basins which contain clear evidence of at least 3 rings, a peak-ring, or an outer ring are also checked. Basins are listed in order of age (youngest to oldest), and then alphabetically. Eleven basins (bolded in table) match all five criteria and are therefore the chosen priority sites for determining multi-ring basin structure. Outside of these 11 basins there are many others which can be visited to help determine basin structure, but not all criteria and features could be studied.

Basin/Category	Certainty	Well Preserved	3 or more rings	Peak-ring	Outer Ring	Total
Orientale	✓	✓	✓	✓	✓	5
Schrödinger	✓	✓		✓		3
Imbrium	✓	✓	✓	✓	✓	5
Bailly	✓	✓		✓		3
Crisium	✓	✓	✓	✓	✓	5

Hertzsprung	✓	✓	✓	✓	✓	5
Humboldtianum	✓	✓	✓	✓	✓	5
Humorum	✓	✓	✓	✓	✓	5
Serenitatis	✓	✓	✓	✓	✓	5
Sikorsky-Rittenhouse	✓	✓				2
Mendeleev	✓	✓		✓		3
Korolev	✓	✓	✓	✓	✓	5
Mendel-Rydberg	✓	✓	✓	✓	✓	5
Moscoviense	✓	✓	✓	✓	✓	5
Nectaris	✓	✓	✓	✓	✓	5
Apollo	✓		✓	✓	✓	4
Grimaldi	✓		✓	✓	✓	4
Freundlich-Sharonov	✓					1
Amundsen-Ganswindt	✓			✓		2
Birkhoff	✓			✓		2
Planck	✓			✓		2
Schiller-Zucchius	✓			✓		2
Lorentz	✓			✓		2
Coulomb-Sarton	✓		✓		✓	3
Smythii	✓		✓	✓	✓	4
Ingenii	✓		✓	✓	✓	4
Keeler-Heaviside	✓		✓	✓	✓	4
Poincare	✓			✓		2
Australe	✓			✓		2
Fecunditatis					✓	1
Lomonosov-Fleming						
Mutus-Vlacq						
Nubium						
Tranquilitatis					✓	1
Al-Khwarizmi-King				✓		1
Balmer-Kapteyn			✓	✓		2
Flamsteed-Billy				✓		1
Grissom-White						
Insularum					✓	1
Marginis						
Pingre-Hausen						
Tsiolkovsky-Stark						
Werner-Airy						
SPA	✓				✓	2
Bailly-Newton						
Cruger-Sirsalis	✓					1
Dirichlet-Jackson	✓					1
Fitzgerald-Jackson						
Fowler-Charlier						
Kohlschutter-Leonov						
Riemann-Fabry						
Sylvester-Nansen						
Wegner-Winlock						

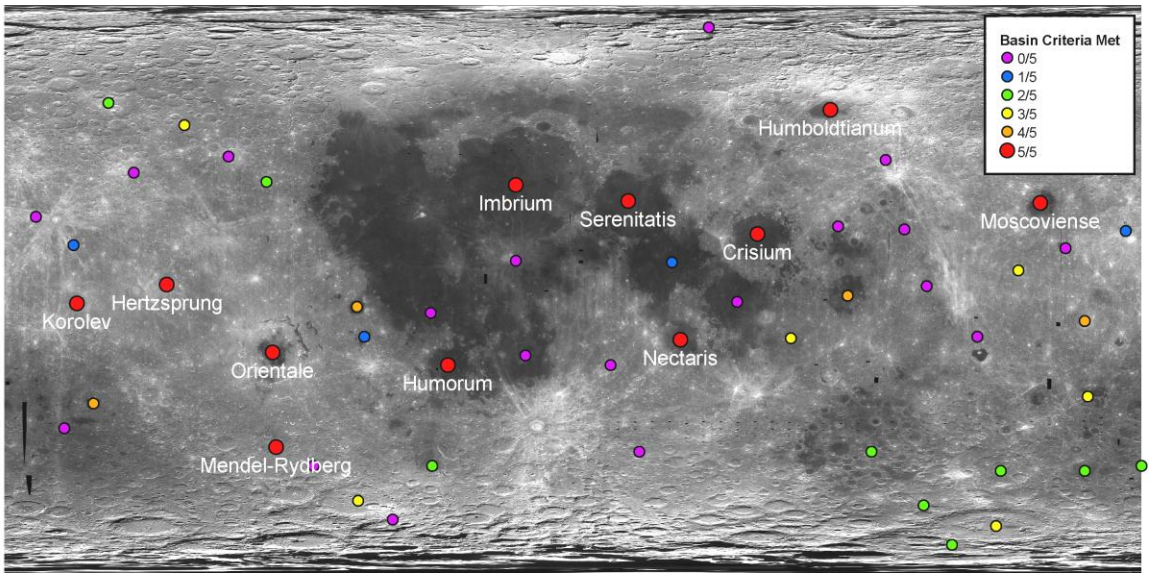

FIGURE 6.32 A global Mercator projection of the Moon showing lunar multi-ring basins. Basins are classified by the number of criteria they meet which are important for determining the structure of multi-ring basins (see text). Basins which meet all criteria are named, with their centers colored red and relatively enlarged. These basins represent the recommended sites for this study. Of these 11 basins, Orientale is the highest priority target due to its young age, well-preserved state, and three clearly defined ring structures.

Case Study of Two Potential Sampling Sites: Outer Rook Ring, within Orientale Basin

We present two possible site sampling localities within Orientale Basin, the highest priority basin for determining the structure of multi-ring basins. Both site localities are positioned on or near the Outer Rook Ring (Fig. 6.33). The Outer Rook Ring lies between the Inner Rook and Montes Cordillera rings. The formation between the two Rook rings is known as the Montes Rook Formation. The Outer Rook ring is an appropriate site to sample as it may possibly represent the main rim or a peak ring of the Orientale Basin. The Montes Rook Formation is also important as spectral data suggests it possesses a weak mafic signature (Head *et al.*, 1993) which possibly represents lower crustal material, inferring the removal of the upper crust during the basin-forming impact. These sites were also chosen due to a break in the Outer Rook Ring at this location; if crew landed here they could visit the massif at either the northern or southern end of the valley (or both).

Site A is located ~350 km south east from Orientale's center, where there is a gap within the Outer Rook Ring at approximately (-22.3^{o}N, -83.2^{o}E) (Fig. 6.34). A crew landing within this valley would be able to sample both, or either of, the northern or southern faces of this Outer Rook massif. At the northern face, large *in situ* boulders as well as possible outcrops for sampling are visible at the summit of the massif. Using Kaguya altimetry data the slope angle on the north slope is ~18^{o}, well within the range of a lunar rover vehicle, allowing the sampling of these summit boulders. In addition to this, boulders which have fallen down the slopes can be sampled at the massif base. On the massif slopes, outcrops containing stratigraphy suitable for sampling may also be present. Crew members would be able to traverse along the base of the ring, collecting samples and looking for stratigraphic sequence sections. The sampling of peak ring material would allow testing of the peak ring formation hypotheses and the structure of the Orientale Basin. For example, if sampling of the ring material infers a deep (lower) crustal origin, this would provide evidence for the Outer Rook forming by the interaction/collision hypothesis, rather than the megaterrace which suggest a shallow (upper) crustal origin for the Outer Rook Ring. A seismic survey could be carried out through the valley to infer the sub-surface structure. A survey across the massif itself may be possible as a lunar rover could easily traverse this. Seismic studies could also be used to test peak-ring formation mechanisms by studying wave velocity and rock density, thereby inferring the stratigraphy of the peak ring.

For example, higher density, originally deep-seated rock overlaying lower density shallow crustal rock, would again provide evidence for the interaction/collision hypothesis of peak-ring formation.

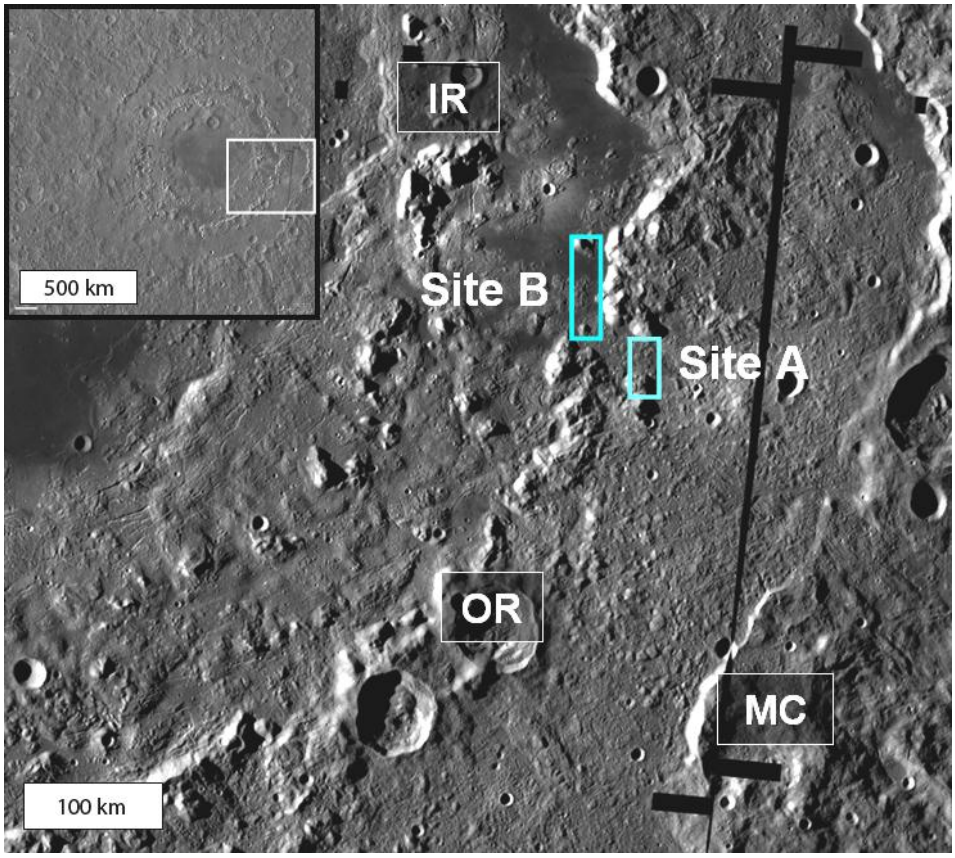

FIGURE 6.33 The locations of two possible sample sites, Site A and Site B, within the Orientale Basin. Site A is located in a break in the ring; from here either the northern or southern section of the ring could be sampled. Site B is located in the Montes Rook formation near some isolated massif structures. An overview of Orientale is presented in the top right for reference and highlights the area within which the sites reside. IR: Inner Rook Ring, OR: Outer Rook Ring, and MC: Montes Cordillera (LROC WAC mosaic of Orientale Basin. Arizona State University).

Site B, ~20 km northwest of Site A could also be a potential sampling site. This locality lies just inside the Outer Rook Ring within the Montes Rook Formation. At this particular locality, a group of what appear to be isolated massifs are present at approximately (-21.14^{o}N, -84.17^{o}E) (Fig. 6.35). These could potentially represent part of the extent of the transient crater or material which has slumped off the Outer Rook Ring. Spectrally, this is also an area of interest as it displays elevated Ti and Fe content relative to the rest of the basin (Fig. 6.36), possibly representing lower crustal material and help to infer the possible depth of excavation. From a locality in this region, the inner slope of the Outer Rook Ring to the east could be potentially sampled in a similar fashion to that outlined at Site A. However, this would limit the data collection opportunities within the isolated massifs at Site B due to the 10 km exploration radius. If however, the exploration radius was 40 km localities at both sites could be sampled (Fig. 6.36) allowing a more thorough examination of the Outer Rook Ring.

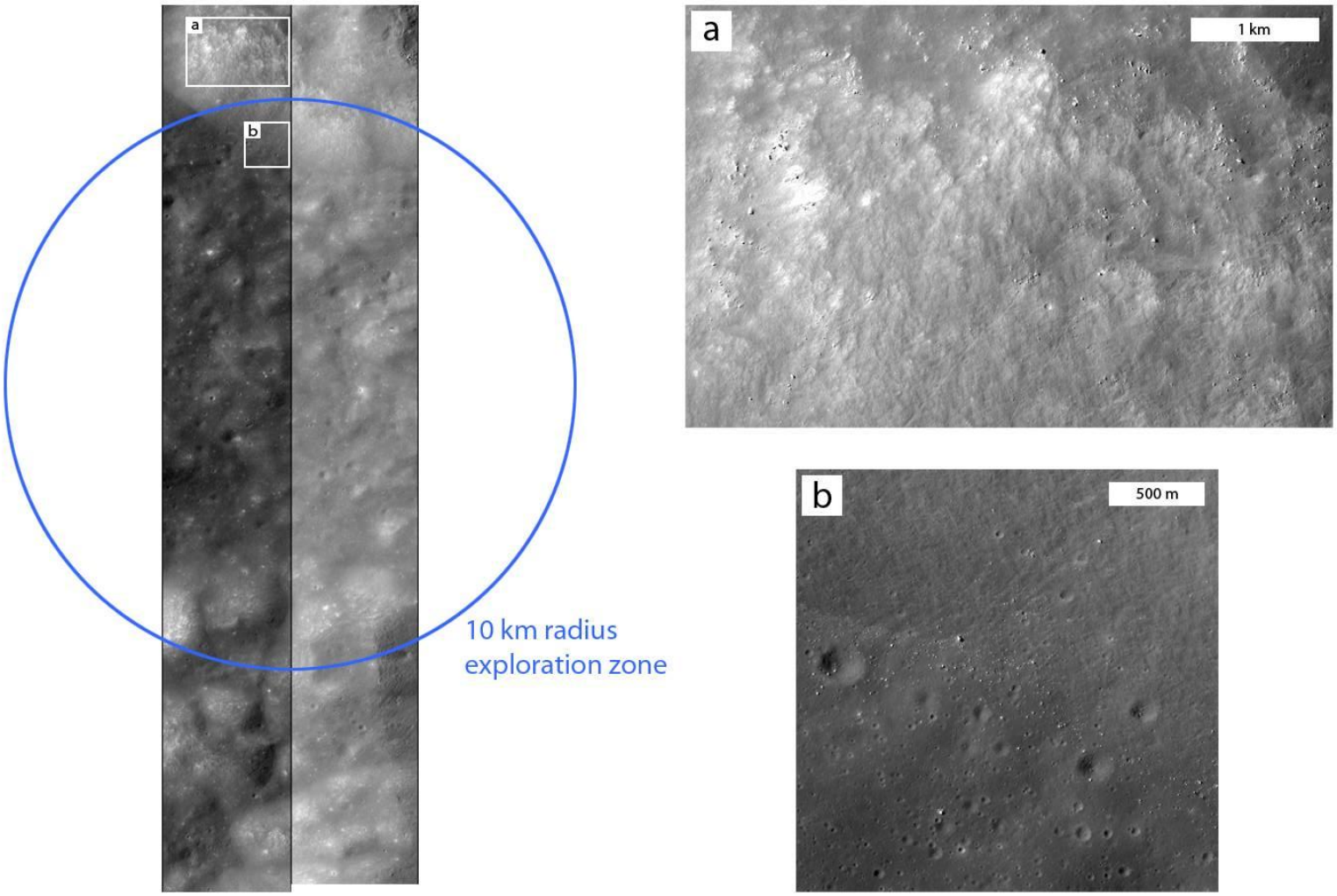

FIGURE 6.34 Example Site A. The two strips on the left are the full extent of LROC NAC images M105063975LE and M105063975RE. The blue circle represents a 10 km exploration radius; it is not placed at any particular location. Two specific localities at this site are highlighted, and scaled up in the images on the right. They highlight zones where samples can be taken from boulders and/or outcrops.

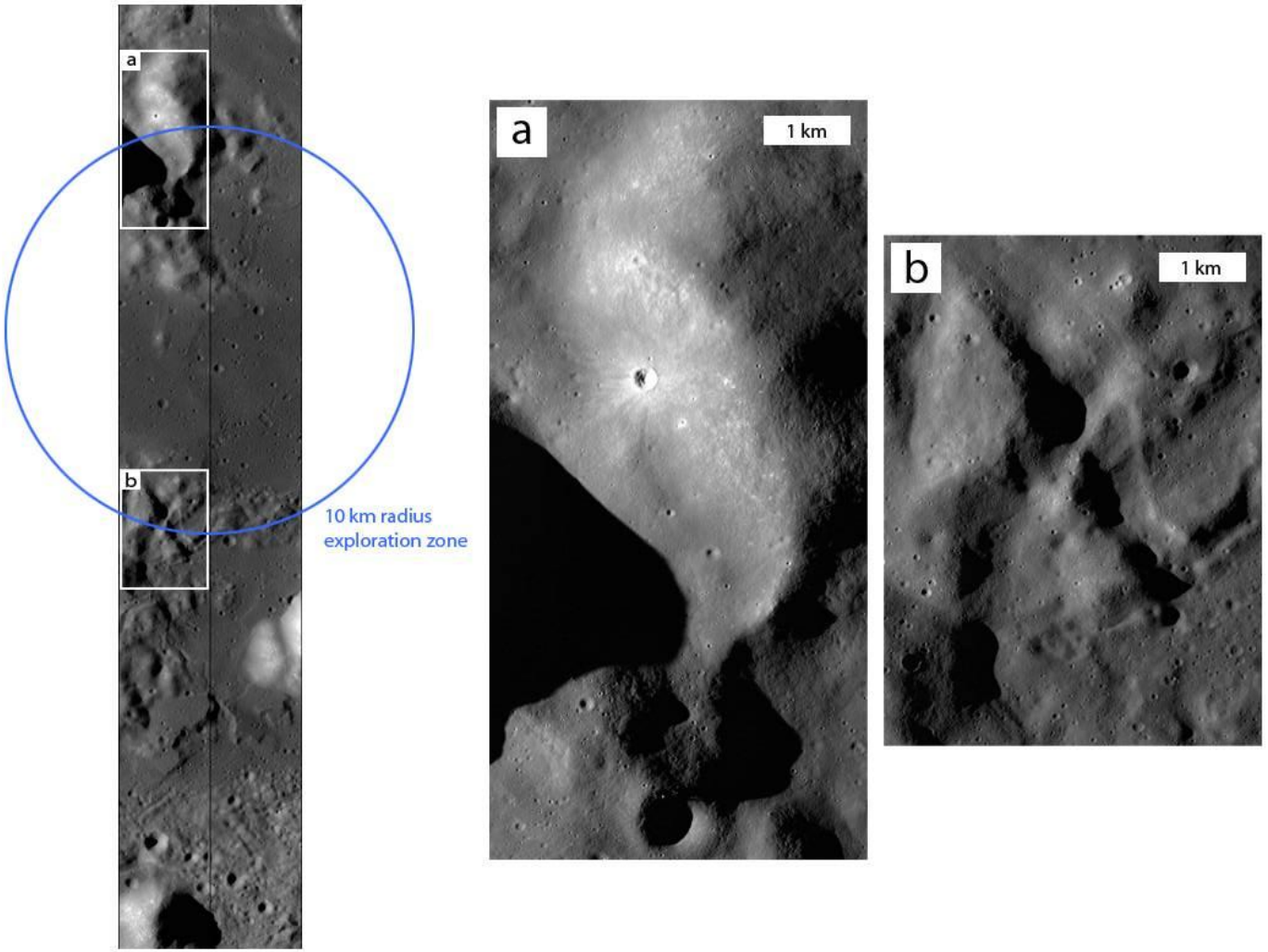

FIGURE 6.35 Example Site B. The two strips on the left are the full extent of LROC NAC images M102709239LE and M102709239RE. The blue circle represents a 10 km exploration radius; it is not placed at any particular location. Two specific localities at this site are highlighted and scaled up in the images on the right. They highlight zones where samples can be taken from the faces of massifs or from freshly exposed material.

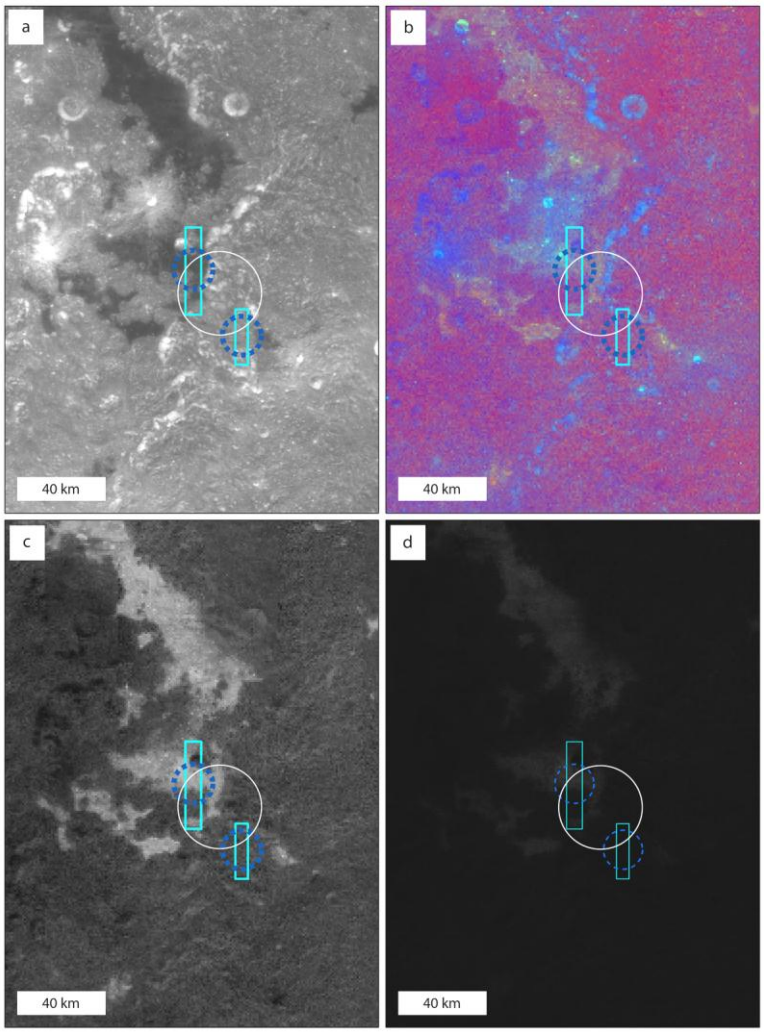

FIGURE 6.36 (a) UVVIS, (b) rgb false color, (c) FeO, and (d) TiO Clementine images highlighting the example sites (shown by the turquoise rectangles of the LROC images). The dashed blue circles represent a 10 km exploration radius, while the white circles represent a 40 km exploration radius. Given the larger exploration radius, both sites could be visited in a single mission. Site A (lower turquoise rectangle) would allow sampling of the Outer Rook Ring; Site B would allow sampling of isolated massifs and areas of elevated Fe and Ti (lighter colors) within the Montes Rook Formation.

Limitations

These two example sites show the limited amount of data and multi-ring basin features that can be collected from a single mission constrained by a 10 km exploration radius. With this travel constraint it would be impossible to visit both these example sites in a single mission; both sites could be visited if the exploration radius was increased to 40 km. This highlights the importance of selecting potential sample sites within a multi-ring basin, especially if other goals and objectives also need to be achieved. Therefore significant pre-mission planning must be undertaken to highlight potential sampling sites. Factors such as geochemical content, slope angle, basin attributes, and lunar location (*e.g.* sunlight, direct communication with Earth) must be carefully considered when planning a sample return mission to a multi-ring basin.

Conclusions

Eleven basins have been identified as potential sites to determine the structure of multi-ring basins. Of these basins, Orientale is the highest priority due to its relatively young age, preservation, and number of

clearly defined rings. Various hypotheses regarding the formation of multi-ring basins can be tested at a variety of locations within a basin. However, only one particular feature, for example a peak ring, could be studied in a single mission given a 10 km radius of exploration. Two rings could be studied and sampled at Orientale (the Inner and Outer Rook Rings) in one mission given a far larger exploration radius of 35 km. For other basins, an even larger exploration radius would be required to sample two ring structures (see Tables A4 and A5 in Appendix A). Geological sampling of outcrops or boulders would be the primary method of data collection. Seismic surveying would be useful, however given the size of massifs and the limits of crew exploration a definitive seismic study over a multi-ring basin feature is unlikely.

The full extent of a multi-ring basin structure could not be examined in a single mission, given current architectural limits. Nevertheless, at a well-chosen site locality, vital field data could be collected, allowing the testing and re-evaluation of multi-ring basin formation hypotheses and scaling laws.

SCIENCE GOAL 6C: QUANTIFY THE EFFECTS OF PLANETARY CHARACTERISTICS (COMPOSITION, DENSITY, IMPACT VELOCITIES) ON CRATER FORMATION AND MORPHOLOGY

Introduction

Impact structures are ubiquitous on solid surfaces of planets, satellites, and small bodies throughout the Solar System. Crater morphologies vary dramatically between these bodies as a result of the unique physical and chemical characteristics of the targets. The lunar surface is scarred by more 300,000 craters greater than 1 km in diameter, representing more than 4 billion years of impact history. The Moon is drastically different from the Earth, with one-sixth the gravity, virtually no water, and a different crustal composition. Impact structures on the Moon can be compared with terrestrial craters to infer the importance of various target parameters. The following section provides guidelines for resolving many issues regarding impact cratering that are still under debate by suggesting landing sites and implementation methods needed to gather the appropriate data.

Scientific Background

Many contentious issues exist within the field of impact cratering. In part these conflicts arise from the variety of methods used to study impact cratering: laboratory experiments, TNT and nuclear explosions, numerical simulations, and geological field work at terrestrial impact structures. Field geology can provide constraints for the other methods, however the number of well preserved impact structures on Earth is limited, affecting our ability to accurately replicate the effects of impact cratering on planetary scales. The plethora of scaling laws, models, and theories that these methods have produced must be used with caution until more ground truth is gathered. We present here a summary of impact cratering theories and models that could be tested on the Moon.

Simple craters

On the Moon, simple craters range from micrometers to ~20 km in diameter. At ~kilometer scales a lens of debris fills their interior, composed of impact breccia that has slid off the crater walls and rim, decreasing apparent crater depths and slightly increasing diameters. The maximum thickness of this layer is roughly half the rim to floor depth and its volume, on average, is half that of the final crater (Melosh, 1989). In terrestrial craters, the density of this layer is approximately 5% less than the country rock. Gravity deficiencies associated with lunar craters and the investigation of one small crater by Apollo 17 crew suggests the same density differences and breccia lens volumes (Dvorak, 1979). Equation 6.4 relates the volume of breccia and the apparent crater diameter to the transient crater:

$$D_t = D(1 - 1.2H_b/[H + H_b]) , \qquad (6.4)$$

where D_t and D are the transient crater diameter and apparent crater diameter, respectively, and H_b and H are the maximum height of the breccia lens and the apparent height of the crater, respectively (units are in meters) (Melosh, 1989). To test this model, breccia lens volumes could be measured for lunar craters on various target lithologies.

There are some anomalous morphologies among simple craters. Bench craters are small, simple craters with either a flattened floor or a small mound at their center. These are caused by impacts into mixed

targets of poorly consolidated regolith overlying intact crust (Oberbeck and Quaide, 1968). The apparent depth of these bench craters has been used to correctly predict the depth of the lunar regolith at the Apollo landing sites. Bench craters have also been identified on Mars and Mercury (Melosh, 1989). Concentric craters display a prominent inner ring and have reduced depth-diameter ratios. They may also be the result of impacts into layered targets. Their occurrence mostly on the margins of maria suggests an origin related to volcanism (Schultz, 1976; Wood, 1978; Wohler *et al.*, 2009). Visiting these anomalous crater types could reveal how target properties influenced their morphology.

Secondary impact craters

Secondary craters are formed from ejected material of a primary impact. They typically have steeper wall slopes angled toward their primary crater, are less circular, and have asymmetric ejecta distribution patterns due to lower impact speeds. They often form crater chains and typically have poorly defined crater rims. Chevron-shaped dunes appear between secondary craters, possibly as a result of simultaneously expanding ejecta curtains. Secondary craters begin to appear just beyond the continuous ejecta blanket, and if far enough away from the parent crater can appear identical to primary craters (Wilhelms, 1987).

Secondary craters represent a unique opportunity to study impact cratering, since their impact speed and trajectory are known. The effect of projectile mass and speed on final crater morphology can therefore be investigated. The population of secondary craters on the Moon must be known in order to estimate the impact flux, so greater knowledge of secondary crater morphology is needed to distinguish them from primary craters (NRC, 2007).

Ejecta deposits

Material ejected from a crater during the excavation stage mixes with the target material in a process called ballistic sedimentation (Oberbeck, 1975). Depending on its proximity to the crater, ejecta will either become part of the continuous or discontinuous ejecta blanket, or be deposited as high-albedo, radially-distributed rays. The brightness of crater rays, in part, is attributed the material's immaturity; freshly produced surfaces are brighter due to less exposure to space weathering, which darkens material. Rays are therefore relatively young features. Craters possessing rays are considered Copernican in age. It is uncertain whether these rays are produced from direct deposition of primary ejecta or the ejecta of secondary craters (Hawke *et al.*, 2004). Collecting samples of crater rays could help resolve this issue.

Central peak formation

Central peaks are the most prominent feature of complex craters, ranging from 10 m to 3.5 km in height. Tsiolkovsky Crater, 185 km in diameter, has a central peak over 30 km across (Hale and Grieve, 1982). Central peaks form when the transient crater floor uplifts material from great depths (Fig. 3.11) (Baldwin, 1972, 1981; Grieve, 1987; Melosh, 1989; Melosh and Ivanov, 1999). In terrestrial craters, this theory has been supported by relating the stratigraphic position of central peak material to stratigraphy outside the crater, showing that central peak material comes from below the depth of the transient crater (Grieve, 1987). A fundamental check must be performed to determine if lunar central peaks are also the product of uplift or if they are formed in an alternative process, such as the accumulation of collapsing rim material (Wilhelms, 1987).

Stratigraphic uplift

In order to predict the lithologies of central peak material, Cintala and Grieve (1998) developed a scaling law for stratigraphic uplift, *SU*, in lunar central peaks:

$$SU = 0.022D^{1.45}, \qquad (6.5)$$

where *D* is crater diameter (units in meters). Observations of lunar central peak heights indicate that craters above 50 km in diameter do not follow Equation 6.5, possibly due to the transition between central-peak and peak-ring craters. Hale and Grieve (1982) observed that central peak volume is reduced for craters above 80 km in diameter and hummocky terrains start to encircle the central peak. Above 140 km, this material eventually becomes a peak ring. It is likely that the amount of stratigraphic uplift for larger complex craters is proportionally lower due to the collapse of the central peak into a peak ring. Uplift for craters outside the range of this scaling law should be tested to understand how uplift varies as a function of

diameter. The model itself should also be tested, as well as the assumption that melting depth and stratigraphic uplift are directly equivalent.

Target properties and transition diameter

The influence of target properties on uplift can be determined by observing the transition diameter above which craters develop central peaks. Complex craters develop over a range of diameters depending on the target gravity and composition. Pike (1988) attempted to determine the transition diameter from simple to complex morphologies on several planetary bodies, finding the transition to occur at diameters of approximately 16 km, 10 km, 6 km, and 3 km on the Moon, Mercury, Mars and the Earth, respectively. The data strongly suggest an inverse relationship between gravity and transition diameter (Fig. 6.37A). This demonstrates the importance of gravity in enabling uplift, and suggests the possibility that it also controls the extent of uplift.

Cintala *et al.* (1977) analyzed the effect of target composition on lunar crater morphology and found craters on mare developed central peaks and terraces at smaller diameters than craters on highlands. Their interpretation was the more coherent structure of the mare made it more prone to central peak and terrace formation (Fig. 6.37B), suggesting that the density of the target may be the cause of this phenomenon (the average density of lunar basalt and lunar highlands is 3.25 kg/m^3 and 2.95 kg/m^3, respectively). Complex craters within the South Pole-Aitken Basin (which may have been excavated in lower crustal material; Wieczorek and Phillips, 1999), on mare, and on highlands should therefore be comparatively sampled in order to investigate if and how target composition effects crater morphology.

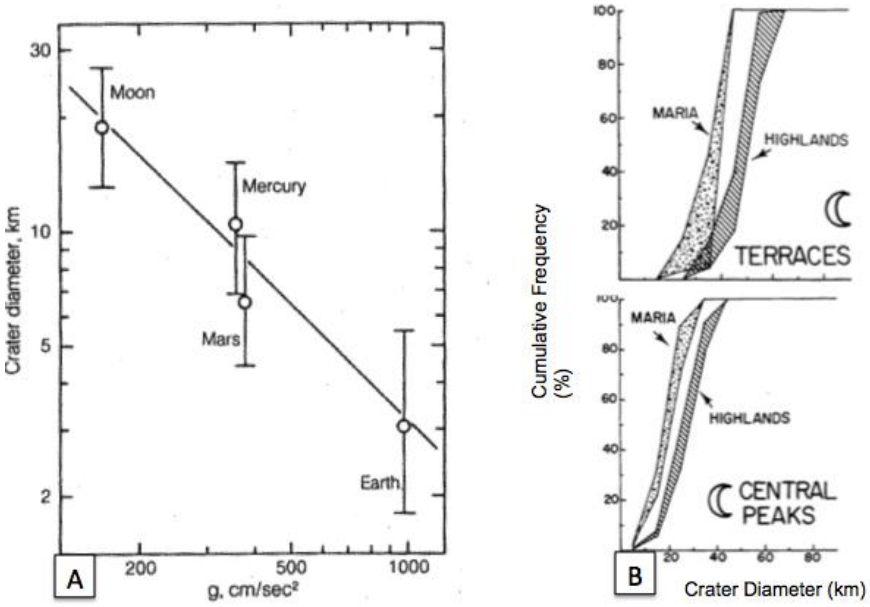

FIGURE 6.37 (A) Crater diameter plotted against target gravity using logarithmic scaling. Circles represent average transition diameter on a given terrestrial body. Error bars are the result of various compositional terranes on the target that also affect transition diameter (from Pike, 1988). (B) Crater diameter plotted against the cumulative frequency of terraces and central peaks. Dotted and dashed areas represent craters that impacted Maria and Highlands, respectively (from Cintala *et al.*, 1977).

Numerical models have also attempted to determine the influence of target properties on crater morphology. O'Keefe and Ahrens (1999) simulated impacts into targets of varying density and gravity, showed that a dimensionless number Ω could be used to predict the certain morphologies of craters:

$$\Omega = Y_s / \rho g d_p, \qquad (6.6)$$

where Y_s and ρ are the yield strength and density of the target, g is gravity, and d_p is depth of crater penetration (MKS units). Simple craters were produced when $\Omega > 0.15$, while central peak and peak ring

morphologies where produced when $\Omega < 0.15$. This shows that increasing crater size, gravity, or the target density encourages the formation of craters with complex morphologies, consistent with observations. Exploring this relationship on the Moon would require visiting craters that impacted targets of varying density and strength.

Terrace formation

On formation of the transient crater, the crater walls become unstable and collapse inwards toward the crater center. In small craters this collapse results in scallops, localized mass wasting deposits evenly sloped at the angle of repose. Above diameters of 20 km, terraces, large discrete blocks often several kilometers wide that encircle the crater interior, form. They slide along faults whose slopes flatten out as they approach the center of the crater (Melosh, 1989). They are affected by composition and gravity in a similar manner as central peaks, developing more readily in mare and at lower diameters in higher gravity (Cintala *et al.*, 1977; Pike, 1988).

Within a complex crater, a single impact melt flow often lies over multiple terraces, suggesting that terraces are emplaced directly after the transient crater forms, before impact melt solidifies. Terraces increase in width closer to the crater center, a behavior consistent with models that require collapsing material to behave plastically (Pearce and Melosh, 1986). The transient crater can be reconstructed by tracing terrace movement back along fault lines. Scaling laws relating the diameter of the final crater to that of the transient crater have been developed using this method (Croft, 1985). Understanding the extent of terrace movement and whether terrace formation occurs in brittle or ductile regimes could be investigated from the floor of a complex crater.

The physical mechanism enabling crater collapse

The influence of target properties on crater morphology is clear. However the exact roles of gravity and target composition in the cratering process, especially during the modification phase, is somewhat unclear because the physical mechanism that allows the transient crater to collapse is still under debate (Ivanov and Melosh, 1999). One possibility is that transient craters above a certain size exceed a strength threshold resulting in the uplift of the crater floor and the subsequent formation of central peaks and terraces. However, for small complex craters, the calculated force of this instability seems to be too weak to overcome the strength of typical rocks (Melosh, 1983), which would prevent the crater from uplifting. This suggests there must be some additional mechanism associated with the cratering process that substantially lowers or removes the strength of the target material and allows material to flow. Acoustic fluidization has been proposed as a mechanism. It is unlikely that acoustic fluidization could be directly tested, but perhaps clast size distribution and maximum pressure and temperature exposures in central peak material could constrain its feasibility.

Melt production

For impacts of equivalent kinetic energy, resulting craters on Earth will be smaller than those on the Moon (due to the larger surface gravity), although similar volumes of impact melt should produced, resulting in a higher ratio of melt to crater volume in terrestrial impacts. When comparing lunar and terrestrial melt volumes it is difficult to discern what factors are most influential in changing melt volume ratios. Comparing lunar craters with each other may help disentangle the relative importance of impact speed and target composition in determining melt ratios.

Implementation

A wide variety of features and processes can be studied to expand our understanding of impact cratering, but some features can only be studied at certain locations. The large spatial scale and geographic extent of even moderately-sized craters is often under-appreciated and if one lands in the interior of a complex crater it is unlikely that a rover would be able to navigate out. Crater walls are generally sloped at the angle of repose (~30^o), while current rover capabilities can comfortable handle slopes of only 25^o (Lunar Exploration Science Working Group, 1995). It is therefore important to note what can be accomplished from landing within a crater as opposed to landing on the crater rim. Table 6.6 lists the most pertinent questions of impact cratering and where each of them can be answered. Visiting multiple craters would enhance the understanding of every aspect of impact cratering, but to answer some questions, visiting multiple craters is the minimum requirement.

TABLE 6.6 Check marks denote where the most pertinent questions regarding the impact cratering process can be addressed.

	Crater Rim	Crater Interior	Multiple Craters
How do lunar central peaks form?		✔	
What is the stratigraphic uplift in central peaks?		✔	
How is this uplift affected by target composition and gravity?		✔	✔
What is the depth of melting in craters?	✔		
Is it equal to the original depth of central peak material?		✔	✔
What is the volume of impact melt?		✔	
How is melt volume affected by target composition and gravity?		✔	✔
How does impact velocity affect crater morphology?	✔	✔	
What is the excavation depth in lunar craters?	✔		
How is it affected by target composition?	✔		✔

The crater interior

The crater interior is the best vantage point for studying crater morphology. Seismometers may be placed on the crater floor and used to infer subsurface structure (*i.e.*, density changes) and therefore estimate impact melt sheet volume as well as the structure of the central peak or peak ring. Once samples are obtained, the seismic wave speed in that material can be measured, allowing for interpretation of the seismic data. This method has been used to measure these parameters at the Chicxulub Crater (Morgan *et al.*, 2000) (Fig. 6.38). A more accurate measurement of impact melt volume could be acquired with a gravity survey, allowing scaling laws that predict melt volumes to be tested (Cintala and Grieve, 1998; Lucey *et al.*, 1998; Petro and Pieters 2002).

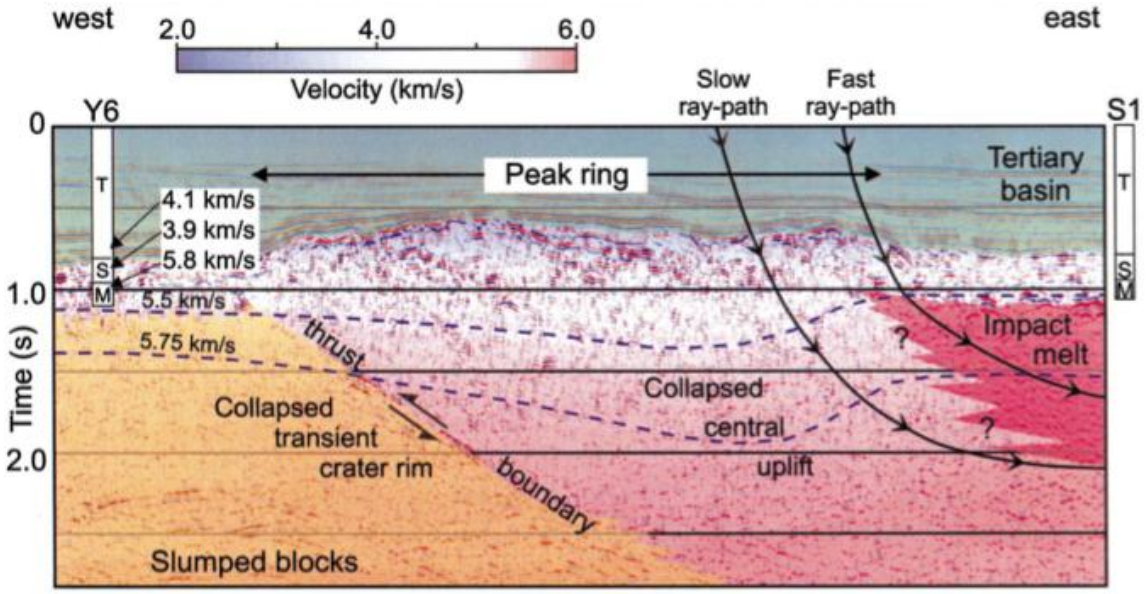

FIGURE 6.38 Seismic reflection data from the Chicxulub impact crater. Faster wave speeds toward the crater's center are interpreted to be caused by a large volume of impact generated melt rock. A linear discontinuity below the peak-ring in interpreted to be a thrust fault that uplifted material form depth (after Morgan *et al.*, 2000).

Examination of the crater wall can give insight into terrace formation. The motion of terraces can be restored by identifying similar stratigraphic units within the modification zone. Materials such as pseudotachylite along the terrace fault surfaces could give insight to the timing of fault movement and the pressure and temperature conditions during which the fault was active. Central peak and peak rings can be examined to determine if both features are the product of uplift. Samples of both should be taken and returned to Earth so their pre-impact positions in the crust can be estimated. Thin veneers of melt can often cover the central peak, so it is important that samples of actual central peak material are collected (Melosh, 1989). The degree of shock metamorphism in a target rock can be related to its pre-impact depth. Determining the composition of uplifted material and comparing it with the predicted composition from crustal thickness estimates can test uplift scaling laws.

The composition of impact melt may help reveal the depth of melting. If deeply buried lithologies such as lower noritic crust or lunar mantle, are included in the melt zone, their chemical components should be visible in the overall melt composition. Samples of impact melt should be taken from the excavated material of subsequent craters that impacted the larger crater's melt sheet. If multiple craters on various lithologies are visited, the effect of target composition and impact velocity on melt volume can be assessed.

The crater rim

Some impact features can be investigated exterior to the crater rim. Melt appears in ejecta as tektites, small glass spherules, or as the matrix of an impact breccia. Recovery of these components could yield the composition of the impactor and possibly the depth of melting. The excavation depth can be estimated if the composition of ejected materials can be related to target lithologies.

High-resolution views of the crater interior from the rim could aid in post-mission photo-geology. This could lead to enhanced interpretations of terrace formation and transient crater modification. The range of impact lithologies can also be studied from this vantage point.

Recommendations

To investigate the questions outlined in the previous section several prioritized requirements must be met:

- Land in or near a well preserved complex crater
- Visit craters that have impacted different lithologies
- Explore several simple craters
- Examine craters of anomalous morphologies
- Examine a secondary crater

The most compelling questions can be addressed by visiting complex craters; these locations should therefore receive priority. Simple craters exist everywhere on the lunar surface and within a 10 km radius of any landing site there should exist several fresh simple craters for study. However, to address the importance of target composition, several craters in different terranes should be visited. Anomalous crater types and secondary craters are given a lower priority as their investigation will not address as many aspects of the impact process as other sites (*e.g.*, complex craters).

Central peak craters of Copernican and Eratosthenian age were selected since they are relatively unmodified and their numbers and spatial distribution provide a wide range of landing sites. Craters were selected from the Lunar Impact Crater Database (Losiak *et al.*, 2011) and cross referenced with an independent study of the young rayed lunar crater population (Werner *et al.*, 2010). Because there are no peak ring craters of Copernican or Eratosthenian age, peak ring craters of every age were included, apart from extremely degraded examples. This produced 234 candidate landing sites. Lunar Orbiter, Apollo, and Clementine images were analyzed to assess the degradation state of each crater, producing a list of 164 craters that were preserved well enough to be ideal for studying crater morphology (Table A6.1). The craters are classified by morphology into simple-complex transitional, central-peak, central-peak-to-peak-ring transitional, and peak-ring craters. Target lithology is also identified for all craters.

The craters are classified by morphology into central peak craters, peak ring craters, transitional craters between simple and complex and transitional craters between central peak and peak ring. Target lithology is also identified for all craters. Figure 6.39 shows complex craters that may be appropriate landing sites for studying the impact cratering process. For these craters, assessing the influence of target composition is more difficult, though every other question pertaining to impact cratering can still be investigated.

Figure 6.40 shows a global map of complex craters with crater morphology indicated by color. Yellow circles are craters are between simple to complex morphology. They show flattened floors, poorly defined terraces and no central peak. These craters could be examined to understand target properties' influence on transition diameter. Orange, tan and brown circles represent central peak, transitional and peak ring craters, respectively. There are only 6 peak ring craters that are relatively well preserved. There are 7 craters transitioning from central peak to peak ring.

Figure 6.41 shows the same craters as Figure 6.40 but with color indicating age. Yellow, green, blue, orange and red are Copernican, Eratosthenian, Imbrian, Nectarian and pre-Nectarian craters, respectively. Black circles are craters with no assigned date. White circles show craters of particular interest. Two craters with certain notable features, were selected for each impact terrain: Finsen, Antoniadi, Reiner, Maunder, Aristarchus, Copernicus, Tsiolkovskiy, and Tycho. Finsen crater is the best preserved central peak crater in SPA terrane, while Antoniadi is probably the best preserved peak ring crater on the entire Moon. Reiner and Maunder have the best preserved central peaks of craters that impacted mare, (or impact melt) without excavating all the way through it. Aristarchus and Copernicus impacted mixed lithologies, are especially well preserved craters and have been well studied. Tycho crater is extremely young, 100Ma, and has been a considered as a landing site since the Apollo Era. Tsiolkovskiy is an anomalously large central peak crater that may have uplifted mantle material (Pieters and Tompkins, 1999). These craters are highlighted not to give them highest priority, but to illustrate the kinds of features that are desirable for studying impact cratering.

Craters that may contain mantle or lower crust in the central peak or peak ring are ideal for studying stratigraphic uplift. Figure 6.42 shows craters may have uplifted these deeper lithologies, based on scaling laws by Cintala and Grieve (1998) and crustal thickness estimates by Weiczorek (1999). There are some craters in this list that are not included as candidate sites in previous figures. This is because they are older and more degraded, making them poor location choices for studying crater morphology. However they are still intact enough to recover samples of uplifted lithologies and test models of uplift.

Figure 6.43 shows fresh complex craters and concentric craters overlapped with locations where secondary craters are likely to be densely concentrated. Purple regions indicate the crater interior and the continuous ejecta blanket, calculated by Moore *et al.* (1974), while red regions extend to 4 crater radii away from the crater center. Secondary crater density should be highest just outside the continuous ejecta blanket (Wilhelms, 1987). Only craters of Imbrian age and younger are selected for this figure to ensure satellite craters are not buried by considerable amounts of regolith. Craters that overlap with red regions may be ideal locations to examine secondary crater morphology.

Visiting any of these complex craters could help answer fundamental questions regarding impact cratering and the effect of planetary characteristics on crater morphology. Multiple craters should be examined to refine our conception of impact cratering, and to ascertain target compositions affect on crater morphology.

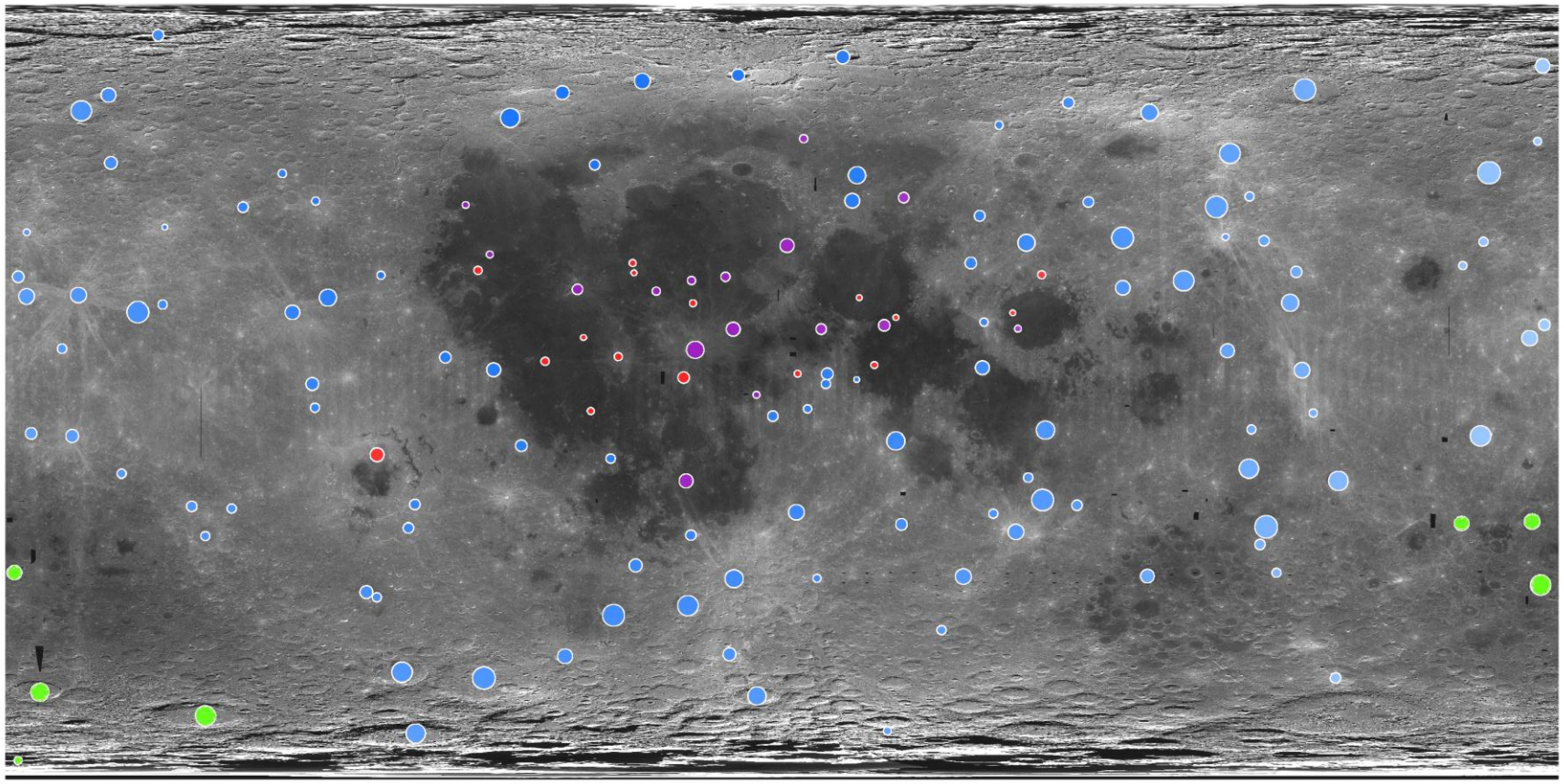

Figure 6.39 Central peak craters of Eratosthenian and Copernican age central peak craters and well preserved peak ring craters. Red, Green and Blue circles represent complex craters that have impacted maria, anorthositic Hhighlands and South Pole-Aitken terranes, respectively. Purple circles show complex craters that have excavated maria and highland material

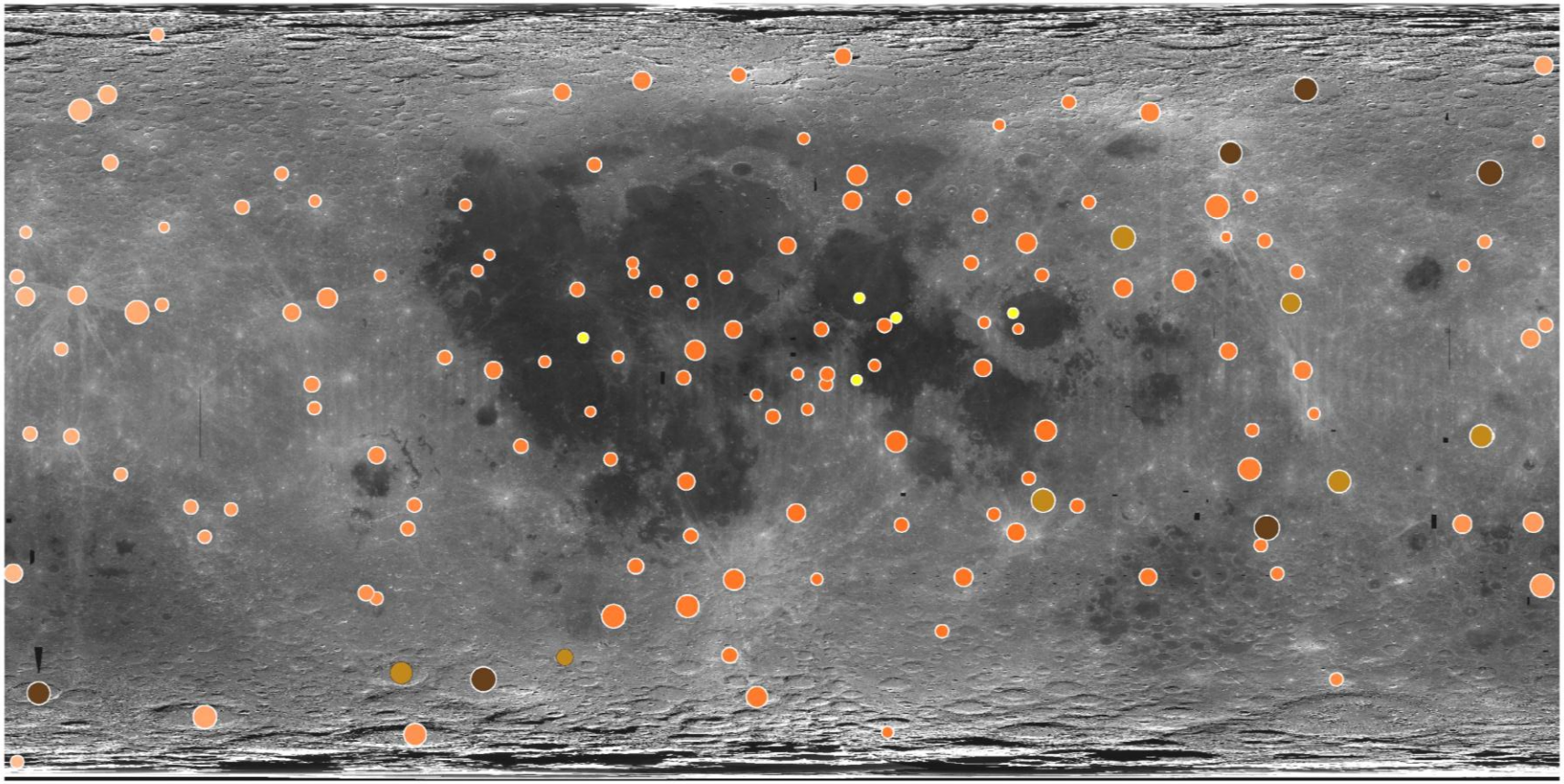

Figure 6.40 All well preserved lunar complex craters. Colors indicate morphology. Yellow cirlces represent small complex craters with flattened floors. Orange, tan and dark brown indicate, central peak craters, craters transitioning from central peak to peak ring, and peak ring craters, respectively.

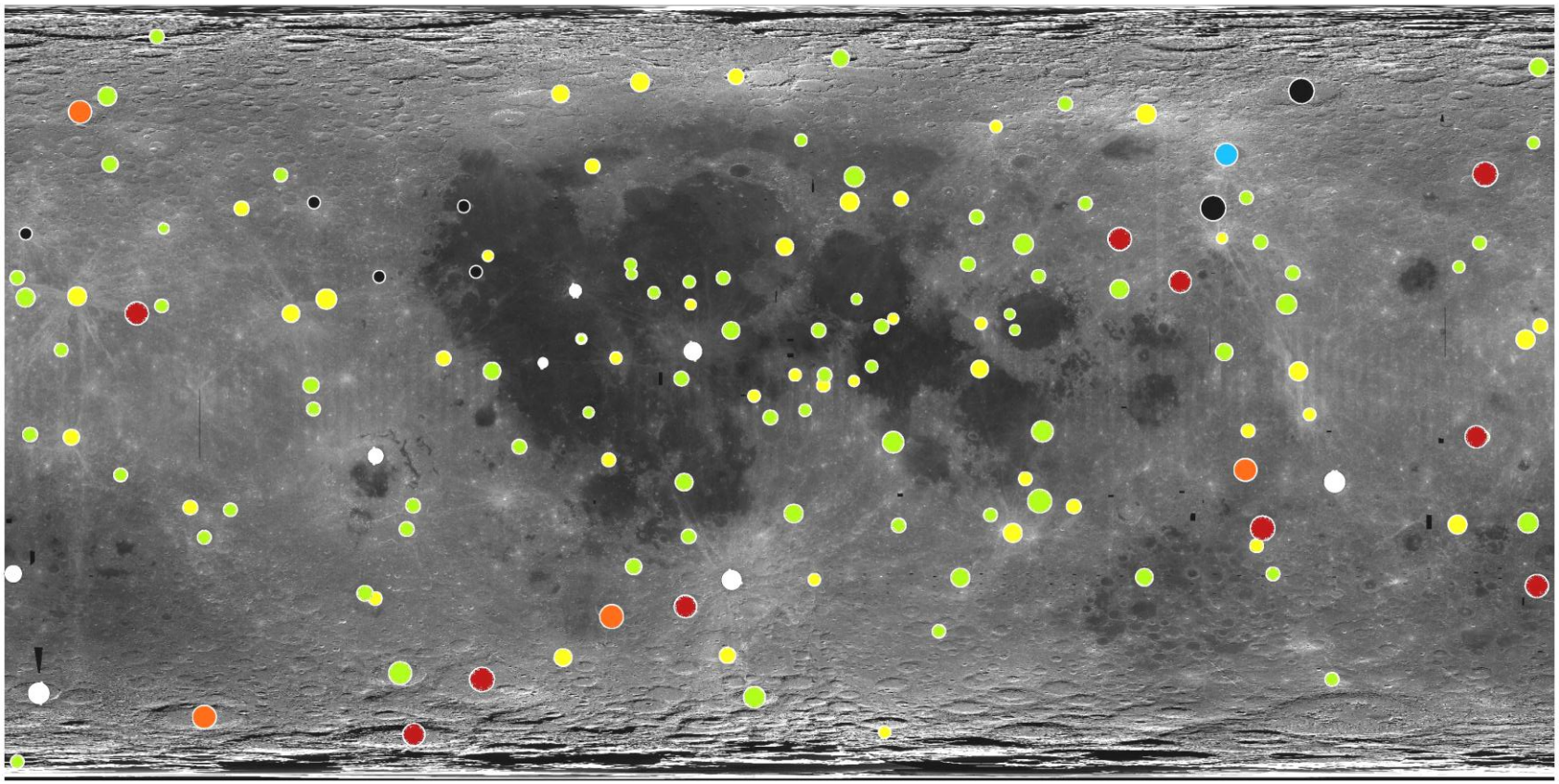

Figure 6.41 All selected craters with colors indicating age. Yellow, green, blue, orange and red are Copernican, Eratosthenian, Imbrian, Nectarian and Prenectarian Craters, Respectively. Black circles represent undated craters while white circles represent select craters of special interest

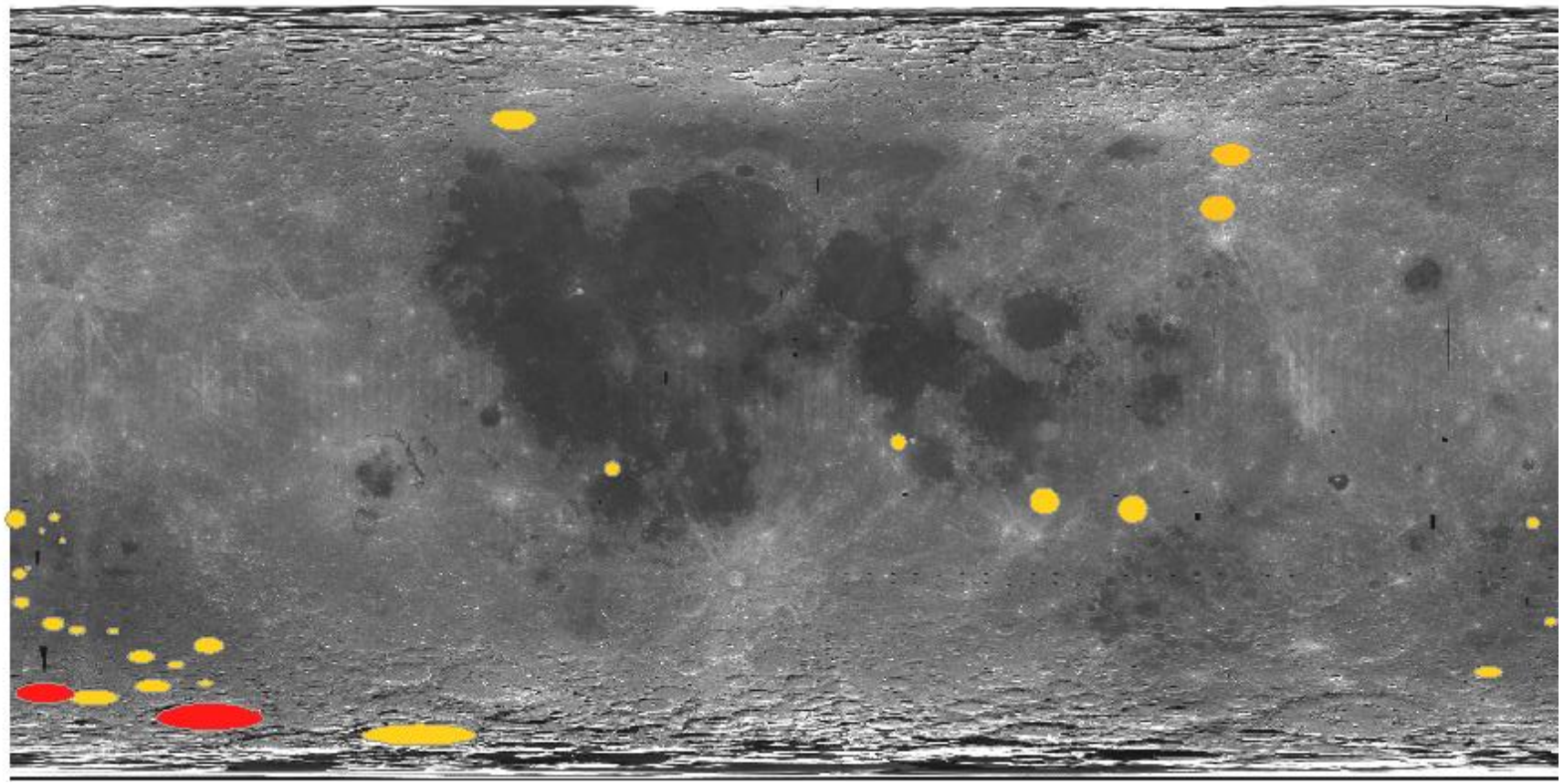

Figure 6.42 Global map showing craters that should contain mantle and or lower crust in their central peak or peak ring. Crater predicted to uplited mantel are red while craters that should only uplift lower curst are in orange

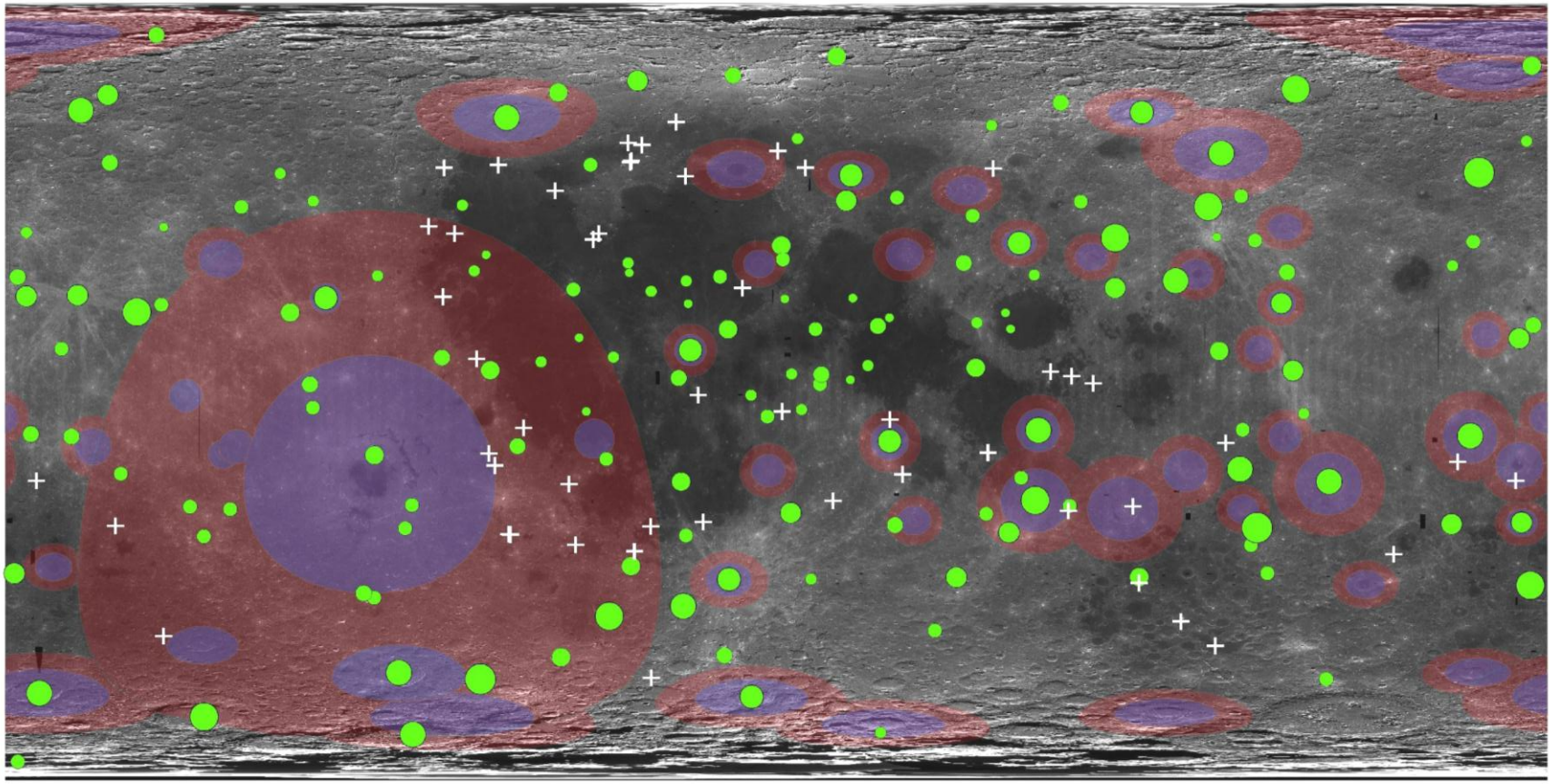

Figure 6.43 Global map showing complex craters, concentric craters and secondary crater fields of young impact features. Purple fields indicate the craters interior and its continuous ejecta blanket. Red fields indicate regions of dense secondary crater populations. White crosses and green circles indicate concentric craters and complex craters, respectively.

Case Studies

This section provides two specific examples of landing sites ideal for accomplishing Science Goal 6c, outlining implementation methods and science questions that could be addressed at these locations.

Antoniadi crater

Located within SPA basin, ~600 km from the South Pole, Antoniadi Crater is 143 km in diameter, and Upper-Imbrian in age (Wilhelms, 1987). It is unusual in that it contains a peak ring and a central peak. The floor of Antoniadi is 9 km below the lunar surface (Araki et at., 2009); it is the lowest point on the Moon. Figure 6.44 shows two possible landing sites with stations for data collection within a 10 km radius exploration zone.

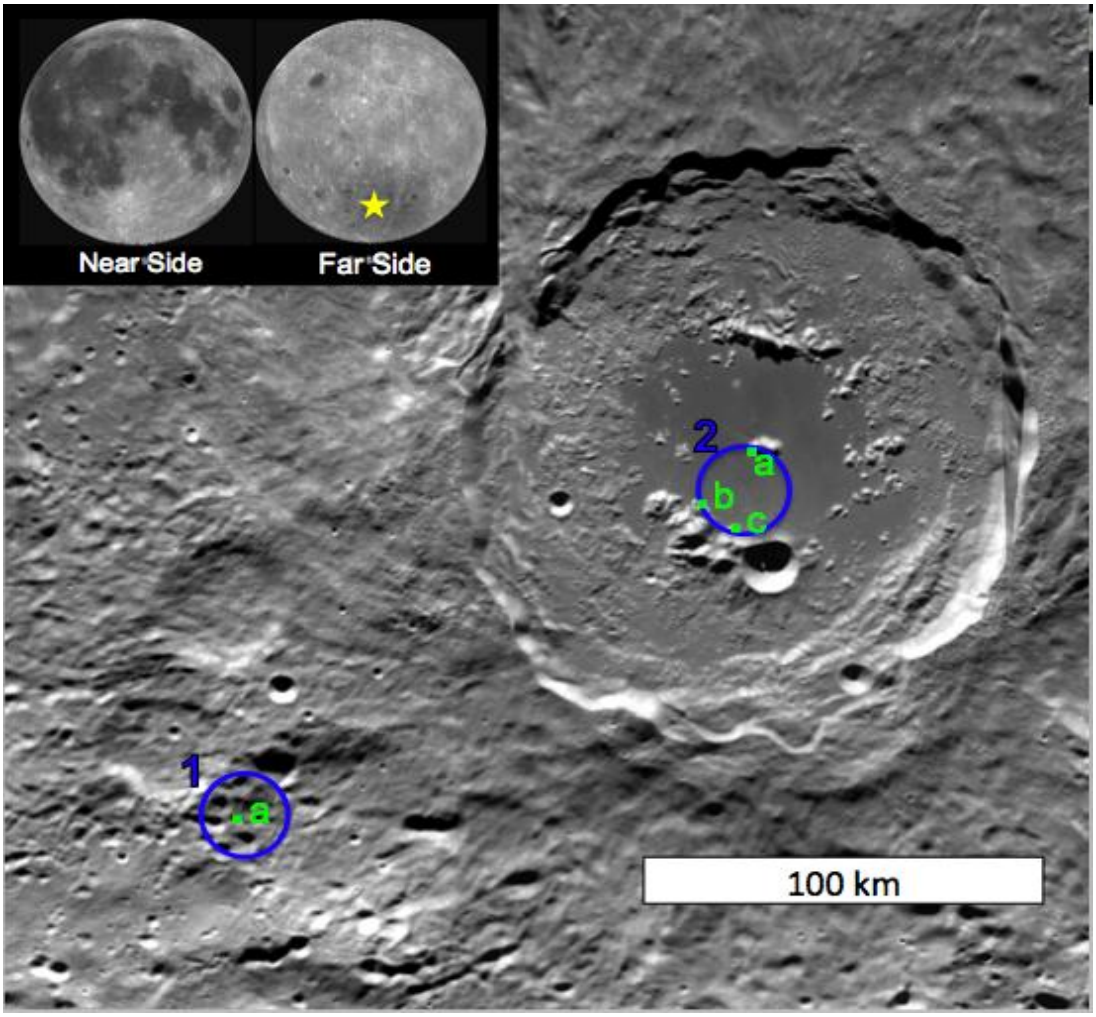

FIGURE 6.44 Mosaic of Antoniadi Crater imaged by Clementine 750nm UVVIS camera. Antoniadi's location is shown by the yellow star on the global map in the top left. Blue circles represent a 10 km radius traverse limit. Locations a, b, and c are illustrated in subsequent figures.

Site 1 is on the ejecta blanket of Antoniadi, southwest of the crater's center. The predicted radial extent of its continuous ejecta blanket is 175 km (Moore *et al.,* 1974), but recent geologic mapping predicts an ejecta blanket with a radius of at least 275 km. Numerous secondary craters can be found in this area (Dominov and Mest, 2009). Scaling laws predict an excavation depth of 14 km, which may be too shallow to excavate mantle material, since gravitational data predicts a 20 km thick crust in this region (Cintala and Grieve, 1998; Wieczorek and Phillips, 1999). Antoniadi's ejecta blanket can be accessed from the excavated material of younger simple craters outside the rim of Antoniadi. Figure 6.45 shows a fresh

simple crater and a secondary crater chain that are in close proximity. Landing in this location would allow geologic examination of secondary craters as well as collection of Antoniadi ejecta. Models of ejecta deposition, excavation depth, and secondary crater morphology could be tested here.

Site 2, within Antoniadi crater, would allow direct sampling of the central peak and the peak ring. Seismometers and gravimeters may be placed along the crater floor to examine the volume of impact melt and the subsurface structure of the peak ring. Sites 2a and 2b show boulders have that have rolled off the central peak and peak ring that would allow sampling without having to ascend possibly hazardous slopes (Figs. 6.46 and 6.47). Antoniadi is estimated to have uplifted from material from 23 km depth (Cintala and Grieve, 1998), so a mantle rich central peak composition would be consistent with uplift models. Possible stratigraphy on peak ring outcrops could also be examined to understand peak ring structure. At station 2c small simple craters have impacted peak ring material and impact melt. These craters could be examined for morphological differences caused by changes in target composition (Fig. 6.48). Excavated material from these craters could also yield definitive samples of impact melt and the peak ring. A landing at this site could reveal the origin of the peak ring, test models of stratigraphic uplift, melt production and melting depth and examine the effect of target composition on crater morphology.

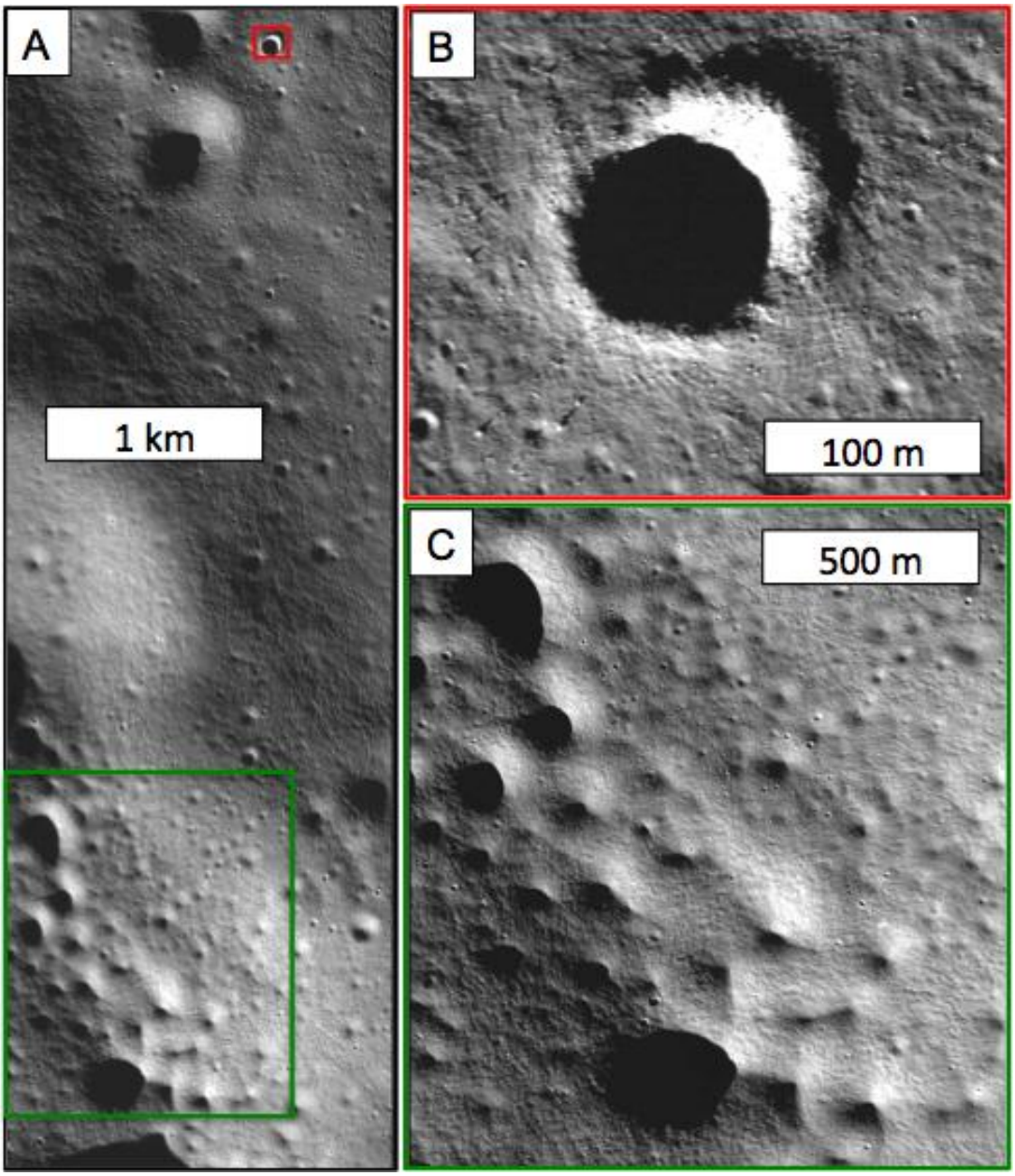

FIGURE 6.45 (a) LROC NAC image M121089722. The red and green boxes highlight a fresh simple crater and a degraded secondary crater. (b) The simple crater at a larger scale. (c) The secondary crater at a larger scale.

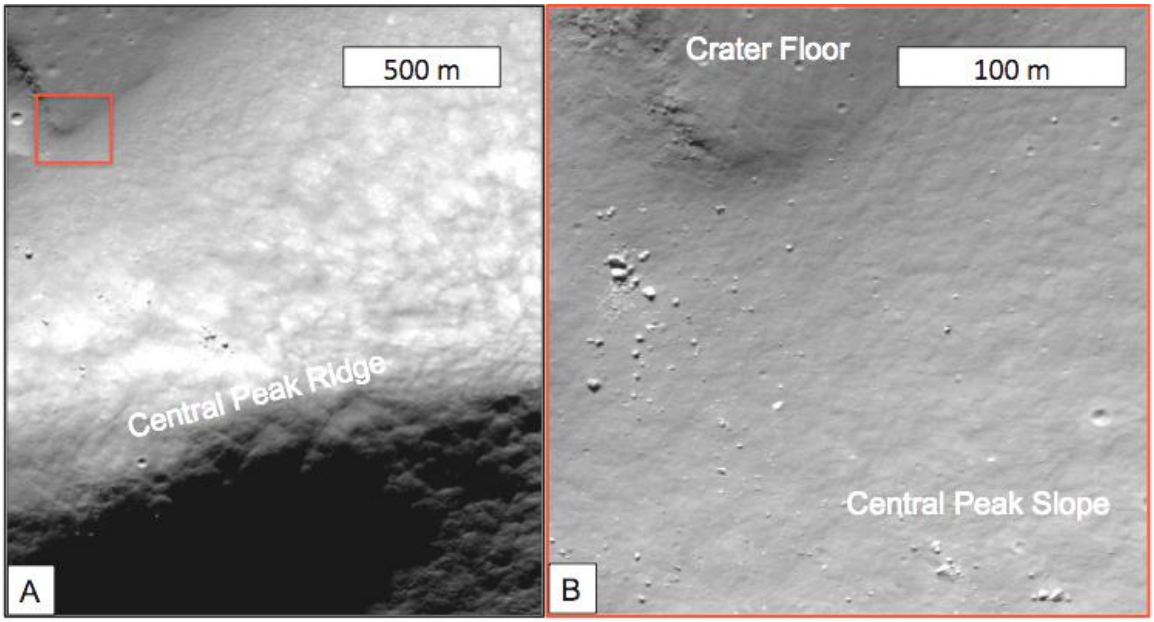

FIGURE 6.46 (a) Central peak of Antoniadi Crater captured by LROC (NAC image M108001035L). The red box highlights fallen boulders that are possibly accessible for sampling. (b) Shows this specific area at a larger scale.

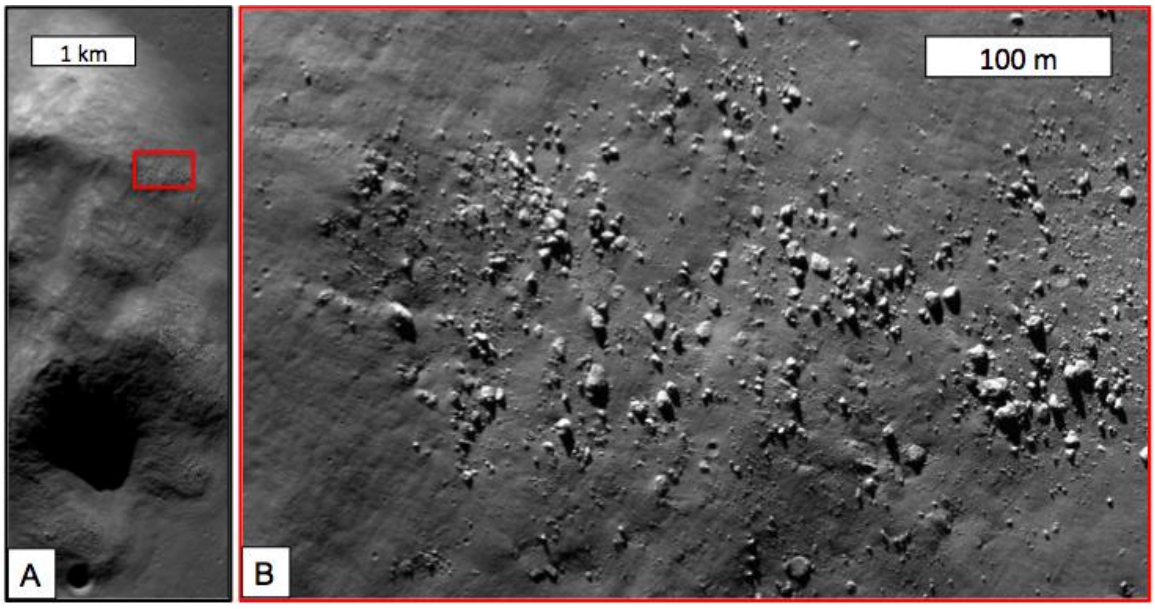

FIGURE 6.47 (a) A segment of Antoniadi's peak ring captured by LROC (NAC image M110371891L). The area within the red box is shown at a larger scale in (b), which highlights possible stratigraphy (in the top left corner) and fallen boulders that could be sampled (towards the right of the image).

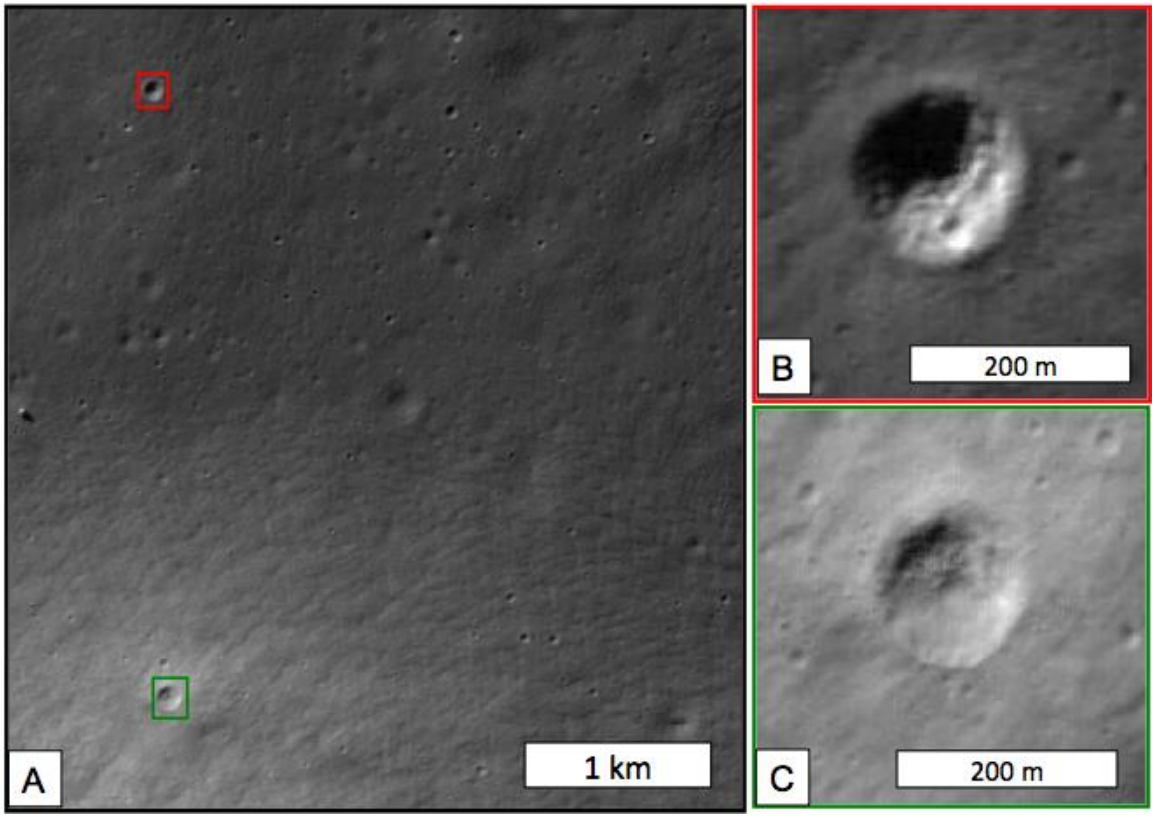

FIGURE 6.48 (a) A portion of Antoniadi Crater captured by LROC (NAC image M10800782R). Red and green boxes highlight simple craters that impacted impact melt and peak ring material; these are shown at the larger scale in (b) and (c) respectively.

Tycho crater

Tycho is one of the most prominent central peak craters on the lunar nearside. It is 103 km in diameter and located on thick highlands crust south of Mare Nubium. The crater is 4 km deep and the central peak rises 2.4 km above the crater floor. The south-western section of its floor is 200 m higher than the rest, probably a result of greater slumping occurring along that section of the crater rim (Margot *et al.*, 1999). Numerous hummocky massifs are irregularly dispersed along the crater floor. These features evolve into more discrete terraces approaching the crater rim and the crater wall is lined with large scarps (Schultz, 1975). Tycho's most striking features are the bright rays that extend for thousands of kilometers across the Moon. One of these rays is thought to intersect the Apollo 17 landing site, 2000 km away, where it may have triggered a landslide dated to be 100 Ma. This is the best age approximation for the Tycho-forming impact event.

Apollo missions to Tycho were considered but not selected as the surface was considered too hazardous to land on. However, Surveyor VII successfully landed 18 miles north of Tycho's crater rim, despite the rugged terrain. Data from Surveyor suggested the local crust was depleted in iron relative to maria (which previous Surveyors that landed in), and that the rock types there were probably impact breccias rather than volcanic flows (Phinney *et al.*, 1969).

Figure 6.49 shows a proposed landing site with a 10 km radius exploration zone depicted by a blue circle. It is possible to investigate both the modification zone (the crater walls) and the central peak within these limits. Station A, shown in Fig. 6.50, shows an example of an appropriate landing site upon a possible pond of impact melt. These impact melts could be found in other locations on the floor of Tycho;

this image from the Lunar Reconnaissance Orbiter narrow angle camera only had limited coverage of the floor of Tycho.

A seismic and a gravity survey could be conducted from the crater floor to determine the volume of impact melt and the structure of the central peak. Samples of impact melt can be collected from small craters on the crater floor, since very little regolith should be obscuring the floor of this young crater. Station B, depicted in Fig. 6.51, shows a segment of Tycho's central peak. At this location samples of central peak material can be collected from boulder falls. Scarps along the central peak could be examined for stratigraphy and structure; Tycho may have uplifted material from 17 km depth in the crust, so samples may have a noritic component to their composition. Station C, Fig. 6.52a, shows boulders that have fallen off of terraces along the crater wall. Possible heterogeneity within the boulders can be seen from orbit. Samples of similar boulders should be collected and crew should examine the crater walls to identify the boulders fall path, as shown in Fig. 6.52b. Compositional analysis of both central peak and terrace material could yield important insights into the cratering process. Models for uplift and central peak and terrace formation could be tested by analyzing samples for shock metamorphic effects and presence of frictional melts.

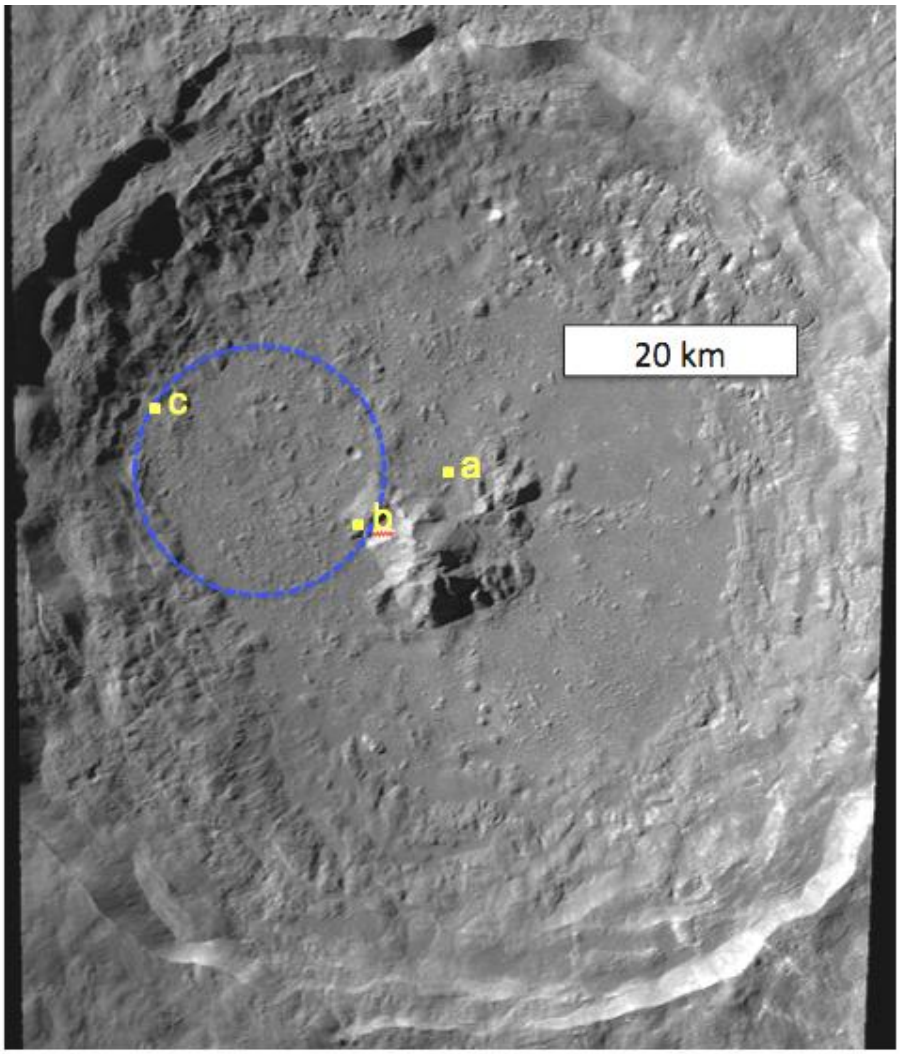

FIGURE 6.49 Tycho crater, 103 km in diameter, located on highlands terrain south of Mare Nubium. Blue circle indicates 10 km radius around a possible landing site. Stations a, b, and c shown below in Figs. 6.50, 6.51, and 6.52, respectively. LROC wide angle camera, image M104584833CE.

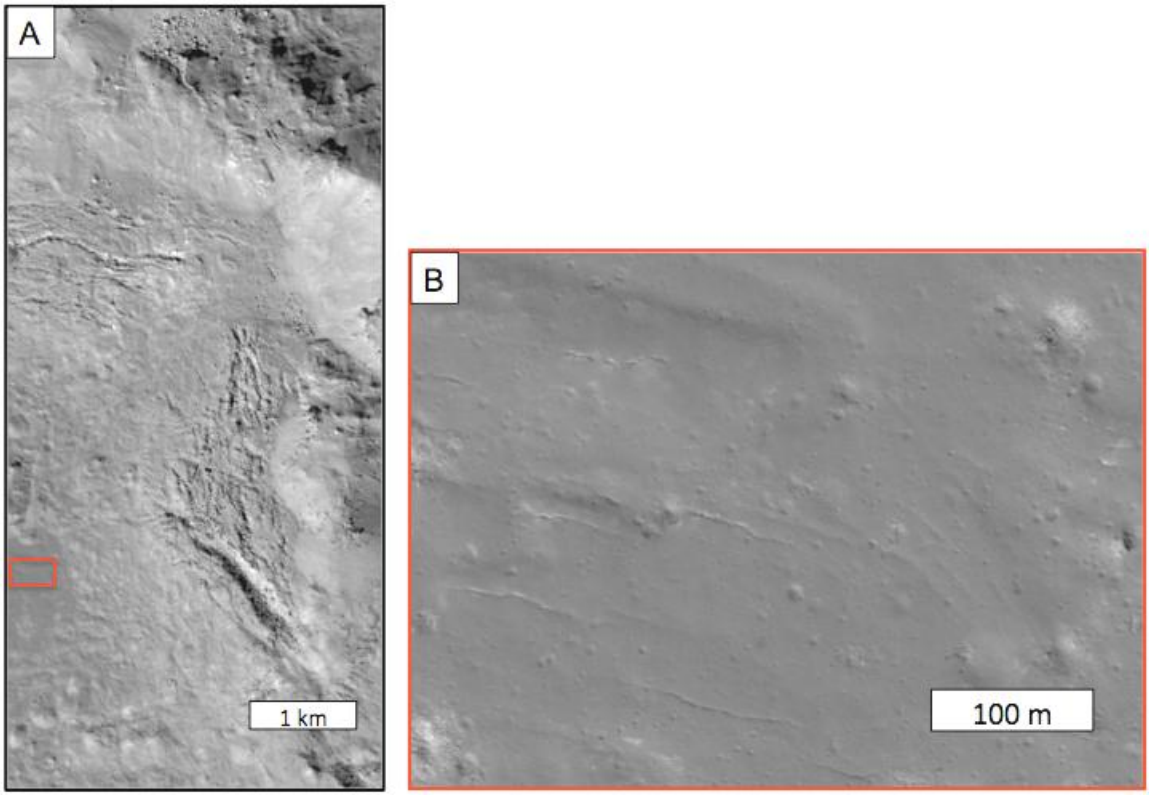

FIGURE 6.50 (a) Tycho crater's floor captured by LROC NAC, image number M121089722R. The red box highlights a flat pond of possible impact melt; an ideal surface to land on. This area is shown at a larger scale in (b).

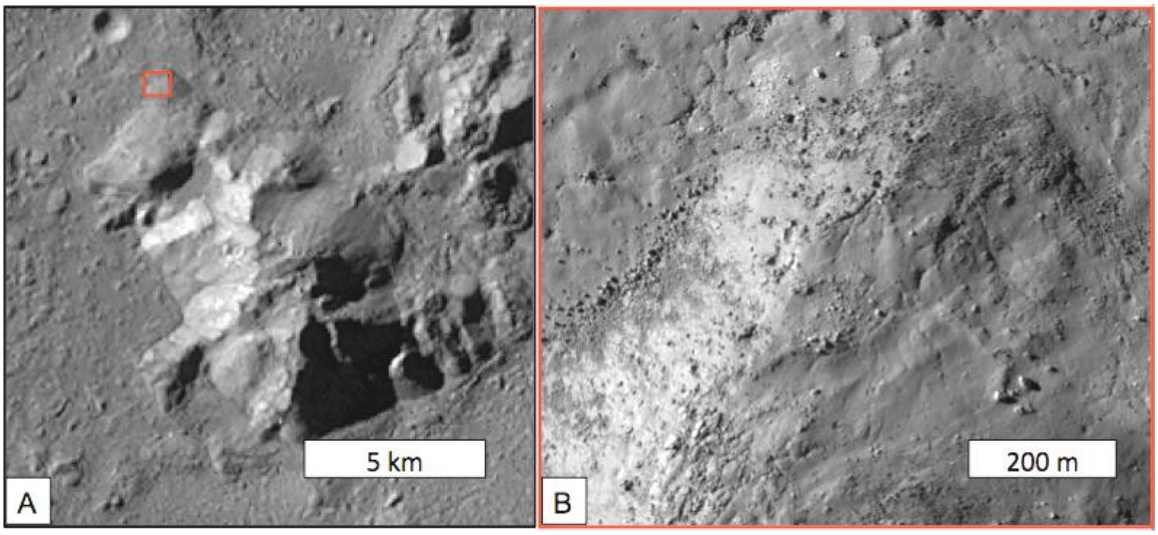

Figure 6.51 (a) Tycho's central peak, cropped from LROC WAC image M104584833CE. The red box highlights a section of central peak with a fresh scarp, possibly produced by faulting, and boulders of central peak material that are accessible for sampling. This area is shown at a larger scale in (b).

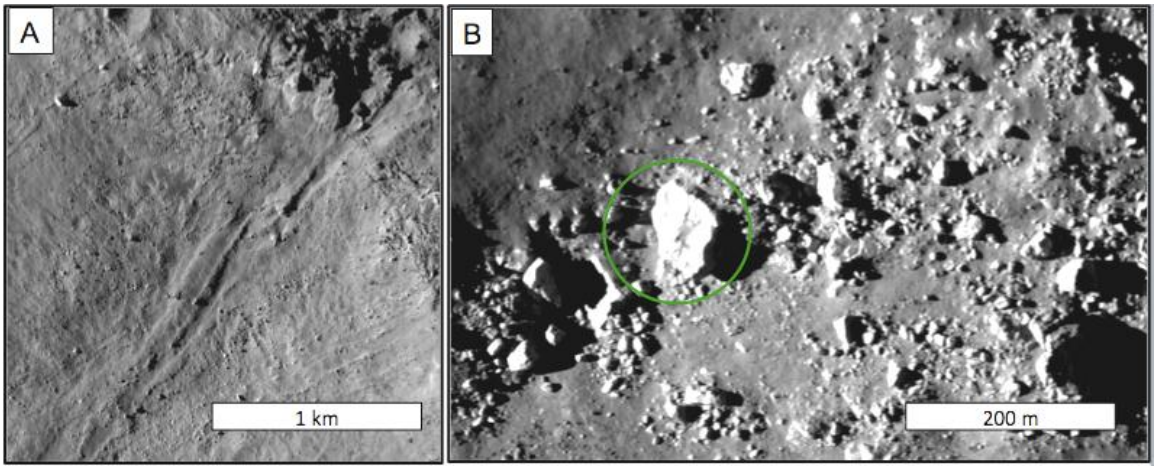

FIGURE 6.52 A portion of Tycho's crater wall imaged by LROC. (a) Boulder tracks along Tycho's crater walls that can be used to track boulders original position (NAC image M116392591R). (b) The green circle shows a large boulder at the base of Tycho's crater wall, that either shows peculiar shadows on its surface or a visible heterogeneity in its composition (NAC image M116392591L).

Conclusion

Numerous methods for studying impact cratering have generated a wide variety of theories, scaling laws, and models pertaining to the impact process; sampling of young lunar complex craters can test these models and theories. The effects of planetary characteristics can be ascertained by visiting multiple craters on different lithologies. Implementation methods include seismic surveys, visual examination of outcrops and the collection of samples from outcrops, boulder falls, and the excavated material of simple craters. Models of stratigraphic uplift, melting and central peak and terrace formation can be tested. Additionally, simple craters, secondary craters and anomalous crater types could be studied to further our understanding of impact cratering. Sample return will allow a thorough analysis of impact-related rocks, further aiding our understanding of impact cratering and adding to the observational data gathered by the mission crews.

SCIENCE GOAL 6D: MEASURE THE EXTENT OF LATERAL AND VERTICAL MIXING OF LOCAL AND EJECTA MATERIAL

Introduction

Impact craters eject material that interacts with the lunar surface on local to global scales. The nature and absolute extent of this interaction is poorly constrained due to the complexity of samples (NRC, 2007). Despite investigations of lunar samples, remote sensing, terrestrial analogs, and experiments, consensus is limited on the extent of lateral and vertical mixing. However, there is evidence for incorporation of local material into ejecta blankets based on geochemical data from Apollo orbital missions. Observations of large impact craters on the Earth and Moon have shown ejecta deposits can extend multiple crater diameters from the crater of origin. These deposits can also be quite thick, on the order of hundreds of meters for basin ejecta (McGetchin *et al.*, 1973).

Material is ejected from a crater as a mixture of impactor and (dominantly) target material. Due to the Moon's low gravity and lack of atmosphere, particles follow a ballistic trajectory that is not affected by base surge (ground hugging), fluid, or turbulent flow (Oberbeck, 1975). Thus, ejecta deposits form predictable facies that are largely the products of initial impactor speed, excavation volume, and excavation angle (Shoemaker, 1960; Oberbeck, 1975). Current ejection and mixing models are heavily biased towards experiments and studies of terrestrial craters; these models may not always be applicable in a lunar regime.

In the following, areas on the lunar surface will be identified where original ejecta mixing ratios are most likely to be preserved based on orbital and spectroscopic observations. Areas of interest will be

focused primarily near Copernican age craters, which by definition have well-preserved ejecta (Wilhelms, 1987). Improvements in remote sensing might yield observational data to calibrate the various estimates of mixing ratios (NRC, 2007). However, direct sampling of crater ejecta is the only definitive way to quantify mixing of local and ejecta material.

Ballistic Sedimentation

The method of ejecta emplacement has significant consequences on resultant morphologic and mixing characteristics. Since the 1960's ballistic sedimentation has been the dominant theory to explain lunar ejection processes (Shoemaker, 1960; Oberbeck, 1975; McGetchin *et al.*, 1973). These models are based on impact experiments, applying or modifying these to fit lunar observations. Some observations of complex crater and basin secondary craters suggest a process other than ballistic sedimentation also plays a role (Haskin, 1998; Haskin *et al.*, 2003).

In ballistic sedimentation models all material is launched from the impact crater in ballistic trajectories (Fig. 6.53). Thus nearly all ejected particles have a horizontal and vertical velocity component. Particles ejected at the same time from the same horizontal profile are ejected at different angles and speeds. In general, material closer to the impact center experiences higher shock pressures and is ejected faster at higher angles relative to the surface. In vertical profiles within the transient crater, initial ejection angle decreases with increasing depth. At some threshold proximity to the transient crater wall, the initial angle of ejecta of a particle is too shallow to overcome crater rim height. As a result, these particles are retained in the transient cavity for greater lengths of time, on the order of tens of seconds to a few minutes rather than a few seconds, resulting in higher comminution (mechanical breakdown) of particles (Schultz and Mendell, 1978).

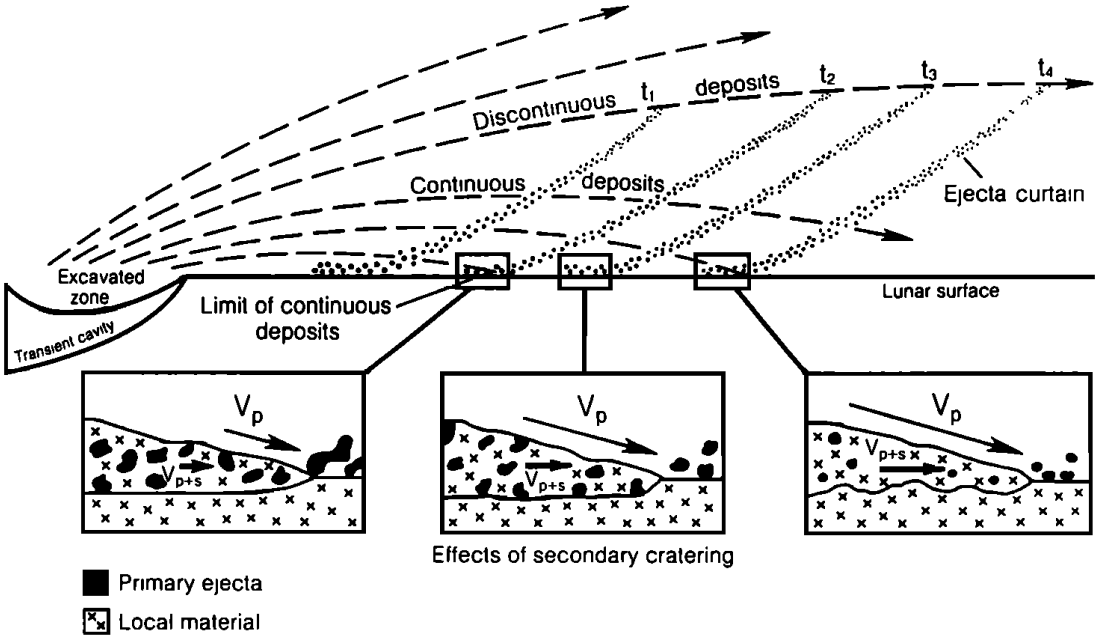

FIGURE 6.53 Ballistic ejection process and effects of particle interaction with preexisting lunar surface as a function of radial range. t, time; V_P, velocity of primary ejecta; V_{P+S}, velocity of mixture of primary and secondary ejecta. Finer-grained fragments (right box) occur higher in the ejecta curtain and were ejected at higher speeds and steeper angles. Larger particles ejected at lower speeds and angles are launched late in cratering, and are concentrated at the base of the curtain (left box). Arrow lengths in boxed sections represent relative velocity magnitude. From Head *et al.* (1993), after Oberbeck (1975).

Particle trajectory (Fig. 6.54) can be modeled by the classic ballistic formula

$$r = (v^2 \sin 2\theta)/g \,, \qquad (6.7)$$

where r is horizontal distance of travel (km), v is ejection speed (km/s), θ is ejection angle (degrees) from the horizontal, and g is gravitational acceleration (km/s^2). This expression does not take into account the radius of curvature of the planet or satellite, or the decrease in gravity with height. However, the error associated with these limitations is small for distances up to ~100 km, or 3^o on the Moon (Shoemaker, 1960). Ejection angles are typically ~45°.

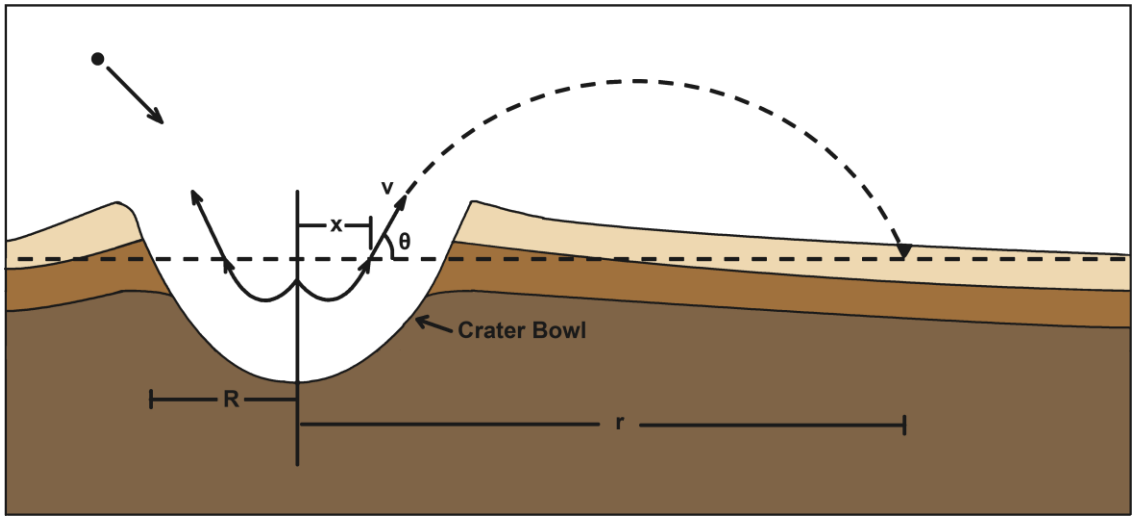

FIGURE 6.54 Schematic diagram of the ballistic trajectory path of a single particle ejected from a crater. *x*, launch position; *v*, ejection speed; *θ*, ejection angle; *R*, apparent crater radius; *r*, distance from crater center. Modified from Housen *et al.* (1983).

Several scaling models have been developed to estimate ejecta thickness as a function of crater size and distance from crater (McGetchin *et al.*, 1973; Pike, 1974; Housen *et al.*, 1983; Moss, 1994). Estimates from different models may vary by an order of magnitude, thus greatly affecting estimates of mixing ratios.

Models of ejecta formation based on terrestrial craters are not directly analogous to the Moon, as gravitational force and atmospheric conditions differ between the two. The lower lunar gravity results in a thinner ejecta deposition profile for the same volume of material ejected on Earth (Fig. 6.55). The Moon's lack of atmosphere results in ballistic trajectories of primary material that are affected only by other ejecta particles. The mushroom-shaped plume and associated fallback deposits of Earth-based large-scale explosions do not occur on the Moon, as this phenomenon is a result of atmospheric influence. Base surges observed in nuclear explosion fallback are probably unimportant when considering ejecta mixing with local material on the Moon as deposition occurs at less than free-fall speed and typical deposits of fine materials are ~1 cm thick (Oberbeck, 1975; Chao *et al.*, 1977). However, a base surge of secondary material results from the horizontal velocity component of ejected material interacting with secondary excavated material (at sites of primary ejecta impact) and interfering with the ballistic trajectory. This horizontal velocity component can result in meter-scale lateral transport and possibly scouring of the lunar surface, entraining local material into deposits. Evidence for scouring comes from the sharp contact and lack of weathered surface between country rock and Bunte breccia of the Ries Crater (Hörz *et al.*, 1983).

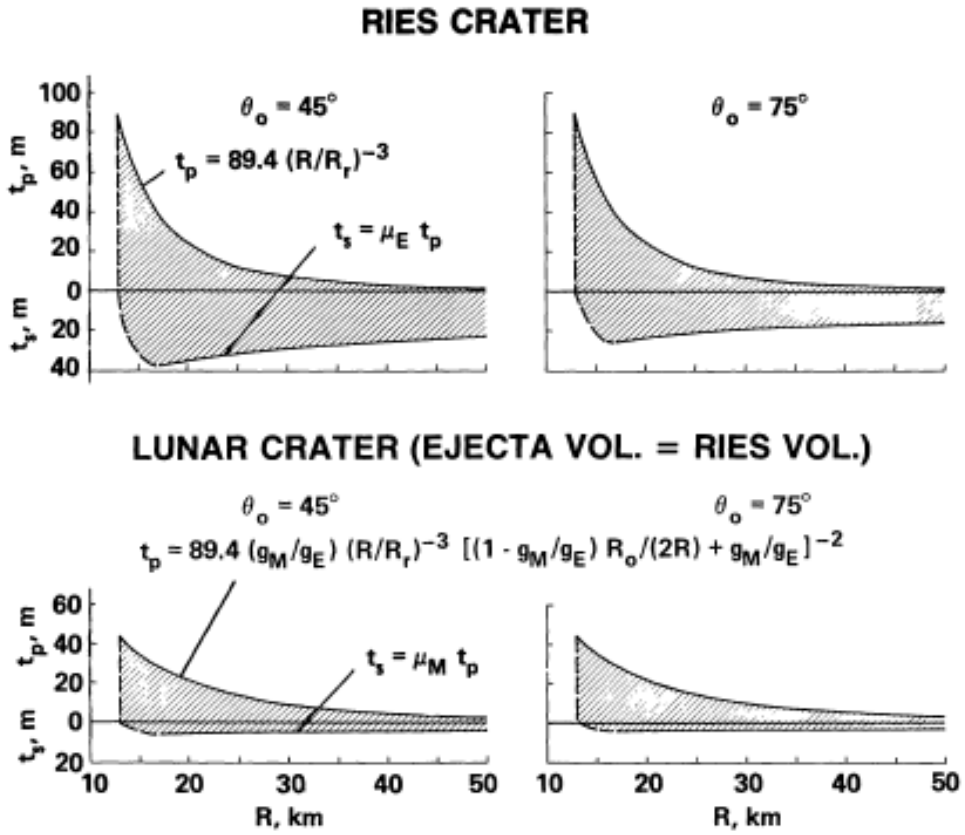

FIGURE 6.55. Calculated profiles (equations as shown) of continuous deposits of the Ries Crater and a theoretical lunar crater with an ejecta volume equal to that of the Ries for ejection angles (θ_0) of 45° and 75°. t_P, thickness of primary ejecta; t_S, thickness of local material incorporated into deposit. (from Morrison and Oberbeck, 1978).

Surface Expressions of Ejecta Deposits

The three generally recognized deposition regimes for craters are (with increasing distance from the crater rim): continuous ejecta, discontinuous ejecta, and rayed material (Fig. 6.56). The extent and nature of these zones varies with crater size and radial distance from the crater. Impact velocity of ejecta increases linearly with increasing distance, while ejecta particle size decreases (Hörz *et al.*, 1991). Near-surface material is excavated first and at the highest velocities and angles, while deeper lithologies are ejected later at lower velocities. This results in a general inverted stratigraphy of ejecta deposits with respect to pre-impact stratigraphy (Fig. 6.57).

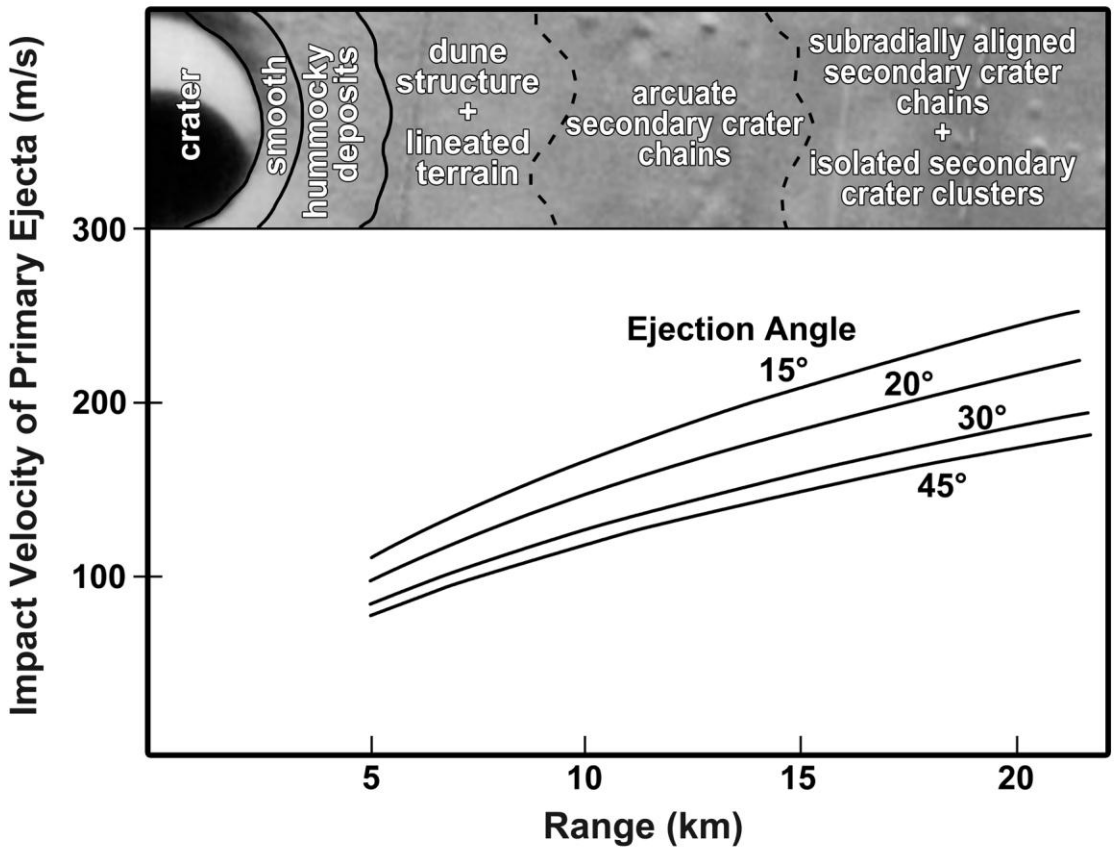

FIGURE 6.56 Idealized crater deposits observable at Lichtenberg B (5 km diameter) and modeled ejection angles and velocities (modified after Settle *et al.*, 1978). Inset image: Lichtenberg B from portion of Lunar Orbiter IV 170-H1.

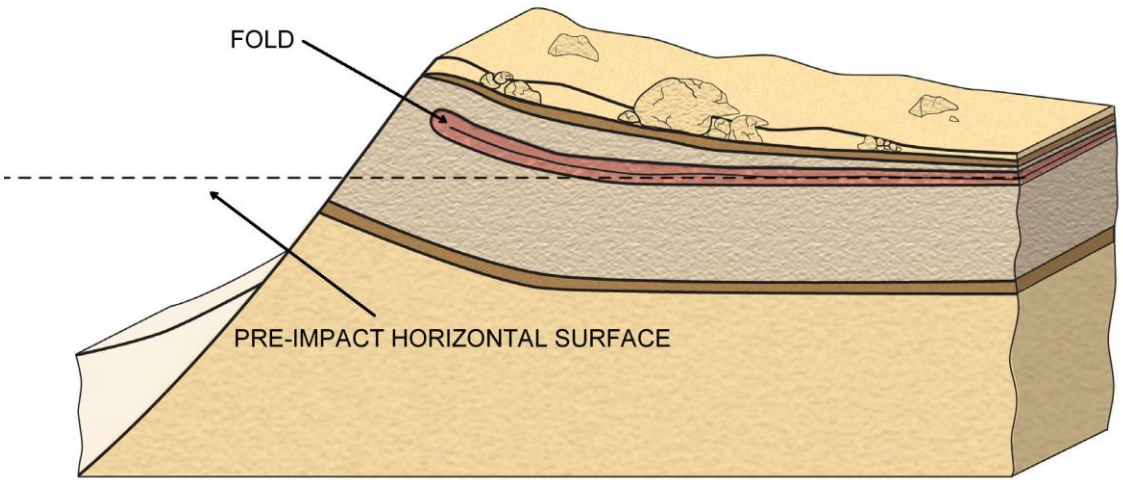

FIGURE 6.57 Illustration of idealized inverted stratigraphy. Modified illustration from Guidebook to the Geology of Barringer Meteorite Crater, Arizona (a.k.a. Meteor Crater), ©2007, David A. Kring, Lunar and Planetary Institute.

The most proximal ejected material form continuous deposits that may completely drape pre-existing ground. Moore *et al.* (1974) measured the radius of continuous ejecta (R_{ce}) deposits for lunar craters in the size range of radius (R) = 0.1–100 km. They determined that R_{ce}/R was constant (~2.3) for craters between 0.3 and 100 km, indicating geometric similarity of ejecta blankets. It has been noted that for large-scale impacts, early ejecta would mix with substrate, with later primary material masking mixed material (Pieters *et al.*, 1985). Despite this intense particle interaction, the bulk of large-scale continuous deposits are deposited at essentially ambient temperatures (Hörz *et al.*, 1983) and low velocities.

The outer periphery of continuous ejecta is lobate and grades into the zone of discontinuous ejecta (Hörz *et al.*, 1991). Discontinuous ejecta deposits tend to be patchy, locally extensive, and have a relatively dense secondary crater population. This zone generally exists within approximately 2.3 to 5 crater radii of the crater center (Fig. 6.58). For small craters, this may be within one kilometer of the crater center, indicating a low threshold velocity for crater formation on the lunar surface (Oberbeck, 1975). Common shallow and elongate craters result from the low angle, higher velocity impact of ejected material (Hörz *et al.*, 1991). Clusters of craters and the beginnings of crater rays also frequently occur in this zone.

Crater rays are relatively narrow, linear, and high albedo ejecta features containing numerous secondary craters (Fig. 6.58). They extend outward from the crater beyond the zone of discontinuous ejecta, though in some cases may be traced back to within a few radii. These features may extend thousands of kilometers from large craters. Tycho has mapped rays up to 2000 km to the northeast with a total covered area of ~560,000 m^2 (Dundas and McEwen, 2007). Many of these rays exhibit gradational boundary contacts, resulting from a combination of soil immaturity and difference in composition between ejecta and local terrain (Pieters *et al.*, 1985). While secondary craters in crater rays may excavate material, the amount of mixing of ray material with pre-existing lunar surface is uncertain. Maximum crater ray thickness estimated for large craters are on the order of 15 m (Pieters *et al.*, 1985). Oberbeck (1971) interpreted the high albedo of some ray elements of Copernicus as the result of relative soil immaturity due to excavation by secondary craters.

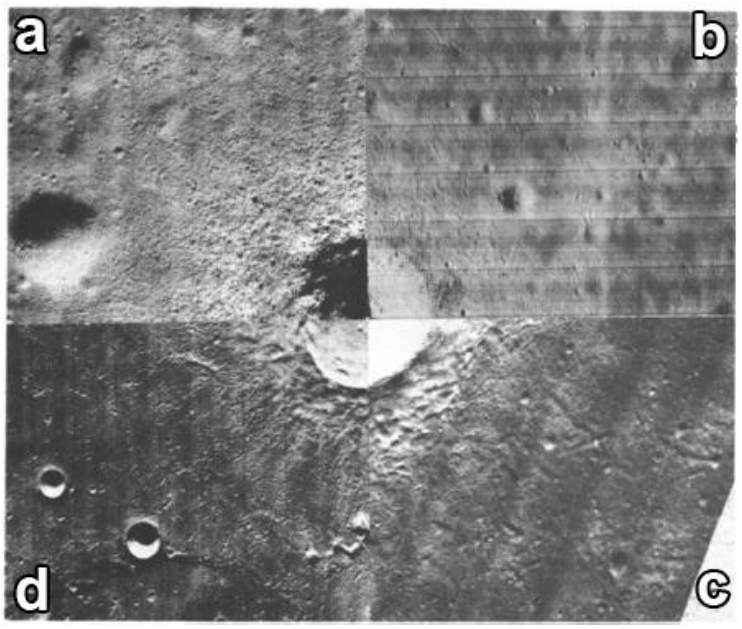

FIGURE 6.58 Photographs of quadrants of four lunar craters of different size, highlighting the changing appearance of continuous deposits and/or secondary crater fields. Photographs have been reduced so that the diameter of each crater is the same in the composite photograph. Crater a is 0.56 km in diameter; crater b is 0.66 km; crater c is 4.2 km; and crater d is 41.6 km. The continuous deposits of crater a drape the surface. Crater b has subdued dunes, while in crater c they are well developed. Hummocky structures are well developed in crater d. Ejecta of the four craters impacted at increasing impact velocity at a given photograph distance from the crater rim in the sequence a, b, c, and d (after Oberbeck *et al.*, 1975).

FIGURE 6.59 Views of the 93 km diameter crater Copernicus and associated ejecta deposits on Mare Imbrium. Left: Clementine basemap V2. Right: Oblique photograph of Copernicus (located near horizon) and secondary crater chains in rays. View is to the south, with the 20 km crater Pytheas in foreground. Apollo 17 Metric photograph AS17-2444.

Spectral analysis is a well-established method of determining surface feature composition (Pieters *et al.*, 1994). Remote sensing spectral studies are a measure of reflected solar radiation at wavelengths ranging from near infrared (NIR, 0.4–1.0 μm) and ultraviolet-visible (UV/VIS, 1.0–3.0 μm). False color mosaics of spectral data ratios are typically used to illustrate spectral variations and are composites of the color ratios:

Red = 0.750 μm / 0.415 μm

Green = 0.750 μm / 0.950 μm

Blue = 0.415 μm / 0.750 μm

Fresh craters are easily distinguished from mature soils (Fig. 6.60); they have a relatively higher albedo, and may have 'greener' or 'bluer' deposits depending on (respectively) if they excavate material with relatively higher or lower abundances of iron and magnesium (Belton *et al.*, 1992). This signature is reduced over time as micrometeoroids and meteoroids garden the lunar surface and average out local differences in composition.

Improvements in remote-sensing capabilities coupled to ground-truth data will yield improvements in estimates of mixing ratios as a function of distance. This has been applied in models and estimates of basin ejecta distribution by several authors (Haskin, 1998; Haskin *et al.*, 2003; Petro and Pieters, 2008). Estimates of Imbrium ejecta volume indicate it would have excavated $1.1–3.2 \times 10^7$ km^3, enough to cover the surface of the Moon to a depth of at least 250 m, assuming even distribution (Haskin, 1998). The Imbrium basin impacted a Th-rich region, and Haskin (1998) suggests Imbrium ejecta is a source of elevated Th over much of Oceanus Procellarum and surrounding highlands. Higher resolution global maps of trace element distribution may be used to trace deposits with unique geochemical signatures; local variations would result from mixing of local and ejecta material.

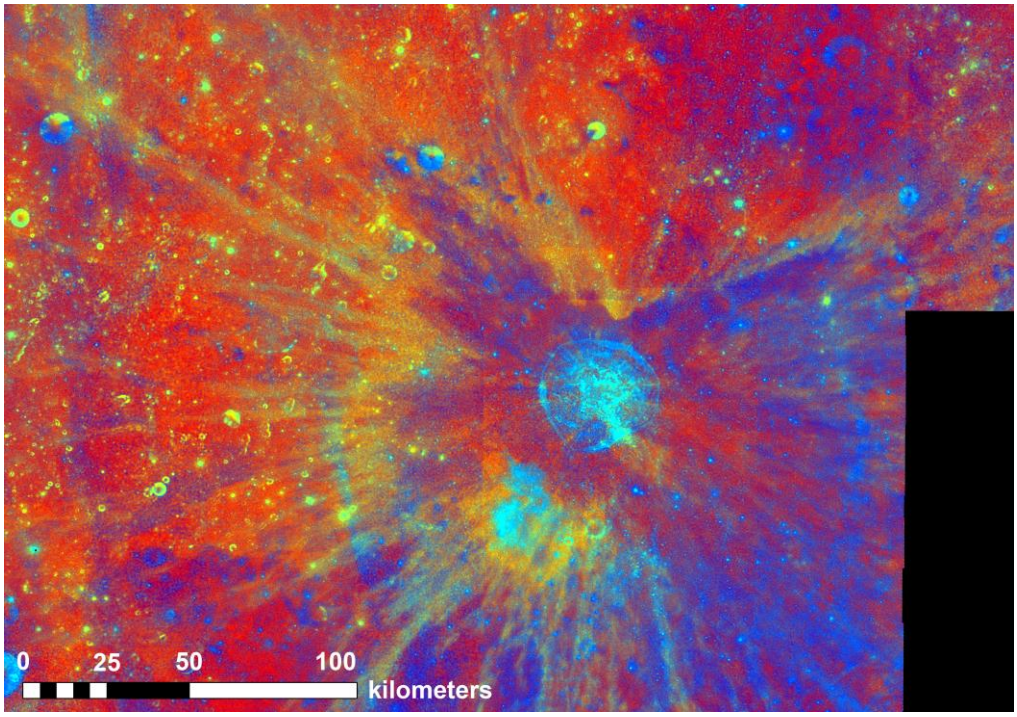

FIGURE 6.60 Clementine false color RGB mosaic of Petavius B, a 33 km diameter crater, and its associated ejecta. Petavius B impacted highland material (to right of crater) and its northwest ejecta extends onto Mare Fecunditatis.

Classification of Ejecta Deposits

The term "impactite" is used as a collective term to identify any rock affected by one (or more) hypervelocity impact(s) (Stöffler *et al.*, 2007). Varieties of lithologies are formed from hypervelocity impacts, and are classified based on texture, degree of shock metamorphism, and lithological components. Impact breccias and impact debris make up the majority of samples returned by Apollo and Luna missions. Lithic breccias and suevites are the major deposits formed outside the rim of the terrestrial Nördlinger Ries Crater (Germany). Monomict breccias result from *in situ* brecciation, whereas polymict breccias dominate ejecta found outside the crater rim. Polymict breccias have two main textures, matrix and clasts, which can be composed of rock fragments, crystallized impact melt, or glassy impact melt. Impact breccia clasts in general are fragments of minerals, rocks, or glassy or partially recrystallized melt bodies. This can include other breccias, resulting in "breccia-in-breccia" textures (Fig. 6.61). The compositions of lunar breccias are consistent with mixtures of known lunar rock types (Stöffler *et al.*, 1979).

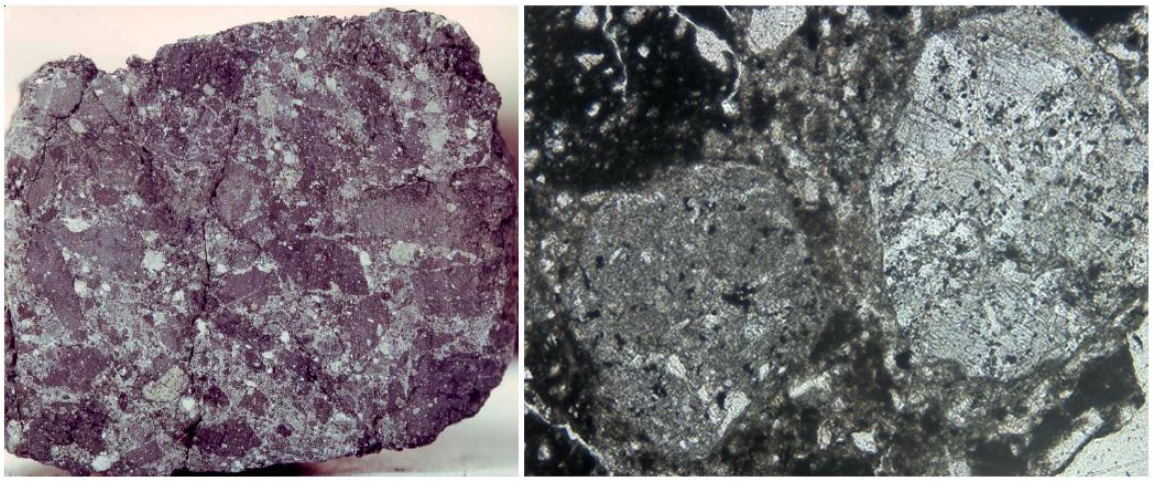

FIGURE 6.61 Macro (left, sawn surface of sample 14306,21, about 6cm across, NASA # S77-22103) and microphotographs (right, plane light view of portion of thin section 14306,4, field of view is 1.15 mm, 10× magnification, Photo # JSC03280) illustrating the breccia-in-breccia texture typical of samples from the Fra Mauro Formation.

Lithic breccias consist exclusively of lithic and mineral clasts, with no melt particles in the matrix, and are generally polymict. This lithology forms the bulk of continuous ejecta deposits, and contains blocks up to several hundred meters in size. In the 24 km diameter Ries Crater, the lithic breccia unit is called "Bunte breccia." The bulk of rock fragments in the Bunte breccia indicate very low shock pressures (<10 GPa), and lithologies from the upper sedimentary units of the target stratigraphy dominate the deposits (Hörz *et al.*, 1983; Kring, 2005). However, Hörz *et al.* (1983) found that both local and ejecta material display pronounced facies and grain size changes over small lateral (<1 km) and vertical scales (<10 m). The chaotic nature of the Bunte breccia yielded pockets and zones of crater-rich or crater-poor materials distributed at random in vertical section. They concluded there is no systematic trend in vertical profile regarding enrichment or depletion of any given lithology (Hörz *et al.*, 1983), while others have described a crude inverted stratigraphy (von Schneider, 1971; Chao *et al.*, 1977). Regardless of its stratigraphic origin, Bunte breccia near the crater rim consists almost entirely of crater ejecta, while 20–30 km away it is composed of 60–80% locally derived material (Kring, 2005).

Suevitic breccias are polymict breccias similar to lithic breccias but contain cogenetic melt inclusions. Both the clasts and melt inclusions originate from the lower stratigraphic section of a target (Stöffler *et al.*, 1979). Outside the crater rim they are called fallout or throwout suevite, as melt fragments often have aerodynamic forms resulting from atmospheric transport during the molten stage. The occurrence of impact melt indicates the material was shocked to much higher pressure (>50 GPa) than the Bunte breccia (Kring, 2005), and originated nearer the crater center. Suevites are deposited as discontinuous layered deposits extending beyond the zone of continuous ejecta (Pohl *et al.*, 1977). They represent a small fraction (generally <5%, though they are 5-8% for the Ries) of the total ejecta volume, though local deposits may be tens of meters thick and contain boulder-size clasts (Pohl *et al.*, 1977; Stöffler *et al.*, 1979).

Shock-lithified lithic breccias and regolith breccias form from the consolidation of debris from multiple impacts. Shock-lithified lithic breccias are similar to lithic impact breccias described above. Regolith breccias contain melt and melt particles formed *in situ*, primarily due to meteoroid and micrometeoroid bombardment.

Recommendations

To accomplish Science Goal 6d, the following requirements must be met at potential landing sites:

I. Target sites with ejecta of known origin

II. Target sites with the potential to yield characteristic mixing ratios of ejecta and local material

III. Target sites that could place constraints on mixing efficiency

Sample return is required to fulfill these goals and determine the nature and extent of ejecta mixing. To minimize heterogeneities resulting from small-scale sampling bias, a large volume of material may be required from each site. Ground-level photo-documentation of ejecta outcrops could supplement these samples and aid in post-mission analysis of emplacement histories. The current study is limited to the area between 70°N and 70°S due to limits of resolution of the global Clementine images at the poles.

The Moon has an extensive crater system, and almost any surface mission will have the opportunity to sample ejecta material. Not all sites are ideal, however. From the above discussion of crater characteristics, the following constraints are recommended in the search for ideal sampling sites.

Young and fresh craters

The most recent craters are more likely to have preserved ejecta deposits. In lunar geochronology, rayed craters are assigned to the Copernican period (from the present to ~1.1–0.9 Ga). The high albedo deposits of rays result from a combination of soil immaturity and differences in composition between ejecta and local material, and thus these deposits are likely to be relatively young in age.

Craters of variable size

Sampling ejecta from a range of crater sizes will be necessary to constrain the effects of scaling on mixing ratios. According to ejecta thickness models, the largest simple craters should have at least 10 m thick continuous ejecta deposits up to 20 km from the crater rim. Thus a single mission to a simple crater could thoroughly sample the full extent of a continuous ejecta deposit. The simple crater Euclides M is examined as a potential case study.

The ejecta of complex craters is too broad and thick to adequately sample the full lateral and vertical extent during a single mission. The focus of missions to large ejecta deposits should be on the transition zone between continuous and discontinuous ejecta (2–3 radii from the crater center). Doing so would avoid late stage, low velocity deposition that could potentially mask the majority of ejecta nearest the crater rim. The 33 km diameter crater Petavius B is investigated further as a case study.

Samples of basin ejecta may yield information on mixing efficiencies at a global scale. Apollo missions sampled formations from the Imbrium, Serenitatis, and Nectaris basins. Mapped basin deposits are also accessible sites of large-scale ejecta. Due to architectural limits of roving capability, only a small fraction of the lateral extent of basin ejecta could be sampled in a single mission. Therefore, improved remote sensing data coupled to new ground truth may be more suitable for determining mixing ratios at these scales. Information on the complete list of craters used in this study can be found in Appendix B.

Compositionally distinct ejecta

The origin of clasts from polymict breccias is significantly easier to establish than those of monolithologic breccias. The simplest method to determine mixing ratios of any two substances is to start with two distinct end-members. On a broad scale, the mare and highlands are significantly different in composition and have extensive contacts. Thus a crater ejecting exclusively highland material onto mare (or vice versa) would yield the best chance for determining mixing extent solely by emplacement processes.

Figure 6.62 shows the 52 Copernican craters recommended for further investigation, considering the constraints discussed above.

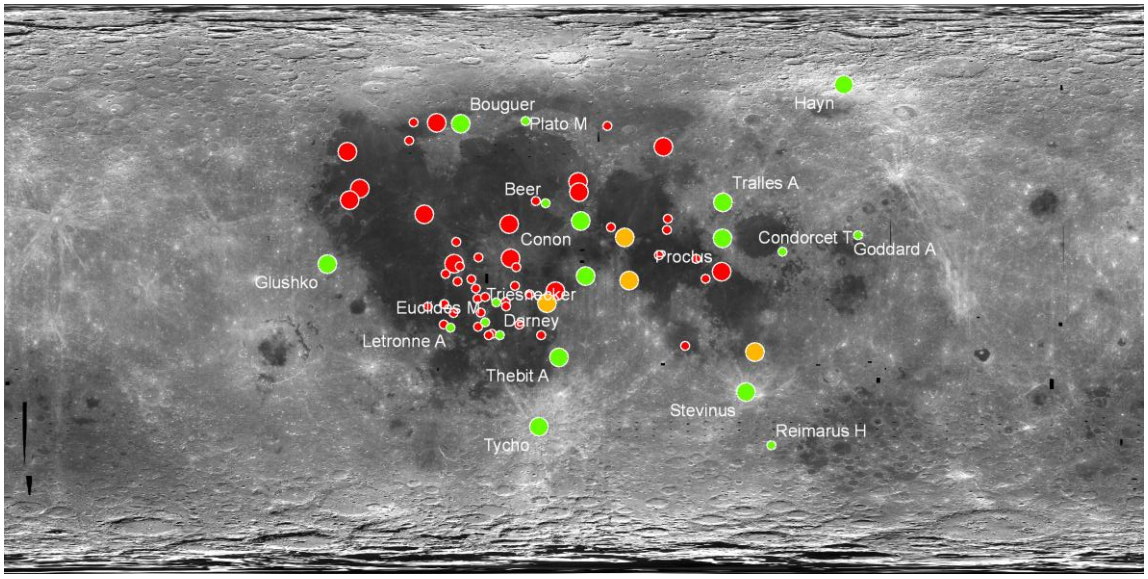

FIGURE 6.62 Fifty two Copernican craters recommended for further investigation. Red circles are highest priority craters, excavating highlands and depositing ejecta on mare; green triangles are high priority craters on highland outcrops in mare; blue squares are low priority craters excavating through mare to underlying lithology.

Case Study: Petavius B Crater

Located on the lunar nearside (-19.90°N, 57.10°E), Petavius B is a complex crater with a diameter of 33 km (Fig. 6.63). High albedo rays are visible over 200 km from the crater center. Based on the butterfly ejecta pattern, Petavius B was formed by an oblique impact from the north. It impacted the edge of highland plains and deposited a significant portion of ejecta on the southeastern margin of Mare Fecunditatis.

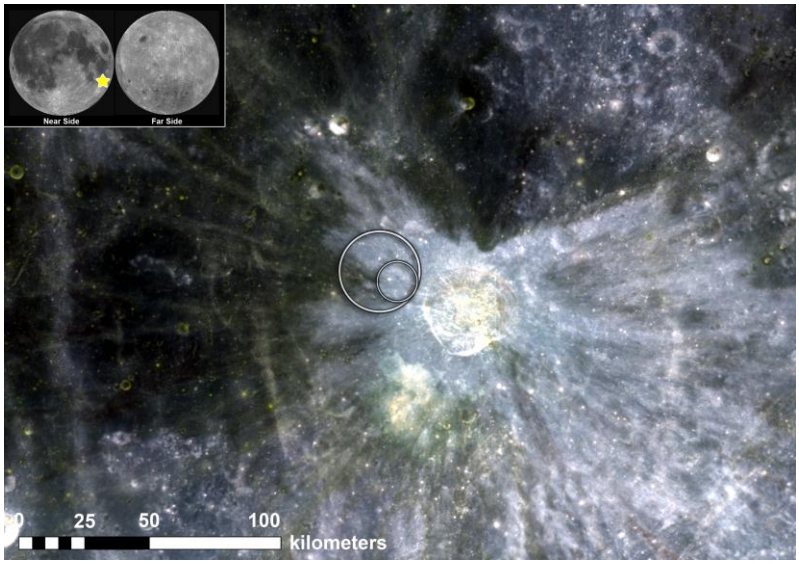

FIGURE 6.63 Petavius B (33 km diameter) is located on the margin of Imbrium plains and Petavius ejecta. Ejecta from Petavius B extends onto the southeast of Mare Fecunditatis. The small and large circle (image center) are 10- and 20-km-radius traverse limits. Upper-left inset image shows approximate location of Petavius B (gold star) on eastern limb of the lunar near side. Clementine UV/VIS color mosaic and inset Clementine 750 nm global albedo.

The ejecta spectra of Petavius B show a marked compositional difference from the mare. The FeO and TiO_2 (wt %) abundance of the continuous ejecta zone is significantly lower than the mare but comparable to the highlands (Fig. 6.64). Abundant boulders and small recent craters are the best targets for sampling ejecta from Petavius B (Fig. 6.65). A 10- or 20-km traverse could sample much of the proximal ejecta deposits. Initial missions to determine the extent of mixing will need to focus on proximal deposits in order to ensure the original composition of ejecta is well characterized.

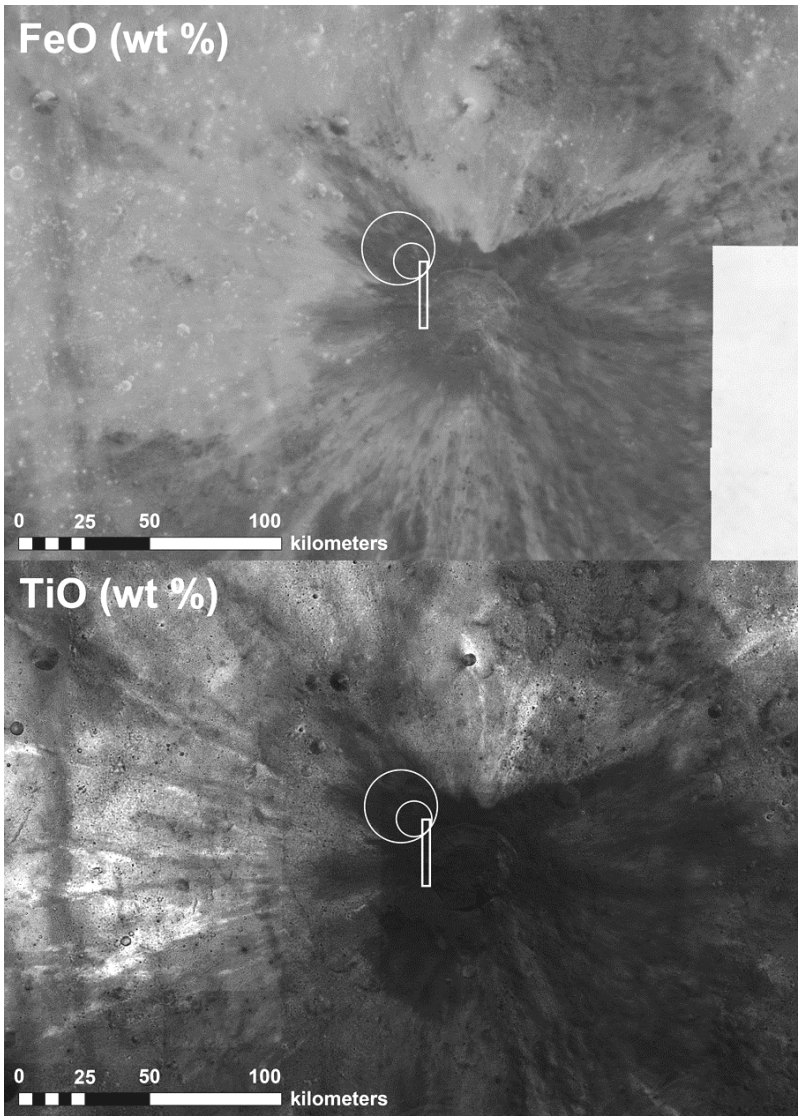

FIGURE 6.64 High-resolution Clementine mosaic of FeO (top) and contrast enhanced TiO_2 (bottom) wt % abundance maps for Petavius B. Lighter shades represent higher abundances of the respective element. Solid white circles represent 10- and 20-km-radius traverse paths. Rectangle indicates approximate area shown in Fig. 6.65.

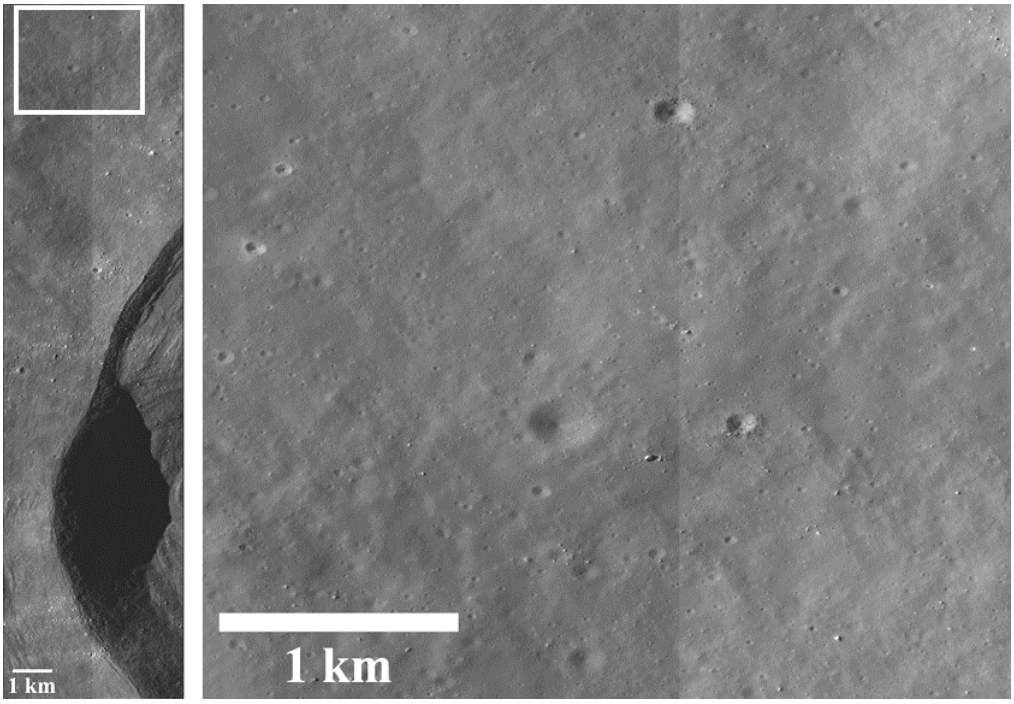

FIGURE 6.65 Northwest rim of Petavius B crater (left image), with box highlighting (right image) boulders ~5 km from the rim as likely sample targets. Mosaic of portions of LROC paired images M119482428LC and M119482428RC.

Case Study: Euclides M Crater

Located on the lunar nearside (10.40°S, 28.20°W), Euclides M is a simple crater with a diameter of 6 km (Fig. 6.66). The impact into a highland rise resulted in deposition of ejecta onto the western margin of Mare Grigoris. Due to its small size, the ejecta of Euclides M is not as extensive as Petavius B.

The relatively higher albedo of ejected highland material is apparent, and in conjunction with spectral data allows for a mapping of the regional extent (Fig. 6.67). Clementine spectral data is available for most of this region, although there is a gap in some datasets approximately one crater radii east of the rim of Euclides M. Nearly the full extent of ejecta can be sampled from this site in one mission, as the material ejected is unlikely to extend beyond 10 crater radii (~30 km). Mare Grigoris is a flat, relatively easily traversable region, as indicated by elevation profiles of the area (Fig. 6.68). The estimated ejecta thickness at the crater rim is ~240 m.

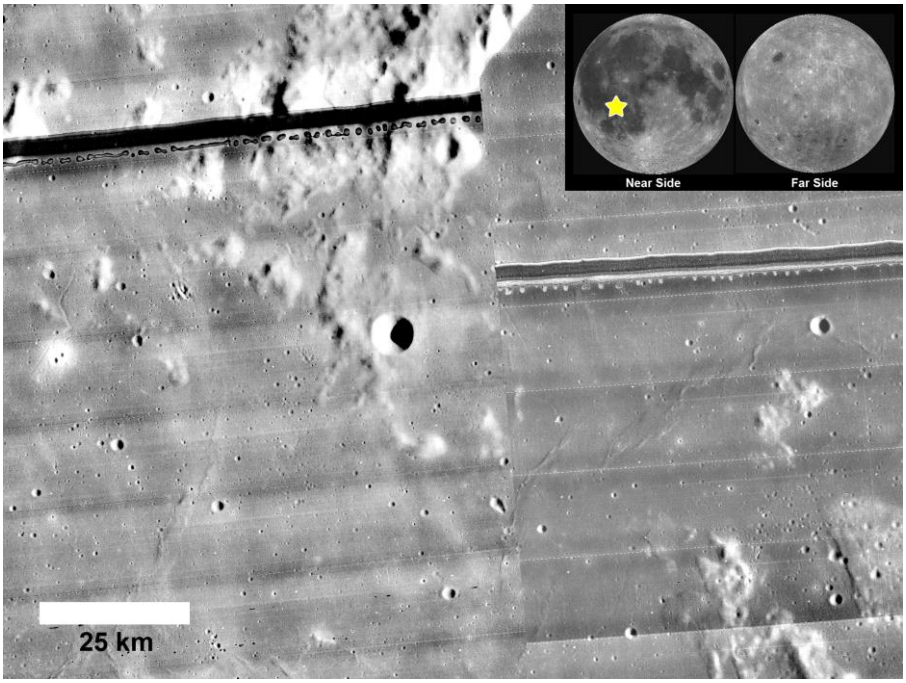

FIGURE 6.66 Lunar orbiter mosaic of the region surrounding Euclides M, showing location on edge of highland material and ejecta deposits extending (eastward) onto Mare Grigoris.

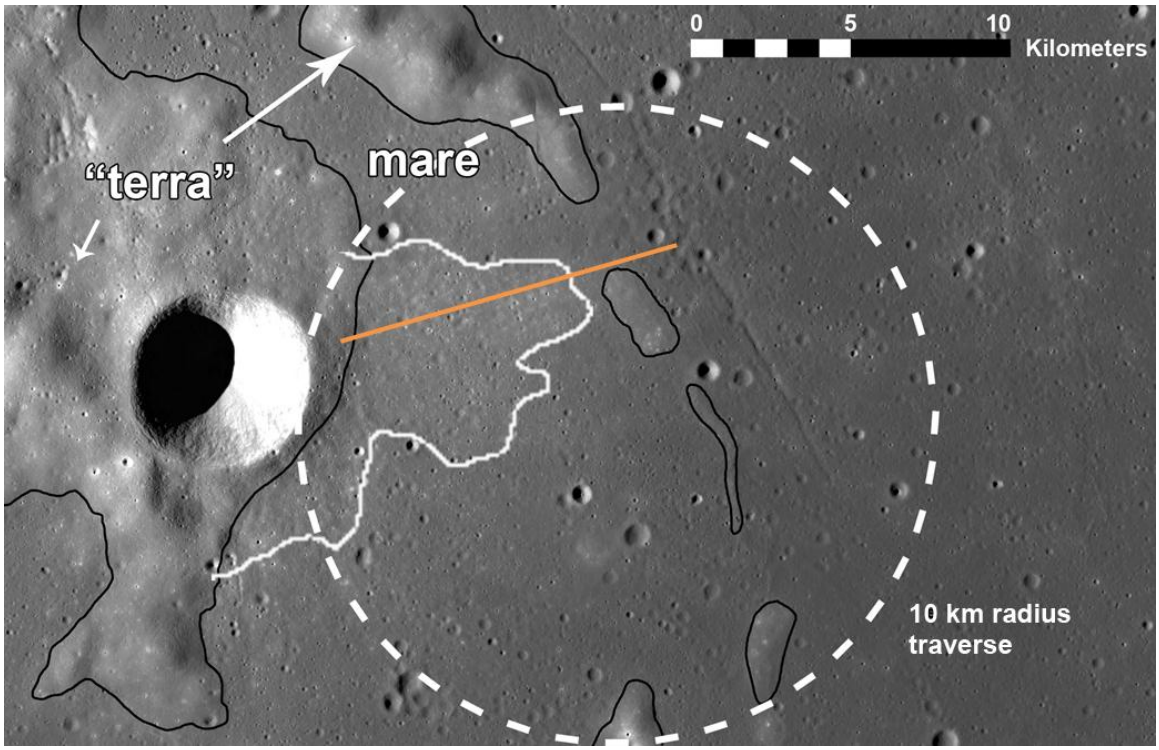

FIGURE 6.67 General geologic divisions within Kaguya/SELENE image TC_EVE_02_S09E330S12E333SC mapped by solid black lines. Solid white line indicates highest-albedo portion of ejecta from Euclides M. White dashed circle indicates 10-km-radius traverse. Orange line indicates profile in Fig. 6.68.

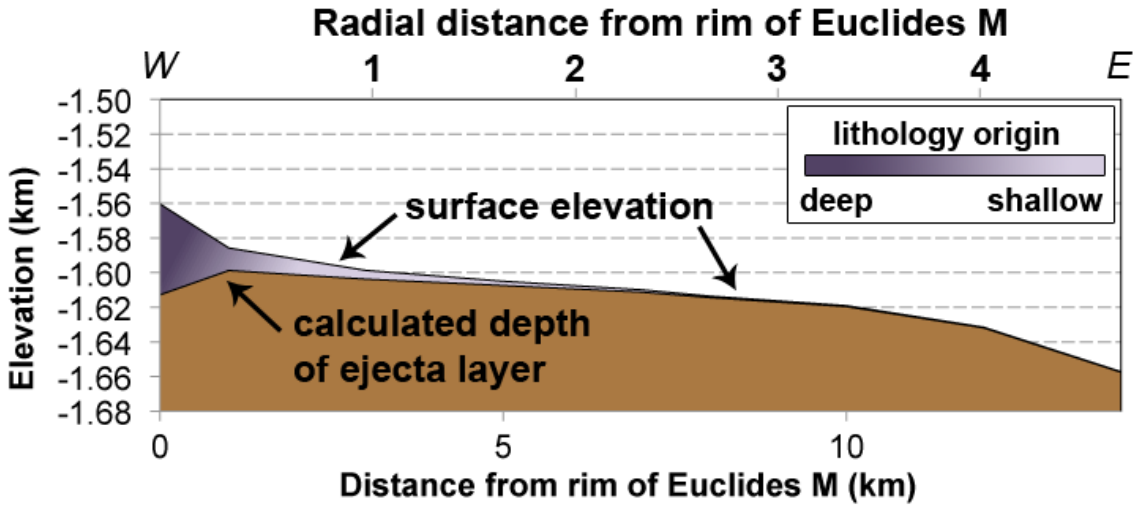

FIGURE 6.68 Elevation profile radially away from Euclides M, with modeled ejecta thickness superimposed.

Conclusions

The sites identified here can help determine the extent of lateral and vertical mixing of local and ejecta material. The Apollo missions sampled abundant impactites that showed the variety of lithologies that impacts produce. Complex mixing ratios resulting from multiple impacts can be better constrained by examining the ejecta of young, fresh craters. Understanding the process of ejecta deposition and mixing across the Moon will improve our knowledge of lunar surface evolution.

CONCEPT 6 CASE STUDY – MAUNDER CRATER, WITHIN ORIENTALE BASIN

We present a case study locality where all of the Science Concept 6 Science Goals can be addressed: Maunder Crater, within Orientale Basin.

Orientale Basin (Fig. 6.69) is an Imbrian aged multi-ring basin located on the western limb of the Moon. It has a topographic rim diameter of 930 km (the Montes Cordillera), and contains two rings within this (the Outer and Inner Rook Rings) with diameters of 620 km and 480 km, with another less prominent ring of diameter 320 km; this ring is referred to as the Inner Shelf Ring in this report. Maunder Crater (Fig. 6.70) is a 55 km diameter complex crater of Eratosthenian age. It is located on the edge of the Inner Shelf Ring of Orientale, within the Maunder Formation, approximately 150 km due north of Orientale's center.

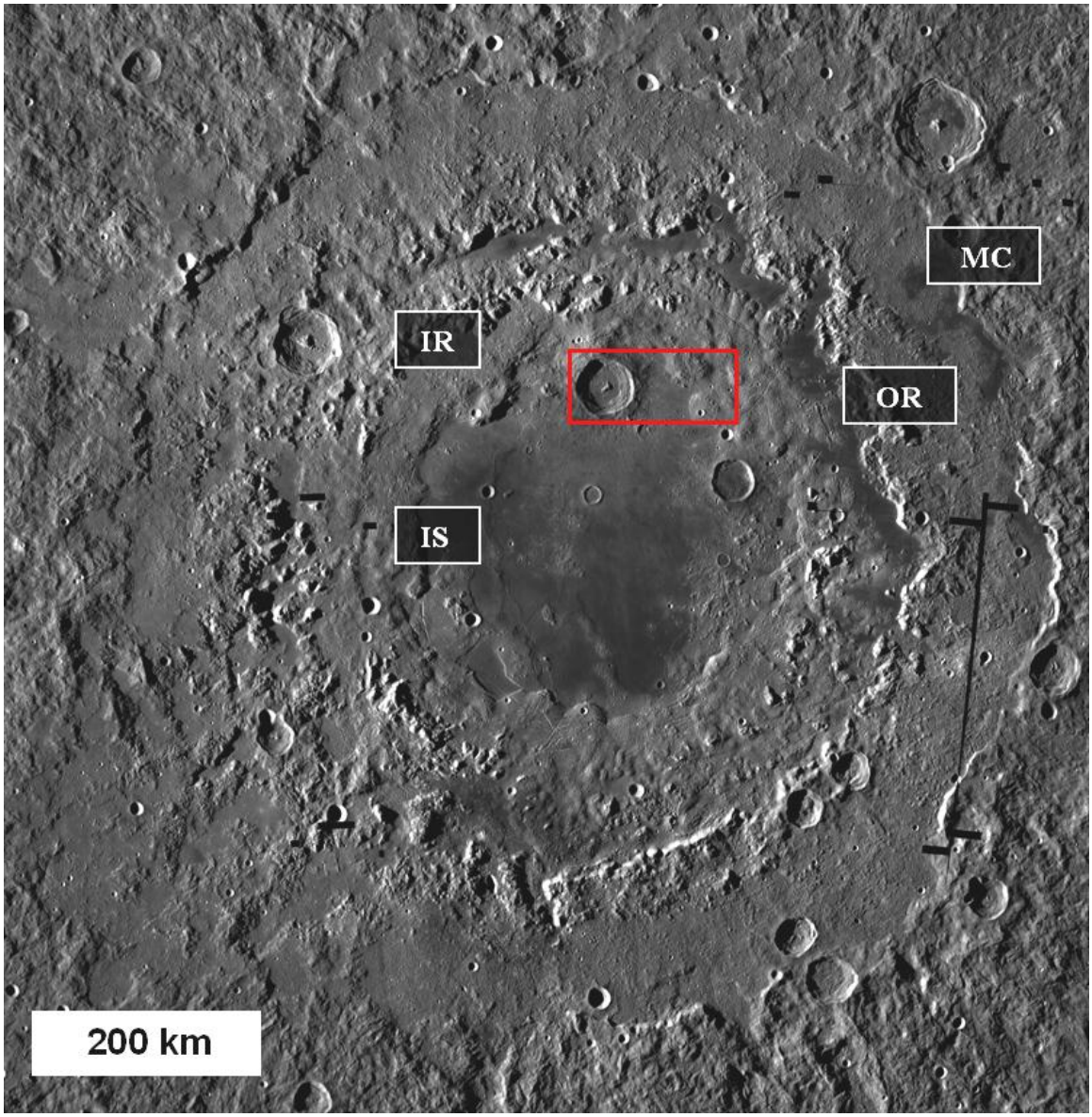

FIGURE 6.69 Orientale Basin. Maunder Crater is highlighted by the red box. IS: Inner Shelf Ring, IR: Inner Rook, OR: Outer Rook, MC: Montes Cordillera (LROC WAC mosaic, Arizona State University).

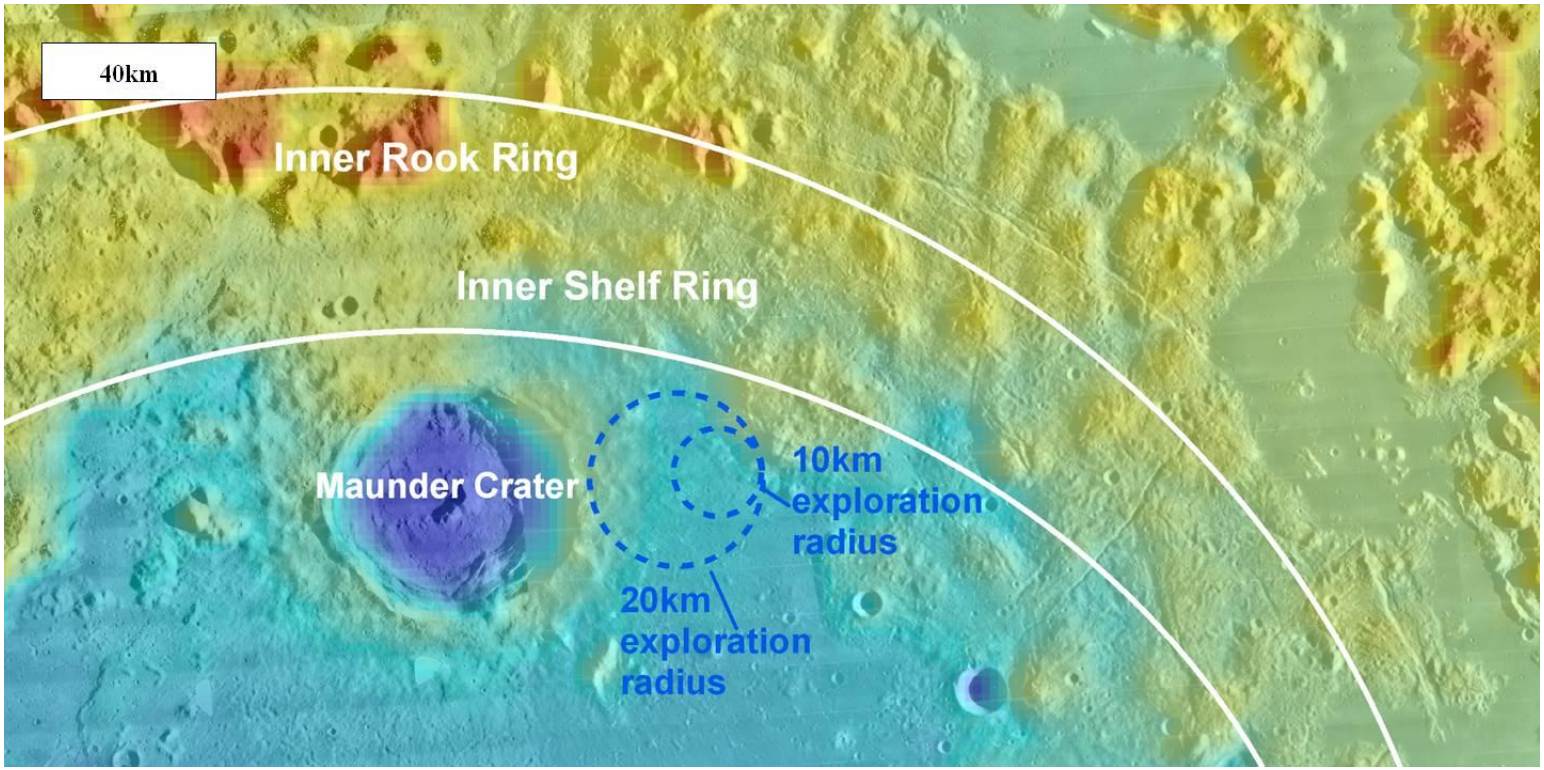

FIGURE 6.70 Kaguya altimeter data overlaying a Lunar Orbiter mosaic; colors represent elevation. Blues are lows, reds are highs. Maunder Crater; the Inner Shelf Ring and the Inner Rook Ring are highlighted. The proposed sampling zones are highlighted by the 10 and 20 km exploration radii. Within these, all of the Concept 6 science goals can be investigated.

Maunder Crater was suggested as a location for an unmanned sample return mission by Wilhelms (1985), but this location was not included as either a tier 1 or tier 2 site by a 2005 survey by the Exploration Systems Architecture Study (NASA, 2005). Maunder Crater is selected here because it is the only location within Orientale that provides access to a well preserved central peak crater, Orientale's melt sheet, and peak ring material. Access to all of these is required to accomplish every goal of Science Concept 6.

Sampling Localities (Figs. 6.71, 6.72, 6.73)

Orientale melt

Maunder Crater impacted into the proposed edge of the Orientale melt sheet. Scaling laws suggest Maunder would have excavated material to a depth of ~4.5 km. Orientale's melt sheet is estimated to be ~10.5 km thick at its center, thinning towards its edge. The Maunder-forming impact should therefore have excavated Orientale melt sheet, which should be contained in its ejecta and be accessible to crew for sampling. This therefore addresses Science Goal 6a.

Inner shelf ring

Though not as topographically prominent as other ring structures at Orientale, the Inner Shelf Ring provides the opportunity to study a multi-ring basin ring. Boulder falls or exposed stratigraphy can be sampled to infer the composition and structure of this inner ring, and therefore help to address Science Goal 6b.

Maunder ejecta

The proposed traverse extends 40 km (~1.5 crater radii) from the rim of Maunder. Within this range, Maunder ejecta will be ubiquitous as it is the largest and most recent crater within several hundred kilometers of the site. There is an estimated 270 m of ejecta at the crater rim, with thickness decreasing to ~20 m at 1.5 crater radii from the rim. Based on estimates of mixing efficiencies, the percentage of primary material should decrease from ~80% to ~40% over this range. The variable spectral composition of Maunder and its ejecta indicate it excavated material of different or variable lithologies, which may make estimates of mixing ratios more difficult to ascertain. The increase in local material with increasing distance may also account for some of the observed variation. Sampling the ejecta will help to address Science Goals 6c and 6d.

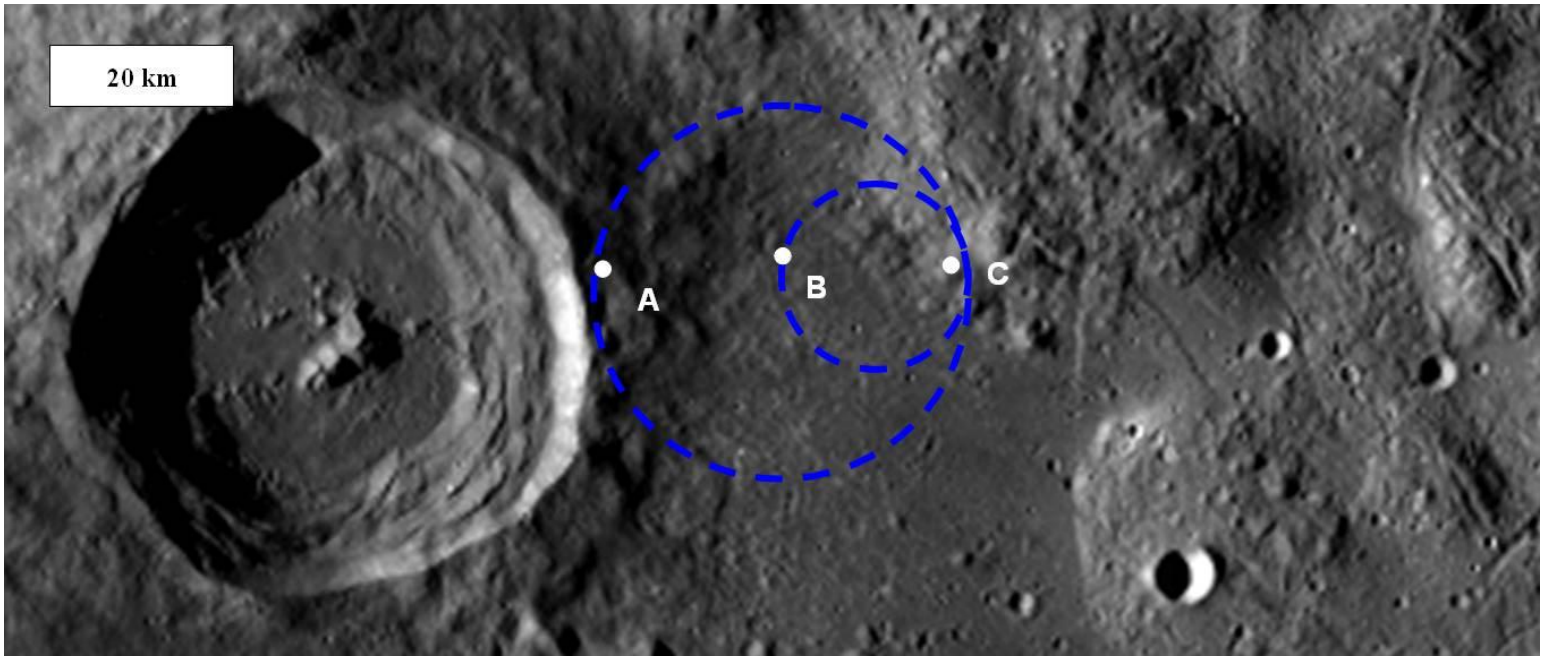

FIGURE 6.71 Maunder Crater and the extent of 10 and 20 km exploration radii. Three sample localities are highlighted: A, B, and C. At A and B Science Goals 6a, 6c, and 6d, can be addressed through the sampling of Maunder's ejecta. At locality C, Science Goal 6b can be addressed through the sampling of the Inner Shelf Ring massifs.

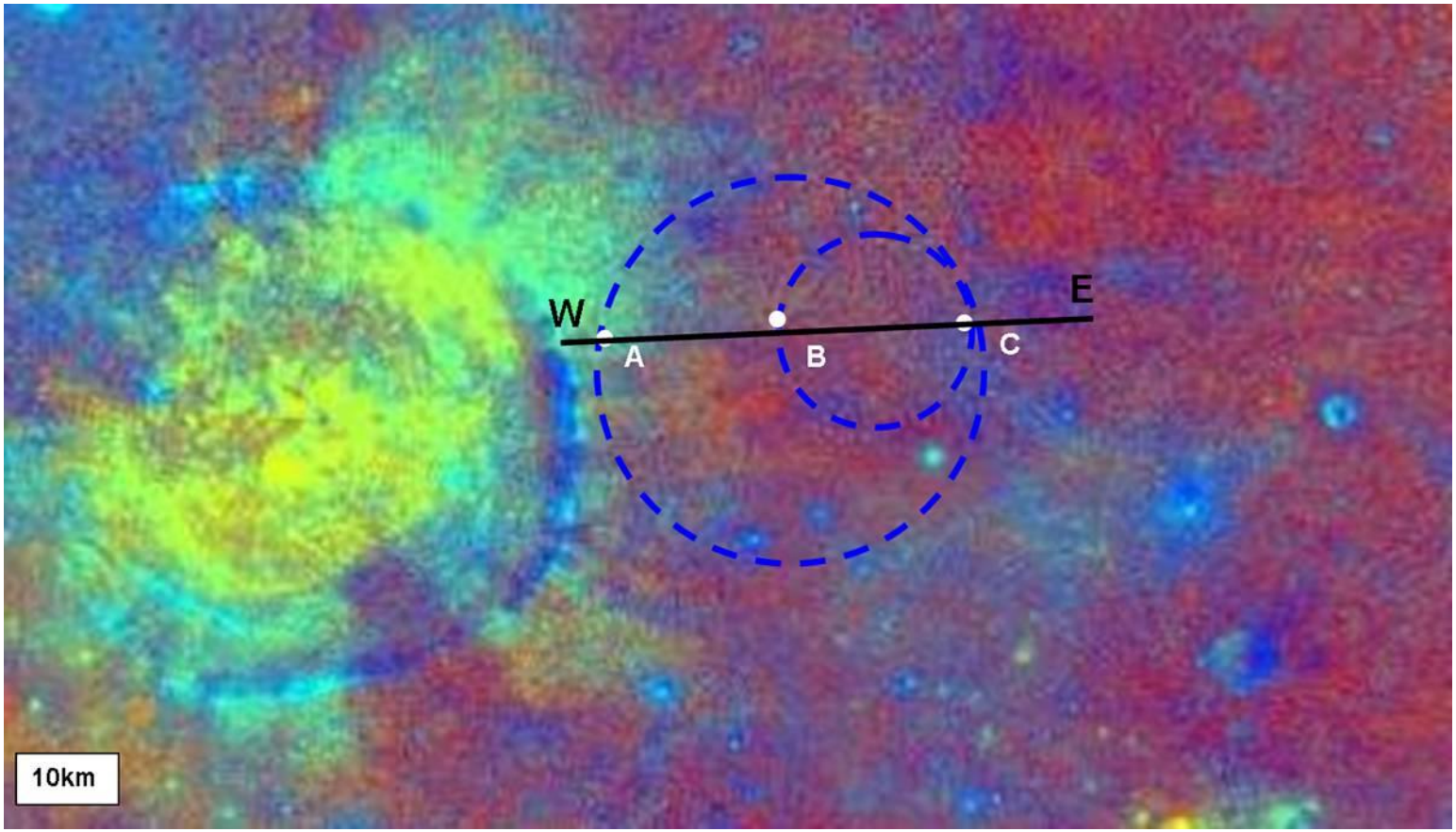

FIGURE 6.72 Maunder Crater and the extent of 10 and 20 km exploration radii on a Clementine false rgb image. Three sample localities are highlighted: A, B, and C. At A and B Science Goals 6a, 6c, and 6d, can be addressed through the sampling of Maunder's ejecta. At locality C, Science Goal 6b can be addressed through the sampling of the Inner Shelf Ring massifs. The extent of Maunder's ejecta is seen by the green and yellow colors emanating from the north east rim of the crater.

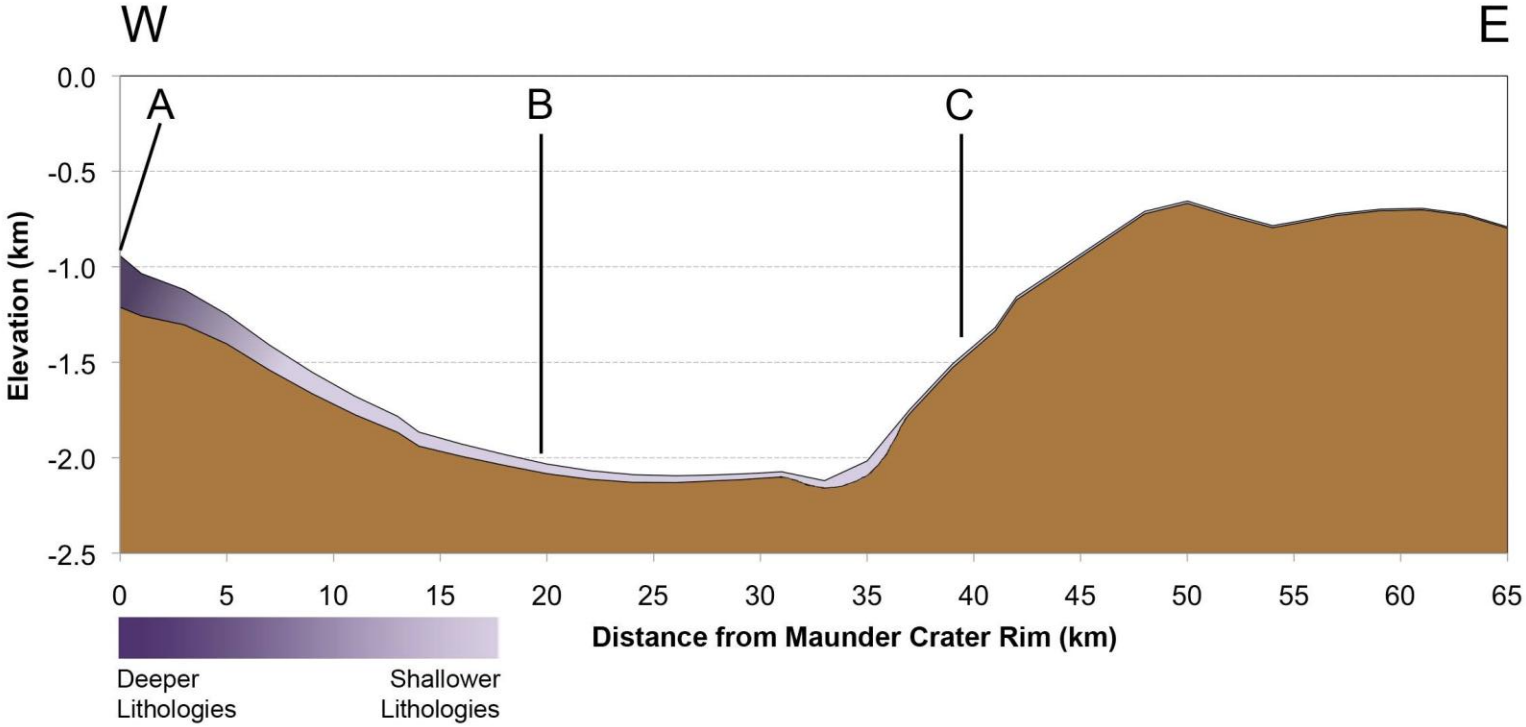

FIGURE 6.73 Cross-sectional profile going east from the crater rim of Maunder to the Orientale Inner Shelf Ring. Purple shows scaled thickness of Maunder ejecta from McGetchin *et al.* (1973). Darker shades depict ejecta that on average originated from greater depths. Stations A, B and C are indicated. Topography is 10× vertically exaggerated (elevation data from Kaguya).

Sample Collection

Science Goal 6a

To determine if the Orientate melt sheet differentiated, samples of Maunder's ejecta should be taken at various distances from its crater rim. Deeper lithologies of Orientale's melt sheet should have been deposited close to the rim of Maunder (site A), while shallower lithologies should have been deposited farther out (sites B and C). Along the traverse from point A to point C samples will be taken intermittently to gauge the amount of chemical variability as a function of Maunder's excavation depth.

Science Goal 6b

Geological sampling can be conducted from boulders lying at the base of the Inner Shelf Ring massif at site C, in the same way as that outlined in the case study for Science Goal 6b. Boulders, based on movement tracks, may be able to be traced back to their original location on the massif. Stratigraphy may be present in outcrops at the massif, which can be used to infer internal structure. Seismic surveying could be carried out however the usefulness of this is dependent upon the size of the exploration radii.

Science Goal 6c

Samples of Maunder's ejecta will hopefully contain not only fragments of Orientale's impact melt sheet, but also fragments of Maunder's melt. Tektites and larger melt clasts incorporated into impact breccias can be analyzed to reveal the composition of Maunder's melt zone. These melt fragments will have the same age as Maunder Crater, and can therefore be distinguished from older Orientale melt fragments. Trace elements in Maunder melt clasts can be analyzed to determine if Maunder was formed from an asteroid or a comet. This can help determine if Maunder's morphology was influenced heavily by impact velocity. Within a 20 km radial traverse limit, Maunder's crater rim is accessible (site A). From there, observations of the modification zone can be made and the motions of terraces can be restored by identifying similar stratigraphic units in various portions of the modification zone.

Science Goal 6d

A sampling traverse from the Fe-rich near-rim deposit to the Fe-poor east/northeast could place constraints on the nature of the observed spectral variation of Maunder ejecta. The decrease in iron content with distance from the crater could be attributed to either lower mixing ratios or increased deposition of Fe-poor ejecta from Maunder. To distinguish between these two factors, a second traverse along the Fe-poor ejecta should be undertaken. To recognize the precise composition of Maunder's ejecta, with certainty, excavated material from the crater rim must be analyzed. Once this composition is known, mixing ratios further from the rim can be calculated. This sampling strategy would be more effective if conducted over a larger area, as a 10 km exploration radius will not contain the full range of material excavated by Maunder.

Maunder Case Study Summary

None of the sites highlighted here are necessarily the best for investigating any of the Science Concept 6 science goals, however this study location does allow all Science Concept 6 Science Goals to be investigated simultaneously. To address the question of melt sheet differentiation, it is more effective to sample a crater near the center of Orientale, where the melt sheet is thicker and more likely differentiated. Sampling inside Maunder Crater is better for studying crater morphology. Both of these requirements however, conflict with the investigation of basin structure. In order to access peak ring material, landing sites near Orientale's transient crater must be chosen, where impact melt and peak rings are likely to be in relatively close proximity.

With a 10 km radial traverse limit, it is possible to address all goals encompassing Science Concept 6: melt sheet differentiation (6a), the composition of the Inner Shelf Ring (6b), the target composition of Maunder Crater (6c), and ballistic sedimentation (6d). However, a traverse limit of 20 km would allow a more thorough assessment of each goal: originally deeper lithologies, including, in theory, more Orientale melt sheet) be collected, a greater number of outcrops along the Inner Shelf Ring could be accessed, Maunder Crater's modification zone could be examined, and more chemically distinct ejecta could be sampled to help determine the degree of mixing. With either traverse limit, a mission at this site would provide insight into fundamental impact processes, and provide data to test a wide variety of impact hypotheses.